Synthesis and Characterization of Graphene Oxide for System Integration in Semiconductor Components

Dissertation zur Erlangung des Doktorgrades der Naturwissenschaften

(Dr. rer. nat.)

an der Fakultät Chemie und Pharmazie

der Universität Regensburg

Deutschland

vorgelegt von

Anton Kröner

aus Landshut

im Jahr 2020

Die vorgelegte Dissertation entstand in der Zeit von Februar 2016 bis Juni 2020 in einer Kooperation von Infineon Technologies AG Regensburg und dem Institut für Analytische Chemie, Chemo- und Biosensorik der Universität Regensburg.

Die Arbeit wurde von Prof. Dr. Antje J. Baeumner und Dr. Thomas Hirsch aufseiten der Universität Regensburg und von Dr. Alexander Zöpfl, Dr. Günther Ruhl und Dr. Stephan Pindl aufseiten von Infineon Technologies AG Regensburg angeleitet.

Promotionsgesuch eingereicht am: 17.06.2020

Kolloquiumstermin: 10.09.2020

Prüfungsausschuss

Vorsitzender: Prof. Dr. Oliver Tepner

Erstgutachterin: Prof. Dr. Antje J. Baeumner

Zweitgutachter: PD Dr. Axel Dürkop

Drittprüfer: Prof. Dr. Alkwin Slenczka

Acknowledgements

List of Acronyms

(c)AFM..(conductive) Atomic Force Microscopy

(HR) TEM ....(High Resolution) Transmission Electron Microscopy

2D .... Two-dimensional

AES.. Auger Electron Spectroscopy

ASIC .... Application Specific Integrated Circuit

BET .... Brunauer-Emmett-Teller

CCD .... Charge coupled device

CP...Conductive Polymers

DLS...Dynamic Light Scattering

EDS.. Energy Dispersive X-ray Spectroscopy

EELS ....Electron Energy Loss Spectroscopy

FIB... Focused Ion Beam

FPGA .... Field Programmable Gate Array

FWHM.. Full Width at Half Maximum

GO .... Graphene Oxide

GQD .... Graphene Quantum Dots

ICP-AES............... Inductively Coupled Plasma Atomic Emission Spectroscopy

LM ....Light Microscopy

LOD .... Limit of Detection

MAK .... Maximale Arbeitsplatz Konzentration

MFC .... Mass Flow Controller

MS ....Mass Spectrometry

NMR.. Nuclear Magnetic Resonance

PCB...Printed Circuit Board

PL .... Photoluminescence

rGO.. reduced Graphene Oxide

RTP .... Rapid Thermal Processing

SECM ....Scanning Electrochemical Microscopy

SEM ....Scanning Electron Microscopy

STEM.. Scanning Transmission Electron Microscopy

Table of Contents

1 Current Trends in Optical Characterization of Two-Dimensional Carbon Nanomaterials

1.1 Abstract

Graphene and graphene-related materials have received great attention because of their outstanding properties like Young's modulus, chemical inertness, high electrical and thermal conductivity, or large mobility. To utilize 2D materials in any practical application, an excellent characterization of the nanomaterials is needed as such dimensions, even small variations in size, or composition, are accompanied by drastic changes in the material properties. Simultaneously, it is sophisticated to perform characterizations at such small dimensions. This review highlights the wide range of different characterization methods for the 2D materials, mainly attributing carbon-based materials as they are by far the ones most often used today. The strengths as well as the limitations of the individual methods, ranging from LM, SEM , (HR-) TEM, STEM, STM, (c)AFM, SECM, Raman spectroscopy, UV-Vis spectroscopy, XPS, XRF, EDS, AES, EELS, XRD, ICP-AES to DLS, are discussed. By using these methods, the flake size and shape, the number of layers, the conductivity, the morphology, the number and type of defects, the chemical composition, and the colloidal properties of the 2D materials can be investigated.

This chapter has been published.

Author contributions: This review article was published after peer reviewing. The authors have been invited to make this contribution. The literature survey was performed by Anton Kröner. The concept and structure of the manuscript was planned together with Thomas Hirsch. Anton Kröner wrote the manuscript. Thomas Hirsch revised the manuscript and is corresponding author.

1.2 Introduction

2D materials, especially graphene or graphene-related materials, have been studied extensively in the past decade regarding their outstanding properties such as mechanical strength, chemical inertness, high electrical and thermal conductivity, high mobility, or optical transmittance [1-3]. These features lead to the assumption that graphene-related materials are promising candidates to be used in a large field of applications like high-power electrical or radio frequency devices, batteries, and bio- and chemo-sensors, or as membrane for water purification [4-7].

Graphene was firstly cleaved off from graphite in 2004 by Geim and Novoselov via a scotch tape method [8]. Since this time, a lot of progress was made, and many other layered materials have been exfoliated as 2D nanomaterials [9]. Researchers even report on the sophisticated hybrid materials, taking benefit, or creating new features by the functionalization or the combination of two or more nanomaterials. Individual 2D nanomaterials, such as graphene, BN, MoS_2, and WS_2, are already commercially available nowadays. Nevertheless, these products often suffer from little to no information on their exact properties such as size, number of layers, and defects.

The size of graphene ranges typically from several nanometers over micrometers up to millimeters, maintaining a thickness of only one atom at best. Bottom-up methods like chemical vapor deposition or epitaxial growth on SiC produce graphene in wafer-scale areas; top-down methods like chemical, mechanical, or electrochemical exfoliation generated graphene wherein the graphene flakes have a very wide size distribution [10, 11]. Furthermore, the top-down methods produce graphene with different qualities in terms of the kind and the number

of defects. These defects can have some benefits like improved dispersibility in water, or it can be detrimental since the electrical conductivity gets decreased [12].

Furthermore, to tailor properties like chemical sensitivity, catalytic effects, or mechanical strength, such materials need to be modified by other nanomaterials and (bio-)molecules, or by doping with other elements [13]. Besides knowing the exact chemical composition of the 2D material, it is also of great importance to identify the contaminants or the impurities introduced during the fabrication, the modification, or the implementation into an application [14, 15]. Moreover, to get a complete picture, more than one analytical method is often needed. Furthermore, the characterization often gets more difficult because the sample preparation for many techniques is not straight forward. In this review, the state-of-the-art characterization techniques of graphene-related materials in terms of flake size and shape, number of layers, morphology, number and type of defects, functionalization, as well as colloidal properties are discussed.

1.3 Characterization

2D carbon nanomaterials need to be prepared, transferred, or modified in many different ways to get the benefit of their attractive features. Therefore, it is of great importance to characterize the material in each stage of synthesis or processing, but at the same time, characterization is extremely challenging due to the small dimensions and the needed accuracy as already small variations in the shape, the dimension or the composition of such materials can already greatly affect their properties. Several microscopic or spectroscopic methods for graphene characterization have been established and are reviewed in the following from the viewpoint of the material property which is desired to be investigated in detail.

1.3.1 Size and Shape

A typical feature of a nanomaterial is the change of its properties with size and shape. The same is true for the 2D materials. These materials intrinsically do not have any bulk phase, which means that every single atom is a surface atom. Nevertheless, at the edges, the valences of such atoms might be different compared to those located within the flake. The chemical and physical properties of the graphene flakes get affected by the degree of sp^2-conjugated carbon atoms, and thereby it is important to measure the size and the shape of the 2D materials. The size of spherical objects (0D material), like monodispersed nanoparticles, can be fully described by the radius and is therefore easy to be characterized. In contrast, non-spherical nanomaterials, such as all kinds of 2D materials, demand a more complex characterization. Exfoliation-based preparation methods lead to irregular shapes and a large distribution in sizes. Therefore, at least the average length and width have to be known to get a first impression of the flake size and of the surface area. Top-down syntheses produce graphene flakes ranging from several micrometers down to a few nanometers in size. A detailed statistical analysis of the flake size distribution is recommended [16] as the mean values together with the standard deviations are only useful for a Gaussian distribution of the flake sizes. If two or more populations are predominantly present, a median value, representing 50% of the population which is below or above, or a mode size ascribed to the fraction with the highest frequency will be more informative. The 2D materials can also exhibit holes within a single flake, which makes the characterization even more sophisticated. This might be important for the design and the characterization of graphene membranes for separation or in electronic applications [17, 18]. An exact knowledge of the size and the shape is especially necessary, when changes in dimensions tremendously impact the physical properties, such as electronic transport, absorbance, or luminescence [19-22]. The Feret diameter is a valuable parameter for the characterization of flake sizes as its value considers the irregularities in shape [23]. To obtain the Feret diameter, the area of an individual flake has to be fitted by two tangents which are parallel to each other.

The maximum distance between both tangents is assigned as the Feret diameter or $Feret_{max}$. Since the Feret diameter includes precise information in only one dimension of a graphene flake, it is necessary to measure a second Feret diameter, the so-called $Feret_{min}$ diameter, which measures the minimum distance between the two tangents, rotated by an arbitrarily angle (Figure 1 (A)). Both values can be combined to a single value, referring either to the ratio ($Feret_{ratio}$) or to the average ($Feret_{mean}$) [24].

To determine the flake size distributions, one needs to image a large number of individual flakes with high resolution to be able to get a reliable statistical analysis. SEM or HR-TEM are suitable, but for large flake sizes excessing the nanometer range, they might run into limitations caused by the slow throughput or by their resolution [25]. Surprisingly, it is also possible to observe single graphene flakes by LM, due to the reflections and the interferences of the incident light at the flake surface and at a substrate of choice, when an optical transparent layer of a certain thickness separates both. The flake gets depicted by its optical contrast, which depends mainly on the differences in the refractive index and the respective absorption coefficients between the observed material and the substrate (Figure 1 (B)). The commonly used substrates for graphene are silicon wafer coated by a silicon oxide layer with a thickness of around 90 nm [26] or 300 nm [27] under white light illumination. Even better contrasts can be obtained by using an excitation wavelength of 543 nm and a silicon nitride layer of 72 nm on the silicon substrates [28]. Graphene flakes up to a few micrometers in size can be screened very fast and precisely by this method. With a suitable software, e.g., the open source project imageJ, such high-contrast pictures can be automatically analyzed by transferring the images into 8-bit monochrome images and by performing a Gaussian fit [29, 30]. Whenever possible, it is recommended to perform an automated analysis as those are not biased by any expectations of the user. The analyses of microscopic images are often challenged by the fact that the flakes overlap each other. This makes an accurate evaluation of the size nearly impossible. When the flakes can be dispersed, the issue of overlapping can be overcome by dilution of the sample before applying it to the substrate. Nevertheless, the sample preparation can become a tedious work.

If the graphene flakes are in the nanoscale, SEM is the method of choice [31]. To gain a high resolution, the type of substrate is essential. As for LM, the image quality of SEM pictures depends on the substrate. Here copper [32] or silicon oxide [33] performs very well (Figure 1 (C)). Moreover, for a successful visualization of graphene by using SEM, good electrical conductivity between the sample and the sample holder must be ensured, to prevent the charging effects by the e-beam [34]. To achieve an atomic resolution, or to detect vacancies in the atomic framework, HRTEM has been successfully applied [35]. By the same method, the defects in the carbon lattice of GO with only a few-atoms resolution have been successfully visualized (Figure 1 (D)) [18]. With liquid cascade centrifugation, it was proposed that the mechanically exfoliated 2D nanomaterials (WS_2 and MoS_2) can be discriminated by their flake size. This was proven by the characterization of the flake size distribution by TEM and AFM. From these analyses, metrics have been developed to characterize the size from the extinction spectra of the dispersion containing the respective nanomaterials (Figure 1 (E)) [36].

A perfect graphene flake consists exclusively of six-membered carbon rings only; as a consequence, only the angles exactly 60° and 120° will characterize the graphene flake borders. From theoretical modeling, it is known that the zigzag graphene edges have specific magnetic properties which are interesting for spintronic devices (Wang et al., 2008). The triangular graphene flakes should theoretically consist of zig-zag edges only, and by this, it is desired for certain applications to create flakes of this shape [37]. This goes along with the need of a characterization method to investigate the structure of the carbon atoms forming the border. The shape of the graphene flakes can be easily influenced during synthesis by the CVD processes that involve changing the growth parameters like temperature, methane flow rate, or growth direction and finally confirming by SEM and AFM measurements [38].
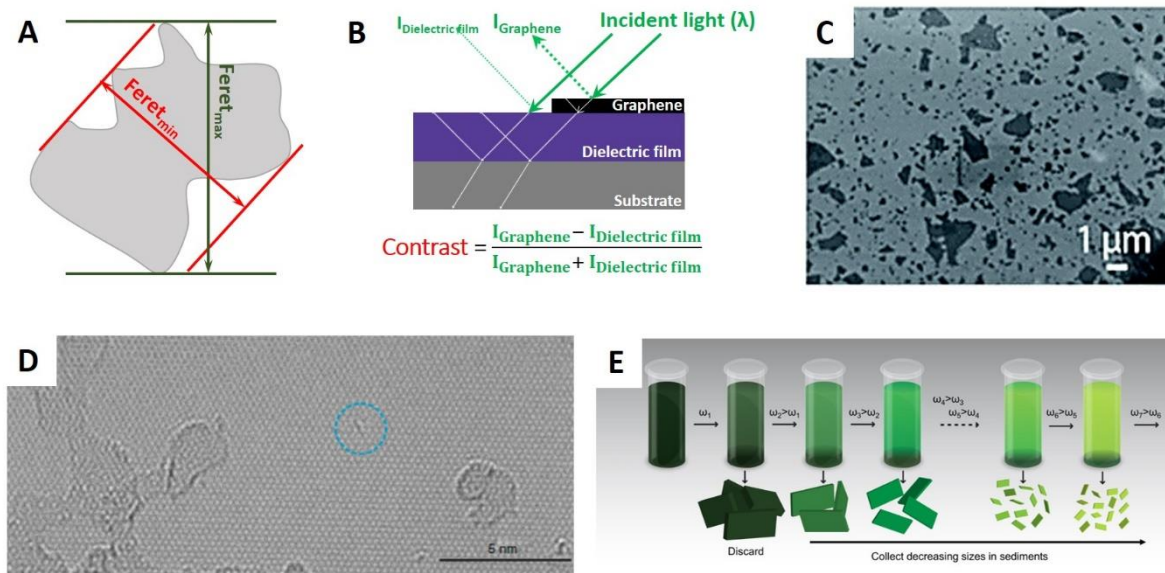
Figure 1. (A) A schematic explanation of Feret$_{min}$ and Feret$_{max}$ diameters. **(B)** Schematic illustration of image generation of a layered Graphene system using LM due to optical transmission and reflection. **(C)** The SEM images of GO with high optical contrast and flake overlapping. **(D)** A TEM image of honeycomb carbon lattice next to lattice defects. **(E)** The centrifugation cascade of exfoliated Graphene to reach narrow Graphene flake size distribution.

(B) Adapted with permission from [39]. Copyright (2017) American Chemical Society
(C) Reproduced under a Creative Commons Attribution (CC BY 3.0) License from [40].
(D) Reproduced under a Creative Commons Attribution (CC BY 4.0) License from [35].
(E) Reprinted with permission from [41]. Copyright (2016) American Chemical Society.

1.3.2 Number of Layers

Per definition, graphene consists of a single carbon layer only [42]. Nevertheless, individual graphene flakes can be arranged in stacks to create the special properties or as an unwanted byproduct obtained by top-down fabrication methods. Few-layer graphene can also arise upon agglomeration when stored in dispersions or after assembly from the liquids on a substrate. To determine the thickness of the graphene layers or the number of layers of stacked graphene flakes, several methods can be used. Here similar requirements have to be fulfilled to determine the number of layers as for the characterization of the flake size. For example, the optical contrast between the graphene and the substrate must be sufficiently high to resolve few-layers graphene by optical or electron microscopy. The number of graphene layers on the substrate can be estimated by correlation between the contrast and the specific thickness: e.g., the number

of graphene flakes has been determined by using a 7.5 nm Au, 1 nm Ti, and 93 nm SiO_2 stacked on a silicon wafer, and by analyzing the reflected light collecting the image after a 520 nm band pass filter by its optical contrast [43]. A disadvantage of this method is that the graphene layer thickness can be estimated only by knowing the thickness of one single layer of the 2D nanomaterial. Since the layer thickness of many carbon 2D materials is affected by the number of defects and therefore depends on the degree of oxidation, an even more precise method, such as AFM, can be applied (Figure 2 (A)). To reach resolutions in height smaller than 1 nm over a large lateral area, it is absolutely necessary to use substrates like mica or large salt crystals which are known to be atomically smooth. Again, the transfer of the material onto the substrate without inducing wrinkles or depositing impurities is challenging. Also, flake overlapping needs to be avoided. The differences in the thickness of <1 nm have been resolved [44, 45], and also the number of graphene layers (from one layer up to 10 layers) was determined [39, 43, 46]. To characterize the thicknesses of deposited graphene layers, FIB cuts can be fabricated and analyzed by electron microscopy. Here, the sample is bombarded by ions or electrons which generate a cut into the graphene layer. Subsequently, a SEM image of the cross-section reveals the layer thickness of the deposited graphene (Figure 2 (B)) [47]. The FIB cut method comes with the disadvantage of destroying the sample. In addition, the sample preparation and the measuring time for FIB cuts is higher compared to standard SEM images. The non-conductive samples have to be taped or sputtered with metals like silver, gold, or platinum to prevent electrical (over)charging in the SEM microscope. Typical thicknesses of the metallic overlayer are 10 nm and therefore usually much thicker than the 2D material itself. This means that sputtering can have a big impact on the 2D material layer thickness, especially if one is interested in the thickness of loosely stacked graphene flakes as they might be used in membranes, which easily can be compressed by the metallic layer deposited on top. Furthermore, it is challenging to derive a homogeneous thickness of the sputtered material in x- and y-direction, because layers are too thin lack in conductivity and still lead to overcharging, whereas too thick layers obscure the fine details and make reliable thickness determination nearly impossible [48].

Whereas, FIB cut is not ideal to visualize monolayers of graphene, the strength of this method is the thickness determination of the coated, the dispensed or the printed graphene layers. The graphene thickness can also be determined by the optical contrast of TEM. Ghosh et al. checked the number of graphene layers by HRTEM in energy storage applications [49]. Since a substrate is necessary for the printed or the dispensed graphene by using inks, TEM is not applicable for this kind of characterization.

In addition to imaging methods, the layer thickness and the number of layers, respectively, can also be determined by Raman spectroscopy. With an increased number of graphene layers, the G-peak is subject to a slight shift to lower wavenumbers, whereas the D-peak undergoes changes in shape, width, and position (Figure 2 (C) and (D)) [50]. The intensity ratio of the maximum of the 2D-band to the G-band can be used as a possible quantitative metric for the determination of the number of graphene layers [36]. An empirical model revealed the following equation to calculate the number of graphene layers (<N>).

$$< N >= 1.04 \, \frac{I_{2D}}{I_G}^{-2.32}$$

It is still questionable if such an empirical formula is valid for all combinations of materials, e.g., it needs to be validated if the coefficients in this model need to be adapted by experimental settings, e.g., by the laser wavelength of the Raman spectrometer. Nevertheless, this method has the advantage to estimate the number of graphene layers in a fast and cheap way and over a large sample area. The disadvantages of this method come with the fact that the error of this metric is around 25% [36], and therefore only rough estimations are possible, which might be useful in a process control during a fabrication step, where high throughput is important. For such purposes, it would also be attractive to refine the metrics according to the given materials and equipment.
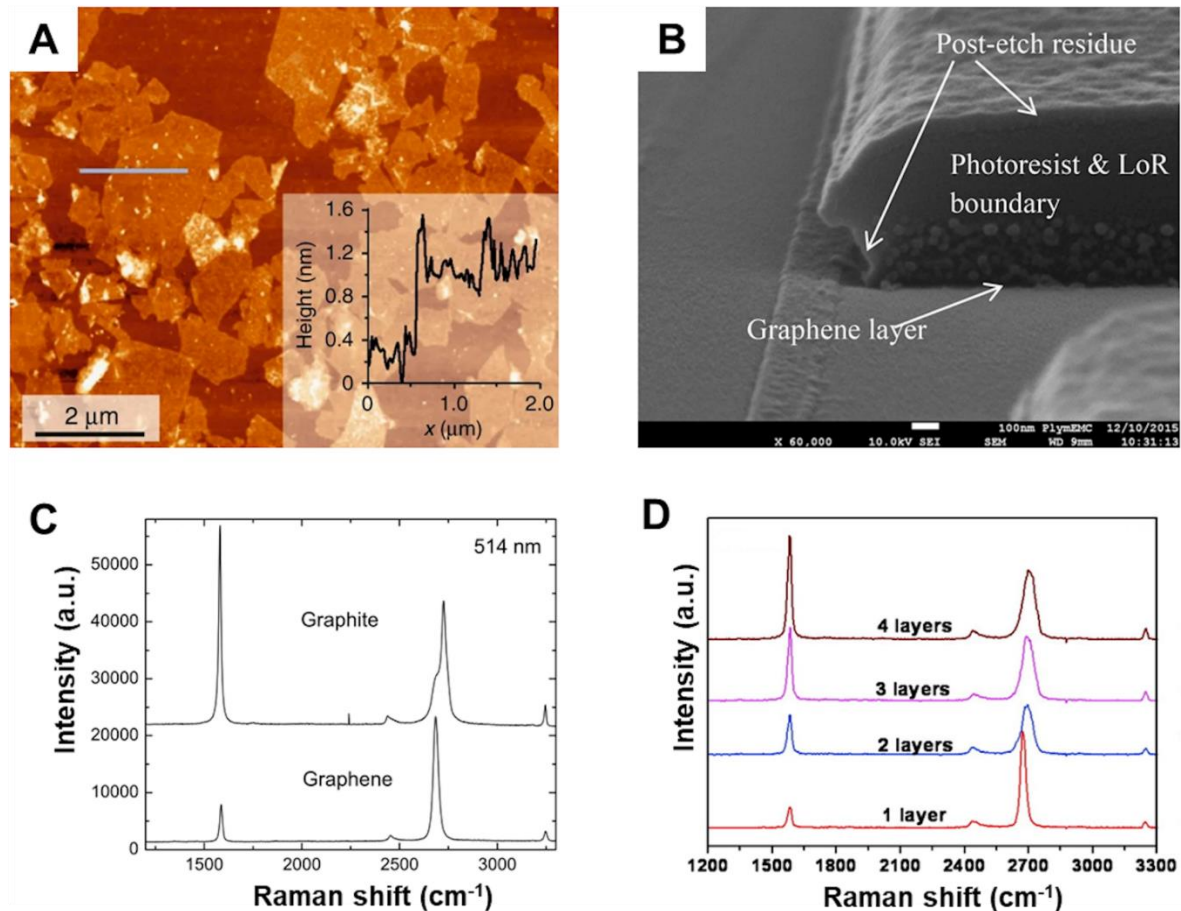
Figure 2. (A) An AFM image of exfoliated Graphene with corresponding height profile along *grey line*. **(B)** SEM image of a FIB cross-section through a Graphene layer, **(C)** Raman spectra of graphite and Graphene at 514 nm and **(D)** Raman spectra of Graphene with different number of layers at 532 nm.

(A) Reproduced under a Creative Commons Attribution (CC BY 4.0) License from [35].
(B) Reproduced under a Creative Commons Attribution (CC BY 4.0) License from [51].
(C) Reprinted with permission from [50]. Copyright (2006) by the American Physical Society.
(D) Reprinted and adapted from [52]. Copyright (2008) American Chemical Society.

1.3.3   Morphology

The surface roughness or topography significantly contributes to the graphene flake surface area and is mainly introduced by the defects in the carbon lattice. It is especially of interest in any application taking benefit of a large surface area or special surface properties, e.g., binding of absorbents in chemical sensing [53] or as a catalyst in synthesis applications [54]. On the one hand, defects, such as those due to epoxy or hydroxyl groups, distort the atomically

smooth surface of graphene, and on the other hand, defects caused by the distortion on the honeycomb lattice, such as five- or seven-membered rings as well as carbon atoms exchanged by nitrogen and boron, affect the topography of the material as described by the wrinkles in the material. The surface roughness of individual graphene flakes is typically in the low-nanometer range and can be characterized by AFM, STM, or SEM. When using SEM, low-acceleration voltages in the range of 3 kV [55] need to be used to keep the penetration depth of the electrons low so as to enable highest surface sensitivity. Since the electrons have a small reach in matter, SEM images made by secondary electrons are extremely surface-sensitive and can resolve the surface morphology (Figure 3 (A)). To get information on the surface morphology in atomic resolution, AFM is the method of choice. The resolution of AFM - typically in the 1 nm range - is sufficient to resemble even absolute dimensions and therefore allows an easier comparison to each other. Investigations of few-layer graphene at different temperatures showed that the graphene roughness can be influenced by temperature [56]. Moreover, by using AFM, an influence on the surface smoothness by the degree of oxidation of the carbon nanomaterial was demonstrated. Exposure to hydrogen iodide vapor smoothens the surface by reducing the GO. This indicates the successfully elimination of oxygenated functional groups of GO [57]. An impressive AFM study on the hydrogen-intercalated epitaxially grown graphene on SiC (0001) demonstrates that curvatures or steps in the graphene are favored spots for adsorbates. The authors achieved, for the first time, an outstanding resolution of 0.3 – 0.4 nm at ambient conditions (Figure 3 (B) and (C)) [58]. In contrast to this method, the roughness of a graphene surface was also resembled in atomic resolution by using STM (Figure 3 (D)). The morphology differences even in the very low angstrom range (< 0.5 Å) can be resolved [59], but this method suffers from the need of vacuum conditions for measurement.

Besides the single graphene flakes, also graphene films consisting of many flakes are also of interest in terms of characterization of their topology. For screening of the homogeneity of graphene films, optical microscopy images can be used. Wrinkles, overlapping flakes, and non-confluently assembled graphene films deposited from graphene suspensions can be investigated in a simple

manner [60]. Inhomogeneous graphene layers with the so-called coffee-ring characteristics, which are typical for dispensing and drop-casting of nanomaterials, often needs to be avoided, since the properties, e.g., layer thickness or electrical conductivity, are different at the coffee-ring compared to the rest of the graphene layer [61]. By observing a Raman line scan over the deposited graphene area or layer and calculating the I_D/I_G-ratio, it is possible to obtain information about the oxidation degree and the location of defects and therefore the homogeneity of the dispensed or the printed graphene layers [62].

Moreover, porous materials, such as graphene aerogels, are characterized by a rough surface and an uneven topology. Typical for this class of materials is the large surface area, which can be used for the intercalation or the absorption of gases, liquids, metals, or ions. Especially parameters like the pore sizes, which is typically in the range of a few nanometers, and the pore size-distribution are of great interest for applications like absorption membranes, energy storage components, or nanoelectronics [63, 64]. For the investigation of the pore diameter, as well as the pore distribution SEM (Figure 3 (E)) has been preferably used [65]. Furthermore, the pore density as well as the channels formed by pores can be studied [66]. In another example, GO was reduced, and porosity was introduced by a NaOH treatment followed up by an acid treatment to ensure that the carboxylic functionalities remain acidic. Pores with an average diameter of 2.16 nm and a pore density of 5.74% have been obtained and characterized by the pore area analysis of STM images [67]. For assemblies of 2D materials consisting of channels that forms fluidic networks, as desired for filtering applications, a detailed information about the pore size is indispensable. It was shown by AFM that the average pore size can be tailored from 3.7 nm upon 6 h of γ-ray irradiation up to 13.6 nm for 24 h treatment [68]. While AFM and STM, with their convincing resolution in the nanometer to the sub-nanometer range, and are therefore superior to SEM, both methods suffer in terms of applicability and throughput.

Microscopy techniques of all kinds mainly characterize the outer receptively visible surface of the porous materials; a further method has to be introduced where the total surface area, meaning the inner and the outer surface, can be

investigated. For that, BET studies are helpful [69]. Here, typically N_2 is introduced into a sample chamber and is adsorbed on the material to be investigated. Finally, the adsorbed gas is measured, and the entire surface can be calculated. Microporous graphene paper which can be used as the air cathode for Li-O_2 batteries fabricated, and the total surface area (around ca. 373 m^2 g^{-1}) was determined by BET adsorption [70]. Furthermore, by using BET, the influence of GO reduction on the total surface and on the average pore width can be characterized and determined. BET showed that the reduction method via ascorbic acid leads to more surface area and a smaller average in pore width compared to the reduction with urea [71]

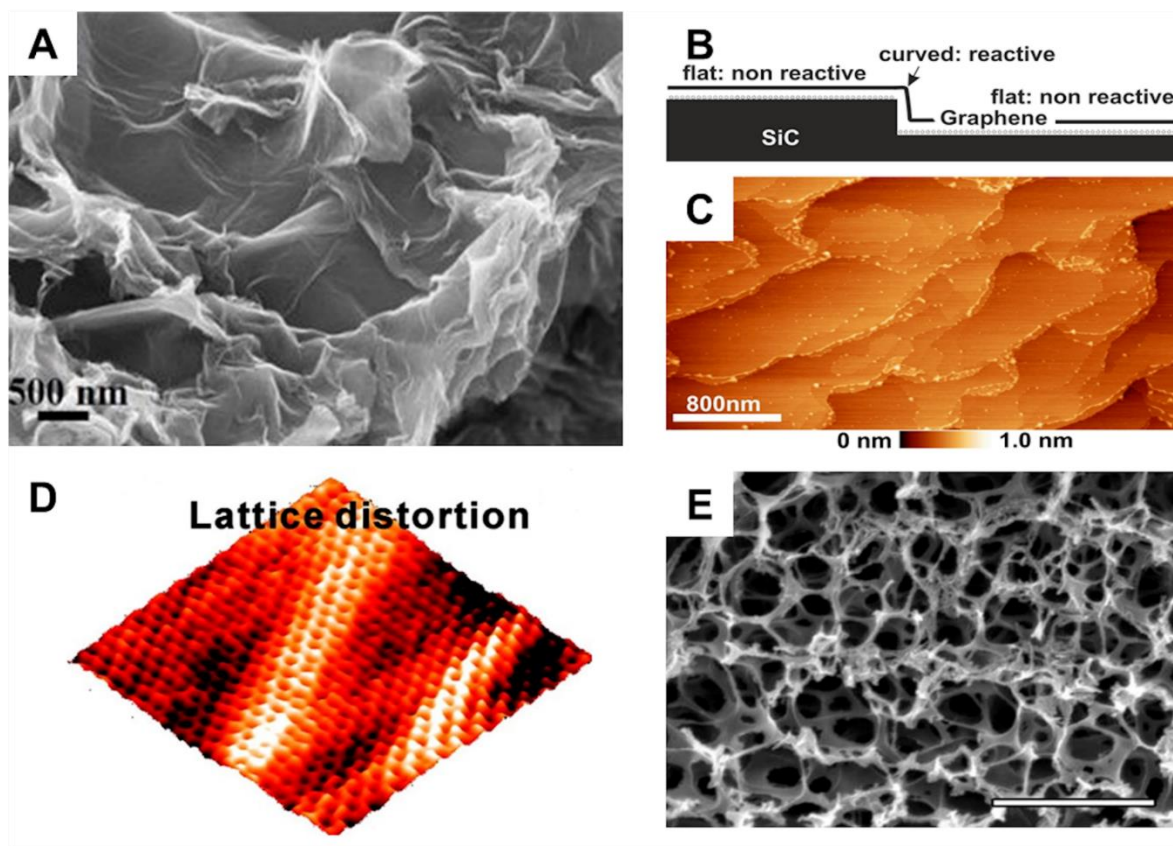**Figure 3. (A)** A SEM image of rGO with highly wrinkled morphology. **(B)** A measuring setup to characterize large Graphene terraces at ambient conditions **(C)** An AFM image of Graphene. The high spots indicating reactive edges. **(D)** A 3D STM image of Graphene which demonstrating clear lattice distortions. **(E)** A SEM image of nano-porous Graphene for determination of pore size and pore size distribution.

1.3.4 Chemical Functionalities

Fabrication methods for the 2D materials following a top-down approach are additionally needed to identify and to characterize contaminations, impurities, and functionalities introduced during the synthesis. The importance arises from the fact that even low contaminants bear the risk of changing the chemical and physical properties of the nanomaterial. The comparison of differently prepared materials is not an easy task up to now as there are no widely accepted standards in material characterization that have been established, e.g., in organic chemistry, by giving data from NMR and MS, when a new compound is reported. During the fabrication, the carbon nanomaterials get contaminated by the species used for the preparation, the purification, or the transfer process [75]. Especially chemicals with high binding affinity to the large surface of carbon atoms need to be determined.

A widely used method to fabricate graphene is the chemical or electrochemical oxidation of graphite [76]. These methods introduce the different oxygen functionalities like hydroxides, epoxides, and carbonyl or carboxyl groups into the honeycomb graphene lattice. By changing the parameters in the synthesis, the number and kind of such groups can be influenced, and therefore the degree of functionalization allows the tuning of many properties such as electrical conductivity or dispersibility of the 2D materials.

The characterization of the chemical composition in qualitatively as well as quantitatively way is routinely performed by XPS. A huge advantage of this method comprises of high surface sensitivity. The nature of functionalities can be retrieved from the characteristic binding energy of every element, e.g., the C1s-peak of carbon (at about 286 eV) and the O1s-peak (at around 532 eV) are present in the XPS spectra of graphene prepared by exfoliation techniques. A shift in the binding energies is attributed to the binding partners of every atom, and therefore it is possible to determine the exact moiety of an oxygen functionality [77] (Figure 4 (A) and (B)). XPS has also been applied to determine the oxidation degree of GO [78, 79]. Another method for chemical

characterization is EELS. Here electrons interact with the sample by inelastic scattering, which results in the loss of energy [80]. By observing the C and O k-edge peaks, which represent the respective 2p partial density of states above the Fermi level, it is possible to investigate the degree of oxidation of graphene [81, 82]. Since EELS is often implemented as an additionally feature of HRTEM, it is popular to generate the EELS spectra with atomic resolution, which is superior to XPS [83]. For large areas, or when the lateral resolution is not of such importance, the conductivity changes in graphene can be measured by CAFM (Figure 4 (C)). Here a small tip, which also deals as an electrode, scans over the sample surface. It is possible to generate the conductivity maps of the graphene flakes or layers [84, 85]. The CAFM proved that the inhomogeneities of a substrate surface have an influence on the graphene conductivity [86], and that the conductivity within a graphene flake is also influenced by domains and wrinkles [87].

A very similar technique to characterize the surfaces or the surface interface is SECM. SECM is based on the spatially resolved imaging of electrochemical processes that is detected by micro- or nanoelectrodes. If the applied voltage is sufficiently high, Fe^{3+} is reduced to Fe^{2+} at the electrode tip and generates a diffusion-controlled current, the so-called Faraday current. By measuring the Faraday current, information about the electrochemical reactivity and therefore about the defects in the graphene lattice can be obtained (Figure 4 (D)) [88]. The electro-activity of the reduced-GO-coated polyester fabrics was investigated by SECM. It was shown that an increase in the electro-activity can be observed after the reduction of GO to rGO. Since the measured current depends on the distance between the tip and the sample, it is possible to get information about the surface topology when the tip is held at a constant height. SECM maps visualized the surface morphology of the reduced-GO-coated fabrics [89]. These examples show that SECM is an important technique to characterize the surface or the surface properties of graphene and other 2D materials. SECM is a valuable characterization method especially for the 2D catalysts, where the surface reactivity can be locally monitored. SECM is still limited in its resolution as it is challenging to fabricate ultramicroelectrodes [90].

The oxygen-containing functionalities in carbon 2D materials can also be investigated by XRD, wherein the (0 0 2) diffraction peak at around 25°-30° indicates the distance between the graphene layers and the (1 0) diffraction peak at around 40°-45° indicates the short-range order in the stacked graphene layers [77]. By using XRD, it was possible to monitor the different degrees of oxidation when synthesizing GO by four different chemical exfoliation methods, as indicated by the change in the GO layer distance [91]. Furthermore, the graphene layer distance is correlated with the degree of oxidation, since the oxygenated functionalities are located perpendicular to the basal graphene plain [92]. Also, thermal treatment affects the structure of the rGO, which was followed by comparing these with the (0 0 2) diffraction peak. A shift from 4.79° for the GO to 11.92° for rGO was found after a furnace process at 2000 °C under argon atmosphere [93]. XRD is also a powerful characterization method when the successful fabrication of heterostructures needs to be proven, as demonstrated for an electrocatalytic applications where the GO was modified with Pd/Ni nanoparticles. [94]. For that, the XRD plots of the GO, the Pt/Ni alloy, and the final graphene composite material were compared, and all peaks of the composite were assigned to the starting materials. By matching all the peaks of the composite material to the corresponding starting materials, it is possible to successfully confirm graphene modifications.

EDS or XRF measures the characteristic X-ray radiation of every element in the sample. Whereas, EDS is always applied in combination with any kind of electron microscopy and therefore irradiates the sample with electrons, XRF uses X-rays. By introducing heteroatoms into the graphene lattice, the electronic, the mechanical, or chemical properties can be tailored. EDS measurements confirmed the successfully introduction of germanium into the graphene lattice for a later application in catalysis [95]. For another catalytic application, Cr^{6+} should be reduced to Cr^{3+} by graphene, and therefore the material was modified by 3-aminopropyltriethoxysilane-stabilized Pt nanoparticles. The presence of platinum and silicon in the corresponding EDS-spectrum confirmed the successful functionalization of graphene [96]. Also, sulphur contaminations in the high ppm range on the reduced GO sheets, introduced by the use of sulphuric acid during the fabrication process, have been identified by EDS [97].

Furthermore, the location or distribution of heteroatoms can be revealed by analyzing an EDS map [98]. Compared to EDS, the XRF measuring setup is less complicated, and the detection limit of XRF is lower (XRF ppm; EDS 0.1%) [99, 100]. Additionally, no vacuum is needed, because no scattering takes place between the X-rays and the air. Also, liquid samples like graphene suspensions or inks (in glass tubes) can be characterized by XRF [101]. The contamination introduced during the graphene synthesis can be determined by XRF very easily [102].

One feature where XRF and EDS differ from XPS and AES is the penetration depth [103]. In the case of XPS, the collected electrons result from the outer photoelectrical effect [104] and for AES they are originated by the Auger effect [105]. Both methods are comprised by an extremely low penetration depth of a few nanometers (few atom layers), allowing to get information on the chemical composition of the surfaces [106, 107]. Compared to XRF, both methods suffer from operation in high vacuum, which complicates the device setup and the sample preparation. Moreover, the probability of Auger effect is decreasing with increasing atomic number. Due to the competition to X-ray transition, the quantitative detection is practically limited to the lighter elements [107]. AES is limited to the conductive samples. Nevertheless, it is a powerful technique to investigate mainly the contaminations on the surfaces or thin layers [108], e.g., iron impurities introduced by the transfer of graphene from nickel to Si/SiO_2 substrates were identified as contaminants caused by using $FeCl_3$ to etch the Ni substrate [109]. The graphene modifications of AgBr@Ag/N rGO and the chemical composition of the nitrogen-doped graphene composite have been identified with AES. Due to the presence of Br^-, Ag^+, and Ag^0, they came to a result wherein some Ag^0 are coated by AgBr [110]. Also, the successfully linking of the hexagonal boron nitride and GO was confirmed by AES [111]. To characterize the non-conductive samples or to get more detailed information on the graphene-contaminating or graphene-modifying elements like chemical composition, binding partners, or oxidation state, XPS is the method of choice.
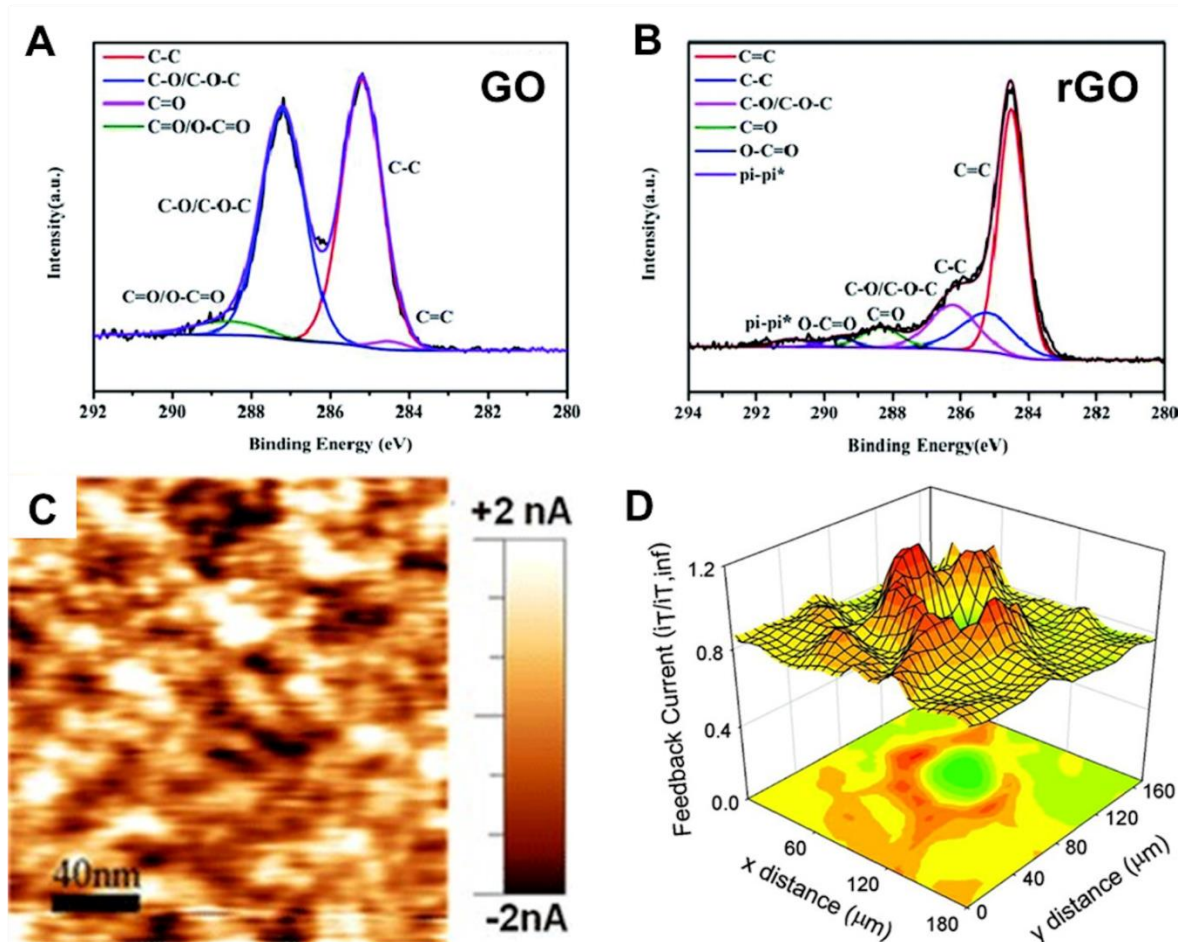
Figure 4. (A) An XPS C1s spectrum of GO with corresponding C1s spectrum of rGO **(B)**. **(C)** A CAFM - map of Graphene with clear current discontinuity (*darker spots correspond to lower conductivity*). **(D)** A SECM 3D image of monolayer Graphene with higher feedback current around the defect/edges.

(A) and **(B)** under a Creative Commons Attribution (CC BY-NC 3.0) License from [112]. **(C)** Reprinted with permission from [113]. Copyright (2012) American Chemical Society. **(D)** Reprinted with permission from [88]. Copyright (2012) American Chemical Society.

1.3.5 Characterization of Graphene Dispersions

The transfer of top-down synthesized graphene is preferably done by dispensing, spin-coating, or ink jet printing on the desired target as these are fast and controlled processes which can be easily applied in any mass fabrication process [114, 115]. For that, the graphene flakes need to be suspended in a liquid that provides high colloidal stability. Therefore, the graphene flake suspensions are often stabilized by substances like sodium cholate [116], ethyl

cellulose, or terpineol [117], which matches the surface energy of the nanomaterial. The resulting graphene inks need to be analyzed in terms of concentration or stability. A big advantage of characterization directly in solution is that the chemical environment of the 2D material needs not to be changed. Measuring the extinction at a wavelength of around 230 nm reveals the concentration of the graphene inks [118]. Since the extinction of the GO suspensions is very high, dilution is necessary, which might be an issue in the case of the composite materials consisting of one material of low-absorption coefficient. Furthermore, by using UV-Vis, it is possible to get a first impression on the chemical structure of the GO. By determining λ_{max}, typically in the range of around 230 nm, information about the amount of sp^2 hybridization can be obtained. A redshift of λ_{max} is attributed to more $\pi \rightarrow \pi^*$ transitions which are equivalent to a more ordered structure and larger sp^2-domains (Figure 5 (A)). A shoulder appearing at a wavelength of around 300 nm indicates the $n \rightarrow \pi^*$ transition of carbonyl groups [119]

It would also be, a nice feature to get an information on the flake size directly from the dispersion as it was performed by DLS (Figure 5 (B)) [120, 121]. Nevertheless, DLS is measuring the hydrodynamic radius and not the absolute graphene flake size. Furthermore, the method of DLS is usually based on spherical particles, and therefore data analysis has to be performed carefully for the 2D materials [25].

The fabrication methods based on chemical exfoliation of graphite to graphene suffer from contaminations of sulphur or sodium which are introduced during the synthesis and which can only be eliminated by excessive dialysis protocols. The determination of these contaminations directly in suspension is very important since the impurities have an influence on the performance as well as on the lifetime of a graphene application [122]. A very practical method to detect contaminations in a liquid environment is ICP spectrometry. By ICP – regardless if ICP-MS or ICP-AES – qualitative information about contaminations down to the ppb/ppt range can be identified directly in the suspensions without any dilution, and therefore no change in the chemical environment has to be taken into account. To avoid or decrease the contaminations, knowledge about the

origin of the impurities is very important. Therefore, the contaminations of several GO syntheses were investigated and compared by ICP-MS to prove that the kind of impurities depends on the chemicals used during synthesis [15]. Higher amounts of potassium and manganese were found in GO suspensions which were fabricated by Hummer's method compared to those of other GO syntheses like those of Staudenmaier or Hofmann [123]. Also, metallic impurities can be detected. This is very helpful to characterize the purification process of GO syntheses [124]. Despite the contaminations, modifications can also be characterized by ICP. Gao et al. determined the cobalt content (35.8%) of their Co/rGO composite by ICP-AES [125].

Nevertheless, to get more detailed information like oxidation state or binding partners, XPS measurements are inescapable. UV-Vis and DLS are not ideal methods to characterize graphene in terms of concentration (high absorbance) and flake size, but both methods can be performed very easily and are cheap and fast; therefore, they must not be neglected for fast screening. Due to this, both methods can be used to check the graphene concentrations in inks or to check their stability in terms of agglomeration. In case of GQDs, these are characterized as nanometer-sized fragments of graphene that show unique properties especially in their luminescence, making these materials attractive for bio-applications [126]. PL properties are useful for optoelectronic applications [127, 128]. Whereas pristine graphene is characterized by a zero-band gap [129] and therefore no PL can be observed, GQD's dispersions are well-known for band gap and their luminescence when they are excited by specific wavelength [20]. Many parameters, e.g., flake size, shape, functionalities, or pH-value influence the GQD's band gap and therefore the PL properties [128]. Since the electron hole recombination at the newly formed sp^2-domains of rGO exhibits blue fluorescence, the PL of rGO (around 450 nm) is blue shifted compared to the PL of GO (around 600 nm) [130]. Furthermore, PL is also strongly influenced by the flake size. For flakes that are too large, the bandgap becomes zero and no PL can be monitored any longer, this material is used as quencher in bioanalytical application. The quenching of the luminescence of a dye can also be used for the characterization of the carbon nanomaterial,

e.g., to evaluate the successful reduction of GO to rGO. A red shift in the PL can be observed when the size N-doped GQDs is increased [131].
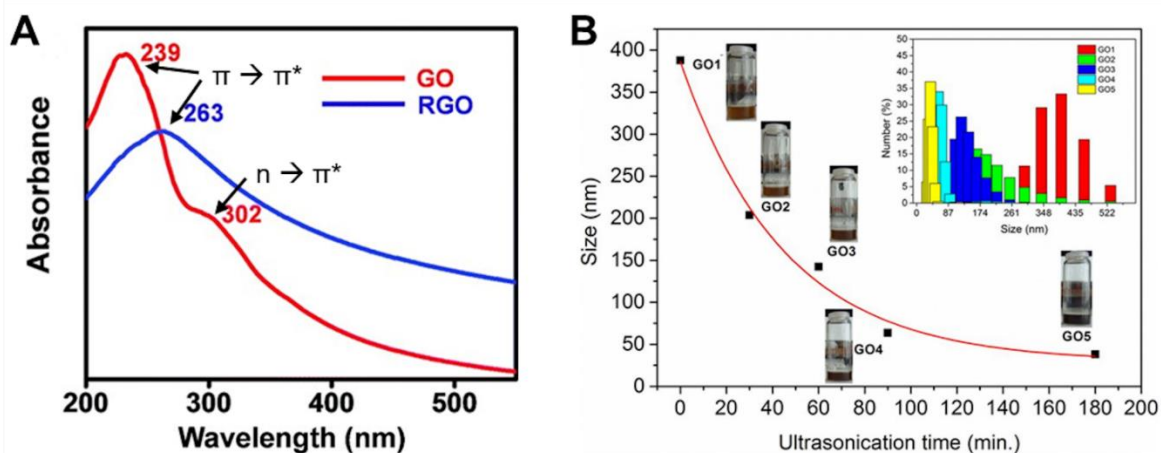

Figure 5. (A) The UV-Vis spectra of GO and rGO with corresponding shift of π → π* and reduction of n → π*. **(B)** The DLS measurements of different GO flake sizes with corresponding sonication time.

(A) Reproduced and adapted under a Creative Commons Attribution (CC BY 3.0) License from [132]. **(B)** Reproduced under a Creative Commons Attribution (CC BY NC-ND 4.0) License from [120].

1.3.6 Summary

Despite the outstanding properties ascribed to the 2D nanomaterials which have demonstrated and extensively reviewed [39, 133, 134] only few practical applications utilizing these materials have reached the market. One of the major hurdles in this field can be found in the inconsistency of the experimental details and the characterizations reported in literature. What is still missing is a standard of minimum information which needs to be reported. To improve the reproducibility and to allow the comparisons of 2D materials fabricated or applied by different groups, it is suggested that parameters such as flake size, number of layers, morphology, functionalities, or colloidal properties of the graphene and graphene-related materials should be reported. It is shown by this review that, for all essential parameters listed, procedures for characterization are available in a great number. For the future, the development of new characterization techniques, and the improvement and hyphenation of already existing methods are desirable, especially in terms of getting faster or higher throughput.

Especially improvements in the surface sensitivity and the detection of contaminations, will enable a better understanding of processing the 2D materials. A reduction of the acceleration voltage of SEM or STEM by maintaining the high resolution or an improved quantification of elements for XPS or AES would be helpful. Future techniques should be able to identify local element doping, defects, or contaminations at the atomic scale. STM, combined further with non-commonly used techniques such as excitation by external optical, magnetic, or electric fields would be very beneficial to investigate and observe the graphene characteristic properties in atomic resolution. Completely missing until now are methods which will enable the online characterization of dynamic processes with high resolution. Such real-time studies are expected to provide new insights in material properties when applied to mechanical, electrical, or electromagnetic stress.

1.4 References

[1]   M. J. Allen, V. C. Tung, and R. B. Kaner, "Honeycomb Carbon: A Review of Graphene," *Chem. Rev.*, vol. 110, no. 1, pp. 132–145, 2010, doi: 10.1021/cr900070d.

[2]   X. Li *et al.*, "Transfer of Large-Area Graphene Films for High-Performance Transparent Conductive Electrodes," *Nano Lett.*, vol. 9, no. 12, pp. 4359–4363, 2009, doi: 10.1021/nl902623y.

[3]   Y. Zhu *et al.*, "Graphene and Graphene Oxide: Synthesis, Properties, and Applications," *Adv. Mater.*, vol. 22, no. 35, pp. 3906–3924, 2010, doi: 10.1002/adma.201001068.

[4]   D. Chen, H. Feng, and J. Li, "Graphene Oxide: Preparation, Functionalization, and Electrochemical Applications," *Chem. Rev.*, vol. 112, no. 11, p. 6027−6053, 2012, doi: 10.1021/cr300115g.

[5]   M. F. El-Kady and R. B. Kaner, "Scalable fabrication of high-power graphene micro-supercapacitors for flexible and on-chip energy storage," *Nat Commun*, vol. 4, no. 1, p. 1475, 2013, doi: 10.1038/ncomms2446.

[6]   C. Zhang, N. Mahmood, H. Yin, F. Liu, and Y. Hou, "Synthesis of Phosphorus-Doped Graphene and its Multifunctional Applications for Oxygen Reduction Reaction and Lithium Ion Batteries," *Adv. Mater.*, vol. 25, no. 35, pp. 4932–4937, 2013, doi: 10.1002/adma.201301870.

[7]   J. Zhao, W. Ren, and H.-M. Cheng, "Graphene sponge for efficient and repeatable adsorption and desorption of water contaminations," *J. Mater. Chem.*, vol. 22, no. 38, p. 20197, 2012, doi: 10.1039/c2jm34128j.

[8]   K. S. Novoselov *et al.*, "Electric Field Effect in Atomically Thin Carbon Films," *Science*, vol. 306, no. 5696, pp. 666–669, 2004, doi: 10.1126/science.1102896.

[9]   H. Zhang, M. Chhowalla, and Z. Liu, "2D nanomaterials: graphene and transition metal dichalcogenides," *Chem. Soc. Rev.*, vol. 47, no. 9, pp. 3015–3017, 2018, doi: 10.1039/C8CS90048E.

[10]   R. S. Edwards and K. S. Coleman, "Graphene synthesis: relationship to applications," *Nanoscale*, vol. 5, no. 1, pp. 38–51, 2013, doi: 10.1039/C2NR32629A.

[11]   L. Tang *et al.*, "Bottom-up synthesis of large-scale graphene oxide nanosheets," *J. Mater. Chem.*, vol. 22, no. 12, p. 5676, 2012, doi: 10.1039/c2jm15944a.

[12]   P. T. Araujo, M. Terrones, and M. S. Dresselhaus, "Defects and impurities in graphene-like materials," *Mater. Today*, vol. 15, no. 3, pp. 98–109, 2012, doi: 10.1016/S1369-7021(12)70045-7.

[13]   J. Liu, J. Tang, and J. J. Gooding, "Strategies for chemical modification of graphene and applications of chemically modified graphene," *J. Mater. Chem.*, vol. 22, no. 25, p. 12435, 2012, doi: 10.1039/c2jm31218b.

[14]   A. Ambrosi, S. Y. Chee, B. Khezri, R. D. Webster, Z. Sofer, and M. Pumera, "Metallic Impurities in Graphenes Prepared from Graphite Can Dramatically Influence Their Properties," *Angew. Chem. Int. Ed.*, vol. 51, no. 2, pp. 500–503, 2012, doi: 10.1002/anie.201106917.

[15]   C. K. Chua *et al.*, "Chemical Preparation of Graphene Materials Results in Extensive Unintentional Doping with Heteroatoms and Metals," *Chemistry - A European Journal*, vol. 20, no. 48, pp. 15760–15767, 2014, doi: 10.1002/chem.201404205.

[16]   M. M. Modena, B. Rühle, T. P. Burg, and S. Wuttke, "Nanoparticle Characterization: What to Measure?," *Adv. Mater.*, p. 1901556, 2019, doi: 10.1002/adma.201901556.

[17]   F. Banhart, J. Kotakoski, and A. V. Krasheninnikov, "Structural Defects in Graphene," *ACS Nano*, vol. 5, no. 1, pp. 26–41, 2011, doi: 10.1021/nn102598m.

[18]   P. Feicht and S. Eigler, "Defects in Graphene Oxide as Structural Motifs," *ChemNanoMat*, vol. 4, no. 3, pp. 244–252, 2018, doi: 10.1002/cnma.201700357.

[19] J. Chen, Y. Li, L. Huang, C. Li, and G. Shi, "High-yield preparation of graphene oxide from small graphite flakes via an improved Hummers method with a simple purification process," *Carbon*, vol. 81, pp. 826–834, 2015, doi: 10.1016/j.carbon.2014.10.033.

[20] B. R. Coleman, T. Knight, V. Gies, Z. J. Jakubek, and S. Zou, "Manipulation and Quantification of Graphene Oxide Flake Size: Photoluminescence and Cytotoxicity," *ACS Appl. Mater. Interfaces*, vol. 9, no. 34, pp. 28911–28921, 2017, doi: 10.1021/acsami.7b08585.

[21] U. Khan, A. O'Neill, H. Porwal, P. May, K. Nawaz, and J. N. Coleman, "Size selection of dispersed, exfoliated graphene flakes by controlled centrifugation," *Carbon*, vol. 50, no. 2, pp. 470–475, 2012, doi: 10.1016/j.carbon.2011.09.001.

[22] M. Zhao *et al.*, "Lateral size effect of graphene on mechanical properties of aluminum matrix nanolaminated composites," *Scr. Mater.*, vol. 139, pp. 44–48, 2017, doi: 10.1016/j.scriptamat.2017.06.018.

[23] W. H. Walton, "Feret's statistical diameter as a measure of particle size," *Nature*, no. 162, p. 329, 1948, doi: 10.1038/162329b0.

[24] J. Walter, T. J. Nacken, C. Damm, T. Thajudeen, S. Eigler, and W. Peukert, "Determination of the Lateral Dimension of Graphene Oxide Nanosheets Using Analytical Ultracentrifugation," *Small*, vol. 11, no. 7, pp. 814–825, 2015, doi: 10.1002/smll.201401940.

[25] A. Liscio *et al.*, "Evolution of the size and shape of 2D nanosheets during ultrasonic fragmentation," *2D Mater.*, vol. 4, no. 2, p. 025017, 2017, doi: 10.1088/2053-1583/aa57ff.

[26] M. Bayle *et al.*, "Determining the number of layers in few-layer graphene by combining Raman spectroscopy and optical contrast: Number of graphene layers by combining Raman spectroscopy and optical contrast," *J. Raman Spectrosc.*, vol. 49, no. 1, pp. 36–45, 2018, doi: 10.1002/jrs.5279.

[27] P. Blake *et al.*, "Making graphene visible," *Appl. Phys. Lett.*, vol. 91, no. 6, p. 063124, 2007, doi: 10.1063/1.2768624.

[28] I. Jung *et al.*, "Simple Approach for High-Contrast Optical Imaging and Characterization of Graphene-Based Sheets," *Nano Lett.*, vol. 7, no. 12, pp. 3569–3575, 2007, doi: 10.1021/nl0714177.

[29] S. Chakraborty *et al.*, "High yield synthesis of amine functionalized graphene oxide and its surface properties," *RSC Adv.*, vol. 6, no. 72, pp. 67916–67924, 2016, doi: 10.1039/C6RA12844K.

[30] X. Lin *et al.*, "Fabrication of Highly-Aligned, Conductive, and Strong Graphene Papers Using Ultralarge Graphene Oxide Sheets," *ACS Nano*, vol. 6, no. 12, pp. 10708–10719, 2012, doi: 10.1021/nn303904z.

[31] J. Chen *et al.*, "Synthesis of graphene oxide sheets with controlled sizes from sieved graphite flakes," *Carbon*, vol. 110, pp. 34–40, 2016, doi: 10.1016/j.carbon.2016.08.096.

[32] Y. Çelik, W. Escoffier, M. Yang, E. Flahaut, and E. Suvacı, "Relationship between heating atmosphere and copper foil impurities during graphene growth via low pressure chemical vapor deposition," *Carbon*, vol. 109, pp. 529–541, 2016, doi: 10.1016/j.carbon.2016.08.057.

[33] S. Grimm, M. Schweiger, S. Eigler, and J. Zaumseil, "High-Quality Reduced Graphene Oxide by CVD-Assisted Annealing," *J. Phys. Chem. C*, vol. 120, no. 5, pp. 3036–3041, 2016, doi: 10.1021/acs.jpcc.5b11598.

[34] K. H. Kim, Z. Akase, T. Suzuki, and D. Shindo, "Charging Effects on SEM/SIM Contrast of Metal/Insulator System in Various Metallic Coating Conditions," *Mater. Trans.*, vol. 51, no. 6, pp. 1080–1083, 2010, doi: 10.2320/matertrans.M2010034.

[35] S. Seiler *et al.*, "Effect of friction on oxidative graphite intercalation and high-quality graphene formation," *Nat. Commun.*, vol. 9, no. 1, p. 836, 2018, doi: 10.1038/s41467-018-03211-1.

[36] C. Backes *et al.*, "Spectroscopic metrics allow in situ measurement of mean size and thickness of liquid-exfoliated few-layer graphene nanosheets," *Nanoscale*, vol. 8, pp. 4311–4323, 2016, doi: 10.1039/C5NR08047A.

[37] L. Ci *et al.*, "Graphene Shape Control by Multistage Cutting and Transfer," *Adv. Mater.*, vol. 21, no. 44, pp. 4487–4491, 2009, doi: 10.1002/adma.200900942.

[38] L. Fan *et al.*, "Controllable growth of shaped graphene domains by atmospheric pressure chemical vapour deposition," *Nanoscale*, vol. 3, no. 12, p. 4946, 2011, doi: 10.1039/c1nr11480h.

[39] C. Tan *et al.*, "Recent Advances in Ultrathin Two-Dimensional Nanomaterials," *Chem. Rev.*, vol. 117, no. 9, pp. 6225–6331, 2017, doi: 10.1021/acs.chemrev.6b00558.

[40] W. Gao, "Effect of flake size on the mechanical properties of graphene aerogels prepared by freeze casting," *RSC Adv.*, pp. 33600–33605, 2017, doi: 10.1039/c7ra05557a.

[41] C. Backes *et al.*, "Production of Highly Monolayer Enriched Dispersions of Liquid-Exfoliated Nanosheets by Liquid Cascade Centrifugation," *ACS Nano*, vol. 10, no. 1, pp. 1589–1601, 2016, doi: 10.1021/acsnano.5b07228.

[42] S. Kochmann, T. Hirsch, and O. S. Wolfbeis, "Graphenes in chemical sensors and biosensors," *Trends Anal. Chem.*, vol. 39, pp. 87–113, 2012, doi: 10.1016/j.trac.2012.06.004.

[43] M. Velický, W. R. Hendren, G. E. Donnelly, J. M. Katzen, R. M. Bowman, and F. Huang, "Optimising the visibility of graphene and graphene oxide on gold with multilayer heterostructures," *Nanotechnology*, vol. 29, no. 27, p. 275205, 2018, doi: 10.1088/1361-6528/aabec1.

[44] C. E. Halbig, O. Martin, F. Hauke, S. Eigler, and A. Hirsch, "Oxo-Functionalized Graphene: A Versatile Precursor for Alkylated Graphene Sheets by Reductive Functionalization," *Chem. Eur. J.*, vol. 24, no. 50, pp. 13348–13354, 2018, doi: 10.1002/chem.201802500.

[45] Q. A. Khan, A. Shaur, T. A. Khan, Y. F. Joya, and M. S. Awan, "Characterization of reduced graphene oxide produced through a modified Hoffman method," *Cogent Chem.*, vol. 3, no. 1, 2017, doi: 10.1080/23312009.2017.1298980.

[46] N.-W. Pu, C.-A. Wang, Y. Sung, Y.-M. Liu, and M.-D. Ger, "Production of few-layer graphene by supercritical CO_2 exfoliation of graphite," *Mater. Lett.*, vol. 63, no. 23, pp. 1987–1989, 2009, doi: 10.1016/j.matlet.2009.06.031.

[47] J. Schnitker *et al.*, "Rapid Prototyping of Ultralow-Cost, Inkjet-Printed Carbon Microelectrodes for Flexible Bioelectronic Devices," *Adv. Biosys.*, vol. 2, no. 3, p. 1700136, 2018, doi: 10.1002/adbi.201700136.

[48] C. G. Golding, L. L. Lamboo, D. R. Beniac, and T. F. Booth, "The scanning electron microscope in microbiology and diagnosis of infectious disease," *Sci. Rep.*, vol. 6, no. 1, p. 26516, 2016, doi: 10.1038/srep26516.

[49] S. Ghosh, S. R. Polaki, M. Kamruddin, S. M. Jeong, and K. (Ken) Ostrikov, "Plasma-electric field controlled growth of oriented graphene for energy storage applications," *J. Phys. D: Appl. Phys.*, vol. 51, no. 14, p. 145303, 2018, doi: 10.1088/1361-6463/aab130.

[50] A. C. Ferrari *et al.*, "Raman Spectrum of Graphene and Graphene Layers," *Phys. Rev. Lett.*, vol. 97, no. 18, p. 187401, 2006, doi: 10.1103/PhysRevLett.97.187401.

[51] B. Li, G. Pan, A. Suhail, K. Islam, N. Avent, and P. Davey, "Deep UV hardening of photoresist for shaping of graphene and lift-off fabrication of back-gated field effect biosensors by ion-milling and sputter deposition," *Carbon*, vol. 118, pp. 43–49, 2017, doi: 10.1016/j.carbon.2017.03.032.

[52] Y. Y. Wang *et al.*, "Raman Studies of Monolayer Graphene: The Substrate Effect," *J. Phys. Chem. C*, vol. 112, no. 29, pp. 10637–10640, 2008, doi: 10.1021/jp8008404.

[53] M. Pumera, A. Ambrosi, A. Bonanni, E. L. K. Chng, and H. L. Poh, "Graphene for electrochemical sensing and biosensing," *Trends Anal. Chem.*, vol. 29, no. 9, pp. 954–965, 2010, doi: 10.1016/j.trac.2010.05.011.

[54] F. Rodríguez-Reinoso, "The role of carbon materials in heterogeneous catalysis," *Carbon*, vol. 36, no. 3, pp. 159–175, 1998, doi: 10.1016/S0008-6223(97)00173-5.

[55] D. C. Joy and C. S. Joy, "Low Voltage Scanning Electron Microscopy," *Micro*, vol. 27, no. 3–4, pp. 247–263, 1996, doi: 10.1016/0968-4328(96)00023-6.

[56] L. Zhou *et al.*, "Surface structure of few layer graphene," *Carbon*, vol. 136, pp. 255–261, 2018, doi: 10.1016/j.carbon.2018.04.089.

[57] Z. Fakharan, L. Naji, and K. Madanipour, "Surface roughness regulation of reduced-graphene oxide/iodine – Based electrodes and their application in polymer solar cells," *J. Colloid Interface Sci.*, vol. 540, pp. 272–284, 2019, doi: 10.1016/j.jcis.2019.01.029.

[58] D. S. Wastl, A. J. Weymouth, and F. J. Giessibl, "Atomically Resolved Graphitic Surfaces in Air by Atomic Force Microscopy," *ACS Nano*, vol. 8, no. 5, pp. 5233–5239, 2014, doi: 10.1021/nn501696q.

[59] P. Järvinen *et al.*, "Molecular Self-Assembly on Graphene on SiO2and h-BN Substrates," *Nano Lett.*, vol. 13, pp. 3199–3204, 2013, doi: 10.1021/nl401265f.

[60] H. Lian, L. Qi, J. Luo, and K. Hu, "Experimental study and mechanism analysis on the effect of substrate wettability on graphene sheets distribution morphology within uniform printing droplets," *J. Phys.: Condens. Matter*, vol. 30, no. 33, p. 335001, 2018, doi: 10.1088/1361-648X/aad34e.

[61] A. L. Gorkina *et al.*, "Transparent and conductive hybrid graphene/carbon nanotube films," *Carbon*, vol. 100, pp. 501–507, 2016, doi: 10.1016/j.carbon.2016.01.035.

[62] M. S. Dresselhaus, A. Jorio, A. G. Souza Filho, and R. Saito, "Defect characterization in graphene and carbon nanotubes using Raman spectroscopy," *Proc. R. Soc. A*, vol. 368, no. 1932, pp. 5355–5377, 2010, doi: 10.1098/rsta.2010.0213.

[63] D. Cohen-Tanugi and J. C. Grossman, "Water Desalination across Nanoporous Graphene," *Nano Lett.*, vol. 12, no. 7, pp. 3602–3608, 2012, doi: 10.1021/nl3012853.

[64] P. Russo, A. Hu, and G. Compagnini, "Synthesis, Properties and Potential Applications of Porous Graphene: A Review," *Nano-Micro Lett.*, vol. 5, no. 4, pp. 260–273, 2013, doi: 10.1007/BF03353757.

[65] Y. Yang, L. Xu, H. Wang, W. Wang, and L. Zhang, "TiO2 /graphene porous composite and its photocatalytic degradation of methylene blue," *Mater. Des*, vol. 108, pp. 632–639, Oct. 2016, doi: 10.1016/j.matdes.2016.06.104.

[66] N. Yousefi, X. Lu, M. Elimelech, and N. Tufenkji, "Environmental performance of graphene-based 3D macrostructures," *Nat. Nanotechnol.*, vol. 14, no. 2, pp. 107–119, 2019, doi: 10.1038/s41565-018-0325-6.

[67] C. Su *et al.*, "Tandem Catalysis of Amines Using Porous Graphene Oxide," *J. Am. Chem. Soc.*, vol. 137, no. 2, pp. 685–690, 2015, doi: 10.1021/ja512470t.

[68] C. Yu *et al.*, "Engineering nano-porous graphene oxide by hydroxyl radicals," *Carbon*, vol. 105, pp. 291–296, 2016, doi: 10.1016/j.carbon.2016.04.050.

[69] T. Osaki, "Effect of sol–gel conditions on BET surface area, pore volume, mean pore radius, palladium dispersion, palladium particle size, and catalytic CO oxidation activity of Pd/Al2O3 cryogels," *J. Porous Mater.*, vol. 25, no. 3, pp. 697–711, 2018, doi: 10.1007/s10934-017-0483-1.

[70] D. Y. Kim *et al.*, "Graphene paper with controlled pore structure for high-performance cathodes in Li–O 2 batteries," *Carbon*, vol. 100, pp. 265–272, 2016, doi: 10.1016/j.carbon.2016.01.013.

[71] L. The Vinh, T. Ngoc Khiem, H. Dang Chinh, P. V. Tuan, and V. T. Tan, "Adsorption capacities of reduced graphene oxide: effect of reductants," *Mater. Res. Express*, vol. 6, no. 7, p. 075615, 2019, doi: 10.1088/2053-1591/ab1862.

[72] V. Chabot, B. Kim, B. Sloper, C. Tzoganakis, and A. Yu, "High yield production and purification of few layer graphene by Gum Arabic assisted physical sonication," *Sci Rep*, vol. 3, no. 1, p. 1378, Dec. 2013, doi: 10.1038/srep01378.

[73] Y. Zhang *et al.*, "Defect-like Structures of Graphene on Copper Foils for Strain Relief Investigated by High-Resolution Scanning Tunneling Microscopy," *ACS Nano*, vol. 5, no. 5, pp. 4014–4022, 2011, doi: 10.1021/nn200573v.

[74] Y. Lu, H. Lyu, A. G. Richardson, T. H. Lucas, and D. Kuzum, "Flexible Neural Electrode Array Based-on Porous Graphene for Cortical Microstimulation and Sensing," *Sci. Rep.*, vol. 6, no. 1, p. 33526, 2016, doi: 10.1038/srep33526.

[75] J. P. Smith, C. W. Foster, J. P. Metters, O. B. Sutcliffe, and C. E. Banks, "Metallic Impurities in Graphene Screen-Printed Electrodes Can Influence Their Electrochemical Properties," *Electroanalysis*, vol. 26, no. 11, pp. 2429–2433, 2014, doi: 10.1002/elan.201400320.

[76] S. S. Shams, R. Zhang, and J. Zhu, "Graphene synthesis: a Review," *Mater. Sci.-Poland*, vol. 33, no. 3, pp. 566–578, 2015, doi: 10.1515/msp-2015-0079.

[77] L. Stobinski *et al.*, "Graphene oxide and reduced graphene oxide studied by the XRD, TEM and electron spectroscopy methods," *J. Electron Spectrosc.*, vol. 195, pp. 145–154, 2014, doi: 10.1016/j.elspec.2014.07.003.

[78] K. Krishnamoorthy, M. Veerapandian, K. Yun, and S.-J. Kim, "The chemical and structural analysis of graphene oxide with different degrees of oxidation," *Carbon*, vol. 53, pp. 38–49, 2013, doi: 10.1016/j.carbon.2012.10.013.

[79] K. H. Thebo, X. Qian, Q. Wei, Q. Zhang, H.-M. Cheng, and W. Ren, "Reduced graphene oxide/metal oxide nanoparticles composite membranes for highly efficient molecular separation," *J. Mater. Sci. Technol.*, vol. 34, no. 9, pp. 1481–1486, 2018, doi: 10.1016/j.jmst.2018.05.008.

[80] R. F. Egerton, P. Li, and M. Malac, "Radiation damage in the TEM and SEM," *Micron*, vol. 35, no. 6, pp. 399–409, 2004, doi: 10.1016/j.micron.2004.02.003.

[81] A. Bellunato, H. Arjmandi Tash, Y. Cesa, and G. F. Schneider, "Chemistry at the Edge of Graphene," *ChemPhysChem*, vol. 17, no. 6, pp. 785–801, 2016, doi: 10.1002/cphc.201500926.

[82] K. A. Mkhoyan *et al.*, "Atomic and Electronic Structure of Graphene-Oxide," *Nano Lett.*, vol. 9, no. 3, pp. 1058–1063, 2009, doi: 10.1021/nl8034256.

[83] R. F. Egerton, "Electron energy-loss spectroscopy in the TEM," *Rep. Prog. Phys.*, vol. 72, no. 1, p. 016502, 2009, doi: 10.1088/0034-4885/72/1/016502.

[84] A. Iwan *et al.*, "Optical and electrical properties of graphene oxide and reduced graphene oxide films deposited onto glass and Ecoflex® substrates towards organic solar cells," *Adv. Mater. Lett.*, vol. 9, no. 1, pp. 58–65, 2018, doi: 10.5185/amlett.2018.1870.

[85] L. K. Putri *et al.*, "Tailoring the properties of oxygenated graphene with different oxidation degrees for noble-metal-free photocatalytic hydrogen evolution," *Catal. Today*, vol. 315, pp. 93–102, 2018, doi: 10.1016/j.cattod.2018.04.009.

[86] F. Giannazzo *et al.*, "Nanoscale electrical mapping of two-dimensional materials by conductive atomic force microscopy for transistors applications," presented at the EMERGING TECHNOLOGIES: MICRO TO NANO (ETMN-2017): Proceedings of the 3rd International Conference on Emerging Technologies: Micro to Nano, 2018, p. 020008, doi: 10.1063/1.5047762.

[87] M. Ahmad, S. A. Han, D. H. Tien, J. Jung, and Y. Seo, "Local conductance measurement of graphene layer using conductive atomic force microscopy," *J. Appl. Phys.*, vol. 110, no. 5, p. 054307, 2011, doi: 10.1063/1.3626058.

[88] C. Tan, J. Rodríguez-López, J. J. Parks, N. L. Ritzert, D. C. Ralph, and H. D. Abruña, "Reactivity of Monolayer Chemical Vapor Deposited Graphene Imperfections Studied Using Scanning Electrochemical Microscopy," *ACS Nano*, vol. 6, no. 4, pp. 3070–3079, 2012, doi: 10.1021/nn204746n.

[89] J. Molina, J. Fernández, J. C. Inés, A. I. del Río, J. Bonastre, and F. Cases, "Electrochemical characterization of reduced graphene oxide-coated polyester fabrics," *Electrochim. Acta*, vol. 93, pp. 44–52, 2013, doi: 10.1016/j.electacta.2013.01.071.

[90] A. J. Bard, G. Denuault, C. Lee, D. Mandler, and D. O. Wipf, "Scanning electrochemical microscopy - a new technique for the characterization and modification of surfaces," *Acc. Chem. Res.*, vol. 23, no. 11, pp. 357–363, Nov. 1990, doi: 10.1021/ar00179a002.

[91] I. Rodriguez-Pastor, G. Ramos-Fernandez, H. Varela-Rizo, M. Terrones, and I. Martin-Gullon, "Towards the understanding of the graphene oxide structure: How to control the formation of humic- and fulvic-like oxidized debris," *Carbon*, vol. 84, pp. 299–309, 2015, doi: 10.1016/j.carbon.2014.12.027.

[92] S. Drewniak, R. Muzyka, A. Stolarczyk, T. Pustelny, M. Kotyczka-Morańska, and M. Setkiewicz, "Studies of Reduced Graphene Oxide and Graphite Oxide in the Aspect of Their Possible Application in Gas Sensors," *Sensors*, vol. 16, no. 1, p. 103, 2016, doi: 10.3390/s16010103.

[93] L. Song *et al.*, "Effect of high-temperature thermal treatment on the structure and adsorption properties of reduced graphene oxide," *Carbon*, vol. 52, pp. 608–612, 2013, doi: 10.1016/j.carbon.2012.09.060.

[94] T. A. Revathy, S. Dhanavel, T. Sivaranjani, V. Narayanan, T. Maiyalagan, and A. Stephen, "Highly active graphene-supported palladium-nickel alloy nanoparticles for catalytic reduction of 4-nitrophenol," *Appl. Surf. Sci.*, vol. 449, pp. 764–771, 2018, doi: 10.1016/j.apsusc.2018.01.280.

[95] M. Tripathi *et al.*, "Implanting Germanium into Graphene," *ACS Nano*, vol. 12, no. 5, pp. 4641–4647, May 2018, doi: 10.1021/acsnano.8b01191.

[96] M. Celebi, K. Karakas, I. E. Ertas, M. Kaya, and M. Zahmakiran, "Palladium Nanoparticles Decorated Graphene Oxide: Active and Reusable Nanocatalyst for the Catalytic Reduction of Hexavalent Chromium(VI)," *ChemistrySelect*, vol. 2, no. 27, pp. 8312–8319, 2017, doi: 10.1002/slct.201700967.

[97] S. N. Alam, N. Sharma, and L. Kumar, "Synthesis of Graphene Oxide (GO) by Modified Hummers Method and Its Thermal Reduction to Obtain Reduced Graphene Oxide (rGO)*," *Graphene*, vol. 06, no. 01, pp. 1–18, 2017, doi: 10.4236/graphene.2017.61001.

[98] A. Pendashteh, J. Palma, M. Anderson, and R. Marcilla, "NiCoMnO 4 nanoparticles on N-doped graphene: Highly efficient bifunctional electrocatalyst for oxygen reduction/evolution reactions," *Appl. Catal. B Environ.*, vol. 201, pp. 241–252, 2017, doi: 10.1016/j.apcatb.2016.08.044.

[99] D. Jembrih-Simbürger *et al.*, "The colour of silver stained glass—analytical investigations carried out with XRF, SEM/EDX, TEM, and IBA," *J. Anal. At. Spectrom.*, vol. 17, no. 4, pp. 321–328, 2002, doi: 10.1039/B111024C.

[100] M. K. Tiwari, A. K. Singh, and K. J. S. Sawhney, "Sample Preparation for Evaluation of Detection Limits in X-ray Fluorescence Spectrometry," *Anal. Sci.*, vol. 21, no. 2, pp. 143–147, 2005, doi: 10.2116/analsci.21.143.

[101] F. L. Melquiades and C. R. Appoloni, "Application of XRF and field portable XRF for environmental analysis," *J. Radioanal. Nucl. Chem.*, vol. 262, no. 2, pp. 533–541, 2004, doi: 10.1023/B:JRNC.0000046792.52385.b2.

[102] O. Jankovský, A. Libánská, D. Bouša, D. Sedmidubský, S. Matějková, and Z. Sofer, "Partially Hydrogenated Graphene Materials Exhibit High Electrocatalytic Activities Related to Unintentional Doping with Metallic Impurities," *Chem. Eur. J.*, vol. 22, no. 25, pp. 8627–8634, 2016, doi: 10.1002/chem.201600811.

[103] R. Linke and M. Schreiner, "Energy Dispersive X-Ray Fluorescence Analysis and X-Ray Microanalysis of Medieval Silver Coins," *Microchimica Acta*, vol. 133, no. 1–4, pp. 165–170, 2000, doi: 10.1007/s006040070087.

[104] A. M. Venezia, "X-ray photoelectron spectroscopy (XPS) for catalysts characterization," *Catal. Today*, vol. 77, no. 4, pp. 359–370, 2003, doi: 10.1016/S0920-5861(02)00380-2.

[105] F. Reniers and C. Tewell, "New improvements in energy and spatial (x, y, z) resolution in AES and XPS applications," *J. Electron Spectrosc.*, vol. 142, no. 1, pp. 1–25, 2005, doi: 10.1016/j.elspec.2004.07.004.

[106] D. R. Baer and M. H. Engelhard, "XPS analysis of nanostructured materials and biological surfaces," *J. Electron Spectrosc.*, vol. 178–179, pp. 415–432, 2010, doi: 10.1016/j.elspec.2009.09.003.

[107] C. Chang, "AUGER ELECTRON SPECTROSCOPY," *Surf. Sci.*, vol. 25, pp. 53–79, 1971, doi: 10.1016/0039-6028(71)90210-X.

[108] C. J. Powell, A. Jablonski, I. S. Tilinin, S. Tanuma, and D. R. Penn, "Surface sensitivity of Auger-electron spectroscopy and X-ray photoelectron spectroscopy," *J. Electron Spectrosc.*, vol. 98–99, pp. 1–15, 1999, doi: 10.1016/S0368-2048(98)00271-0.

[109] M. Xu, D. Fujita, J. Gao, and N. Hanagata, "Auger Electron Spectroscopy: A Rational Method for Determining Thickness of Graphene Films," *ACS Nano*, vol. 4, no. 5, pp. 2937–2945, 2010, doi: 10.1021/nn100276w.

[110] L. Zhang, Y. Shi, L. Wang, and C. Hu, "AgBr-wrapped Ag chelated on nitrogen-doped reduced graphene oxide for water purification under visible light," *Appl. Catal. B Environ.*, vol. 220, pp. 118–125, 2018, doi: 10.1016/j.apcatb.2017.08.038.

[111] G. R. Bhimanapati, M. Wetherington, S. Mahabir, and J. A. Robinson, "Synthesis and radiation response of BCON: a graphene oxide and hexagonal boron nitride hybrid," *2D Mater.*, vol. 3, no. 2, p. 025028, 2016, doi: 10.1088/2053-1583/3/2/025028.

[112] L. Shen *et al.*, "Analysis of oxidation degree of graphite oxide and chemical structure of corresponding reduced graphite oxide by selecting different-sized original graphite," *RSC Adv.*, vol. 8, no. 31, pp. 17209–17217, 2018, doi: 10.1039/C8RA01486H.

[113] A. Eckmann *et al.*, "Probing the Nature of Defects in Graphene by Raman Spectroscopy," *Nano Lett.*, vol. 12, no. 8, pp. 3925–3930, 2012, doi: 10.1021/nl300901a.

[114] E. Kymakis, K. Savva, M. M. Stylianakis, C. Fotakis, and E. Stratakis, "Flexible Organic Photovoltaic Cells with In Situ Nonthermal Photoreduction of Spin-Coated Graphene Oxide Electrodes," *Adv. Funct. Mater.*, vol. 23, no. 21, pp. 2742–2749, 2013, doi: 10.1002/adfm.201202713.

[115] F. Torrisi *et al.*, "Inkjet-Printed Graphene Electronics," *ACS Nano*, vol. 6, no. 4, pp. 2992–3006, 2012, doi: 10.1021/nn2044609.

[116] M. Lotya, P. J. King, U. Khan, S. De, and J. N. Coleman, "High-Concentration, Surfactant-Stabilized Graphene Dispersions," *ACS Nano*, vol. 4, no. 6, pp. 3155–3162, 2010, doi: 10.1021/nn1005304.

[117] E. B. Secor, S. Lim, H. Zhang, C. D. Frisbie, L. F. Francis, and M. C. Hersam, "Gravure Printing of Graphene for Large-area Flexible Electronics," *Adv. Mater.*, vol. 26, no. 26, pp. 4533–4538, 2014, doi: 10.1002/adma.201401052.

[118] G. Wang, B. Wang, J. Park, J. Yang, X. Shen, and J. Yao, "Synthesis of enhanced hydrophilic and hydrophobic graphene oxide nanosheets by a

solvothermal method," *Carbon*, vol. 47, no. 1, pp. 68–72, 2009, doi: 10.1016/j.carbon.2008.09.002.

[119] D. C. Marcano *et al.*, "Improved Synthesis of Graphene Oxide," *ACS Nano*, vol. 4, no. 8, pp. 4806–4814, 2010, doi: 10.1021/nn1006368.

[120] G. Gonçalves *et al.*, "Breakdown into nanoscale of graphene oxide: Confined hot spot atomic reduction and fragmentation," *Sci Rep*, vol. 4, no. 1, p. 6735, 2015, doi: 10.1038/srep06735.

[121] S. Kumar, A. Garg, and A. Chowdhuri, "Sonication effect on graphene oxide (GO) membranes for water purification applications," *Mater. Res. Express*, vol. 6, no. 8, p. 085620, May 2019, doi: 10.1088/2053-1591/ab1ffd.

[122] V. Mazánek, S. Matějková, D. Sedmidubský, M. Pumera, and Z. Sofer, "One-Step Synthesis of B/N Co-doped Graphene as Highly Efficient Electrocatalyst for the Oxygen Reduction Reaction: Synergistic Effect of Impurities," *Chem. Eur. J.*, vol. 24, no. 4, pp. 928–936, 2018, doi: 10.1002/chem.201704515.

[123] L. Wang, Z. Sofer, J. Luxa, and M. Pumera, "Nitrogen doped graphene: influence of precursors and conditions of the synthesis," *J. Mater. Chem.*, no. 2, pp. 2887–2893, 2014, doi: 10.1039/c3tc32359e.

[124] I. Barbolina, C. R. Woods, N. Lozano, K. Kostarelos, K. S. Novoselov, and I. S. Roberts, "Purity of graphene oxide determines its antibacterial activity," *2D Materials*, vol. 3, no. 2, p. 025025, 2016, doi: 10.1088/2053-1583/3/2/025025.

[125] L. Gao, W. Zhuge, X. Feng, W. Sun, X. Sun, and G. Zheng, "Co/rGO synthesized *via* the alcohol-thermal method as a heterogeneous catalyst for the highly efficient oxidation of ethylbenzene with oxygen," *New J. Chem.*, vol. 43, no. 21, pp. 8189–8194, 2019, doi: 10.1039/C9NJ00470J.

[126] M. Bacon, S. J. Bradley, and T. Nann, "Graphene Quantum Dots," *Part. Part. Syst. Charact.*, vol. 31, no. 4, pp. 415–428, 2014, doi: 10.1002/ppsc.201300252.

[127] G. Eda *et al.*, "Blue Photoluminescence from Chemically Derived Graphene Oxide," *Adv. Mater.*, vol. 22, no. 4, pp. 505–509, 2010, doi: 10.1002/adma.200901996.

[128] Z. Wang, H. Zeng, and L. Sun, "Graphene quantum dots: versatile photoluminescence for energy, biomedical, and environmental applications," *J. Mater. Chem. C*, vol. 3, no. 6, pp. 1157–1165, 2015, doi: 10.1039/C4TC02536A.

[129] M. Li, S. K. Cushing, X. Zhou, S. Guo, and N. Wu, "Fingerprinting photoluminescence of functional groups in graphene oxide," *J. Mater. Chem.*, vol. 22, no. 44, p. 23374, 2012, doi: 10.1039/c2jm35417a.

[130]C. T. Chien *et al.*, "Tunable Photoluminescence from Graphene Oxide," *Angew. Chem. Int. Ed.*, vol. 51, no. 27, pp. 6662–6666, 2012, doi: 10.1002/anie.201200474.

[131]L. Tang *et al.*, "Deep Ultraviolet to Near-Infrared Emission and Photoresponse in Layered N-Doped Graphene Quantum Dots," *ACS Nano*, vol. 8, no. 6, pp. 6312–6320, 2014, doi: 10.1021/nn501796r.

[132]M. Mohandoss, "Solar mediated reduction of graphene oxide," *RSC Adv.*, vol. 7, pp. 957–963, 2017, doi: 10.1039/c6ra24696f.

[133]C. Cheng, S. Li, A. Thomas, N. A. Kotov, and R. Haag, "Functional Graphene Nanomaterials Based Architectures: Biointeractions, Fabrications, and Emerging Biological Applications," *Chem. Rev.*, vol. 117, no. 3, pp. 1826–1914, 2017, doi: 10.1021/acs.chemrev.6b00520.

[134]H. Jin *et al.*, "Emerging Two-Dimensional Nanomaterials for Electrocatalysis," *Chem. Rev.*, vol. 118, no. 13, pp. 6337–6408, 2018, doi: 10.1021/acs.chemrev.7b00689.

2 Aim of the work

Fifteen years ago, graphene and its exceptional properties have been discovered [1-2]. This led to a great hype to use this material in semiconductor industry. In many proof-of-concept studies the potential of the material was clearly demonstrated, but up to now there are only a few applications reported which have already arrived at market [3]. The reason for that can be found in the complexity of synthesis and transfer of 2D carbon materials. Either the quality of the material can be controlled in an acceptable way or the transfer of such a material is feasible, but never both at the same time can be achieved.

Therefore, the aim of this work is to investigate the synthesis of GO in a large batch. First, by synthesizing graphene via chemical exfoliation, different ionic impurities are introduced which have to be controlled. Due to this, a method needs to be established in order to determine these contaminations qualitatively and quantitatively after synthesis. Second, graphene suspensions are containing a large ensemble of graphene flakes with different lateral flake sizes ranging from several nanometres up to few micrometres. Based on this, the graphene lateral flake size must be controlled, characterized and if necessary designed. Third, the quality of graphene is described by the number of defects within the carbon lattice. Here, a technique is needed, which characterizes the number as well as the kind of these defects satisfactory within graphene flakes. Furthermore, all characterization techniques used are evaluated in terms of scalability and throughput for the characterization of graphene.

Finally, the insights gained from the detailed graphene material characterization should be used to transfer the graphene suspensions on interdigitated gold structures with the aim to fabricate integrated microsensor devices suitable for gas sensing.

3 Experimental

The following chapter covers the materials and chemicals used. Moreover, the protocols for GO synthesis, purification, system integration of GO suspensions and methods applied for characterization and measurements are described.

3.1 Materials

Both types of graphite (flake graphite 22003 and flake graphite 22599.5) were purchased from Thielmann Graphite GmbH & Co KG. Sodium nitrate (> 99%) was obtained from Alfa Aesar, potassium permanganate (p.a.) from Merck, Sulphuric acid (96% (w/w) VLSI Selectipur*) from BASF, hydrochloric acid (37% (w/w) chem. rein) from Brenntag and hydrogen peroxide (30% (w/w)) from Technic. Triton X was purchased from Sigma Aldrich. All chemicals were used as received without further purification. Deionized water, was obtained through the company's own water desalination and purification of Infineon Technologies AG Regensburg.

Synthetic air (N_2: (80%, O_2: 20% (v/v)), forming gas (H_2: 4%, N_2: 96% (v/v)) and oxygen gas (99.9999%) were purchased from Linde Electronics. NO_2 Ecocyl® gas bottles (0.1% (v/v) in synthetic air) were obtained from Linde.

3.2 Synthesis and Purification of Graphene Oxide

To investigate the reproducibility of the chemical exfoliation of graphite, two different batches of the starting material have been studied, which differ in their flake size and purity. Each synthesis was repeated under the exactly same conditions for three times. The flake graphite 22599.5 was used for GO batches A1 - A3, GO batches B1 - B3 were made with the flake graphite 22003. The difference between both graphite starting materials is the carbon content, which was specified by the manufacturer as followed: > 99% carbon content for 22599.5 graphite and > 87% carbon content for the 22003 graphite.

GO was prepared by a modified Hummers method [4]. Here, 6.0 g of flake graphite was placed in a double-walled flask together with 4.5 g $NaNO_3$ and filled up by 450 mL of H_2SO_4. The coolant between the double-wall of the flask was kept at 25 °C, controlled by an external thermostat. 27.0 g $KMnO_4$ was added in small portions and the mixture was stirred for three days. For the next step 450 mL of 5% H_2SO_4 was added to the mixture, which was then heated to 80 °C and stirred for 2 h. After adding 90 mL of 36% H_2O_2, the mixture was allowed to stand for 9 h at 25 °C with sparing stirring to reduce the remaining $KMnO_4$. For the purification of GO, two solutions were prepared to remove ions of oxidant origin such as manganese or sodium ions. Solution I consists of 3% H_2SO_4 and 0.5% H_2O_2, solution II contains 3% HCl. Initially, the reaction mixture was divided to four 200 mL cups and centrifuged at 3175 rcf for 60 min. The clear supernatant was removed; the cups were refilled with solution I and shaken to disperse the GO flakes again, before the mixture was centrifuged at 3175 rcf for 15 min. This procedure was repeated four times with solution I and twice with solution II. The cups were refilled with water and shaken to disperse the GO flakes. The mixture was then allowed to stand for another three days. Next, the mixture was centrifuged at 3175 rcf for 60 min. The yellow-brown coloured supernatant was discarded, and the cups were again filled with water, shaken and centrifuged 3175 rcf for 120 min. Subsequently, the aqueous suspension of blended reaction mixture was centrifuged at 3175 rcf for 5 min, this time the supernatant was collected in a 2 L flask, which was then filled up with water,

while the sediment was discarded. The product was dialysed with a total amount of 8 L of water. During the diafiltrating (every 2 L) small amounts of the mixture were sampled and analysed by ICP-AES.

After centrifugation, the GO was further purified via dialysis, until 8 L of permeate were run through the filter. Figure 6 shows a schematic illustration of the KrosFlow research II TFF System from Repligen which was used for dialysis with a flow rate of 70 mL/min and a maximal pressure limit of 1.1 bar.
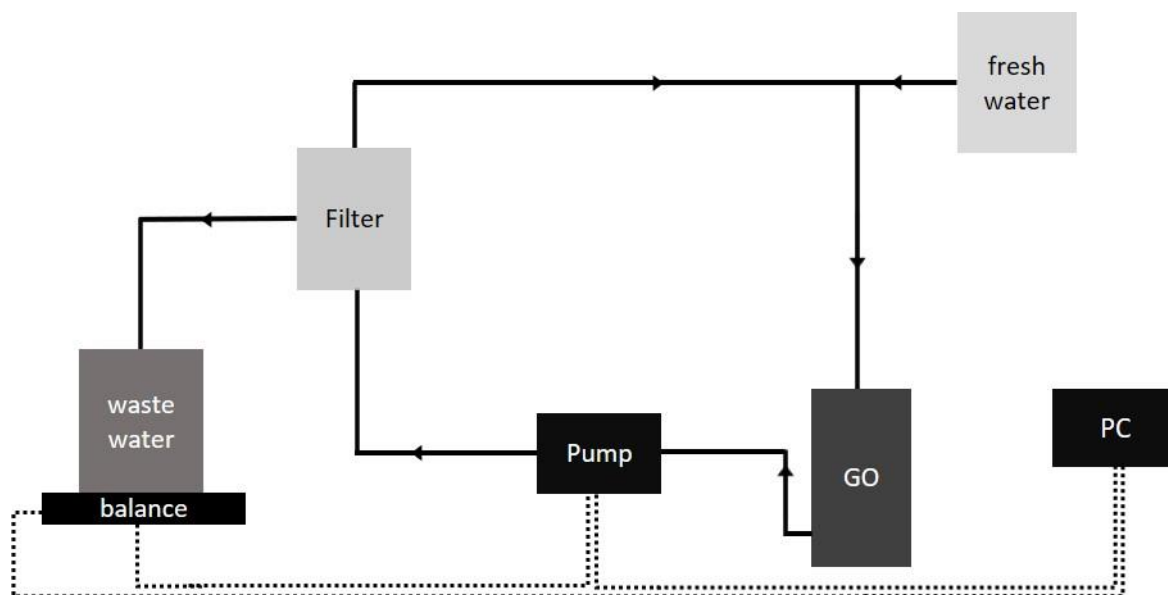

Figure 6. The schematic illustration of the "*KrosFlow research II TFF System*"- dialysis setup. The solid lines show the flow circle of dialysis and the dashed line the communication between the computer (PC), the pump and the balance. The communication enables the automatic performance, recognizes the possible clogging of the filter, and stops the dialysis after the desired volume. Here, the pump presses the GO sudspension through a filter membrane (cut-off: 750 kDa). A certain part of the water including impurities gets removed from the suspension. To avoid any enrichment from GO, fresh water is introduced into the system and keeps the GO concentration constant. The water is collected on a balance which communicates with an PC and the pump. If the desired volume of dialysis is reached, the whole system stops automatically.

Sonication: GO suspensions were sonicated by a Bandelin Sonopuls HD2200 ultrasonic device with a VS200T probe using a frequency of 20 kHz at 35% (maximal power output 200 W).

3.3 Characterization Methods

Gravimetric Analysis

The mass concentration of the GO batches was determined by gravimetry with a Mettler AT261 DeltaRange balance. The error of the gravimetric analysis was calculated for all six GO batches (A1 - A3 and B1 - B3) according to the protocol in the appendix.

Inductively Coupled Plasma - Atomic Emission Spectrometry

A Thermo Fisher iCAP 6300 duo was used for the quantification of contaminations of GO suspensions. GO suspensions were diluted to 0.5 mg/mL. All permeates of the dialysis were analysed without further sample preparation. For the calibration of the ICP-AES device a multi-elemental standard was used.

All ICP-AES measurements were done by Dr. Josef Steiner in the Failure Analysis of Infineon Technologies AG Regensburg.

UV-Vis Spectroscopy

Spectra were recorded in a quartz cuvette (10 mm) at a GO concentration of 0.025 mg/mL. The absorbance spectra were recorded on a Cary 50 Bio UV-Visible spectrometer from Varian.

Raman Spectroscopy

Raman spectra were recorded by a Thermo Scientific DXR Raman microscope equipped with a 532 nm excitation laser. The excitation power for all measurements was set to 8 mW and the exposure time was 0.2 s with 40 exposures. A gold coated silicon wafer was used as substrate. The sample was drop-casted (10 µL of GO suspensions (2 mg/mL)) onto the substrate and dried at ambient environment before measurement.

X-ray Photoelectron Spectroscopy

XPS spectra were recorded (2020) using a Thermo Fisher Scientific NEXSA spectrometer at Technische Hochschule Deggendorf in Taisnach. Excitation was done by monochromatic Al-K$_\alpha$ radiation (1486.6 eV) with a 400 µm beam diameter. Charge compensation was done by flooding the sample simultaneously with low energy electrons and Ar-ions. Survey spectra were recorded with a pass energy of 200 eV, detail spectra with a pass energy of 50 eV and averaging over 5 scans. C$_{KLL}$ spectra were recorded with a pass energy of 100 eV and averaging over 100 scans to provide a good S/N ratio. The measurements were done by Dr. Günther Ruhl.

XPS spectra recorded in 2016 were recorded using a ThermoFisher Escalab 250 Xi at Osram Opto Semiconductors GmbH in Regensburg. Excitation was done by monochromatic Al-K$_\alpha$ radiation (1486.6 eV) with a 650 µm beam diameter. Detail spectra with a pass energy of 20 eV and averaging over 3 scans.

Nuclear Magnetic Resonance – Relaxation Time

The experiments were made on an Acorn Area Quant from Xigo Nanotools. All samples (4 scans per measurement) were measured with the "T2 Carr Purcell–Meiboom–Gill mode" [5].

Dynamic Light Scattering

All measurements (3 scans per sample) were performed at 20 °C with a Malvern Zatasizer Nano-ZS at a GO concentration of 0.025 mg/mL.

Electron Microscopy

SEM images were recorded on a Jeol 6700 with an acceleration voltage of 5 kV. GO suspension was diluted to 0.002 mg/mL, Trition X (0.280 µL per 10 mL GO suspension) was added and the mixture was drop-casted on a Si_3N_4 wafer. Finally, the sample was heated up to 200 °C for 1 min to remove the Trition X.

3.4 Design of Sensor Chips

The chips were obtained from the production line of Infineon Technology AG Regensburg. Every single sensor chip contains 8 sensor fields, each with a separated heater and sensing structure. The heater is located underneath the interdigit gold sensing structure and is used to heat up the sensor to the desired temperature; up to 350 °C by applying electrical current. On a Si_3N_4 layer with a thickness of 550 nm an interdigit gold structure (500 nm) is metalized and contains 22 gold fingers on each side. The width and the distance of the gold fingers is 6 µm. The area of one sensor field is 500 µm times 500 µm. Figure 7 (A) depicts the layout of one sensor chip (containing 8 sensor fields). Figure 7 (B) compares the size between one sensor chip and a one Cent coin.
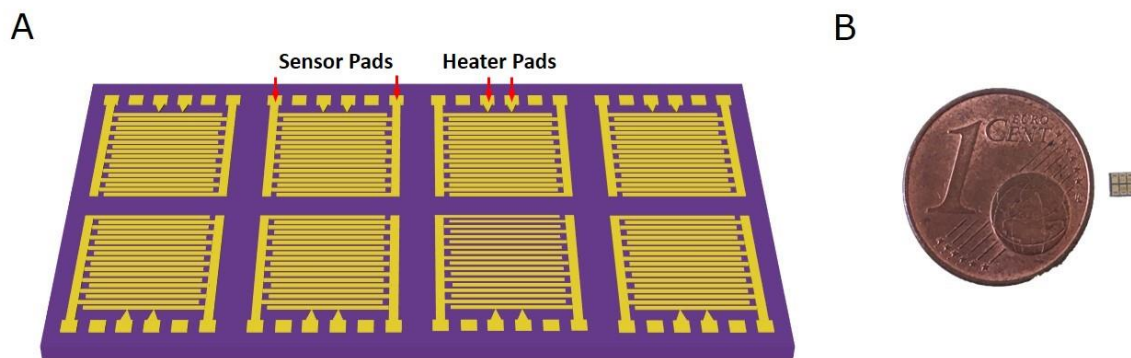

Figure 7. (A) Scheme of one sensor chip containing 8 sensor fields with an interdigit finger structure (yellow). One sensor field has an area of 500 µm x 500 µm. With the outer gold contact pads of each sensor field, the resistance of the sensor layer is measured. With the inner contact pads the sensor heater structure which is hidden under the interdigit structure can be controlled. Under the gold structure is an insulating silicon nitride layer (violet). The last two contact pads are not connected. **(B)** The size comparison of one sensor chip with eight sensor fields like in **(A)** compared with a one Cent coin.

3.5 Graphene Oxide Deposition

To deposit GO suspensions on the sensor device a VIEWEG F7000NV dispensing robot was used in combination with a micro-dispensing valve VERMES MDV 3200+ that was operated by the micro-dispensing controller VERMES MVC 3200+. The robot uses a CCD camera to allow the accurate alignment of the dispensing tip over the work piece. The position was adjusted automatically by optical image control (Figure 8).
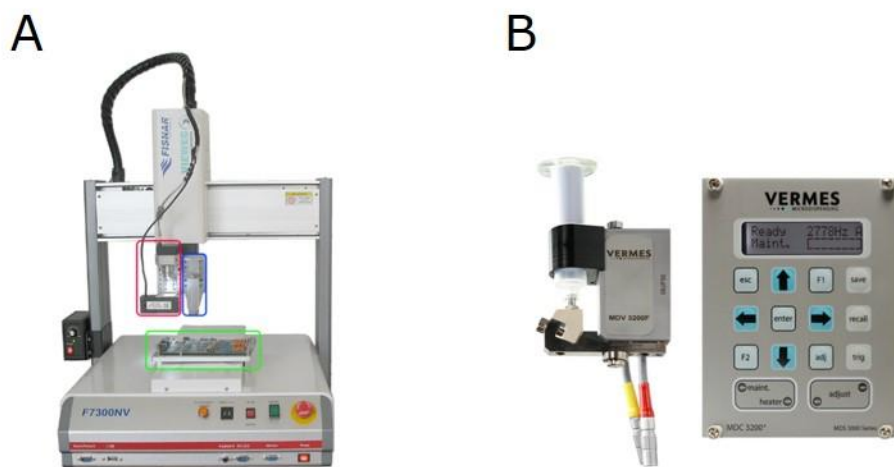

Figure 8. Computer controlled micro-dispensing tool which deposits the ink (GO suspension) on the sensor structure. **(A)** VIEWEG F7000NV Dispensing: The robot arm can move in x-, y-, z-direction. **Green:** The hot plate and sample stage. **Red:** The camera with light source for optical control. **Blue:** The micro-dispensing unit. **(B)** VERMES micro-dispensing valve MDV 3200+ and VERMES micro-dispensing controller MDC 3200+.

A number of parameters, which can be divided into two categories, influence the GO deposition: First, parameters which have no influence on the deposited amount of GO, e.g., the chuck temperature (50 °C), and the dispense height (0.2 mm). With the chuck temperature, the evaporation of GO suspension is controlled, and coffee-ring effect can be minimized. The dispense height is the distance from chip to nozzle and has an influence on the GO spot size. The second part of the parameters influences the amount of dispensed GO. These parameters have been set to the values given in Table 1.

Table 1. Dispensing parameters which have an influence on the deposited GO amount.

Nozzle size μm	Needle lift %	Pressure mbar	T_{Rising} ms	$T_{Falling}$ ms	T_{Open} ms	T_{Delay} ms
70	35	61	0.3	0.3	0.3	2.4

The nozzle size is defined as the diameter of the opening hole through which the GO suspension is deposited on the sensor structure. The needle lift represents the ram stroke of the needle and means the distance, how far the needle is going up during one dispense shot. The pressure is necessary for the GO suspension to be pressed from the reservoir through the dispensing tool to the dispensing nozzle. T_{Rising} respectively $T_{Falling}$ are the times how long it takes for the valve to open and to close. T_{Delay} is the time between one completed dispensing cycle and the next cycle. The time had to be set to 2.4 ms to avoid double dispensing of the same spot.

Before dispensing can takes place, the chips were exposed to an oxygen plasma (20 s, 40 W) to remove organic impurities like remaining photoresist or other residues coming from the production and to improve the wetting properties for the deposition of GO suspensions, and to avoid any coffee-ring formation which reduces the sensor layer homogeneity. This step was done with a Myplass III from Plasma Electronic.

After the dispensing the deposited GO will be thermally reduced with a Jetfirst 300C from Jipelec. This RTP is necessary, to obtain rGO which contains a larger sp^2–hybridized system and therefore shows an increased conductivity, and it was performed with the following settings: Heating rate: 37.5 °C/s up to 400 °C for 20 min under forming gas (containing 4% H_2 and 96% N_2). Before and after the RTP process the reaction-chamber was flushed three times with nitrogen gas. Between the cleaning steps, vacuum was esthablished in the chamber. A scheme of the used RTP device is shown in Figure 9.
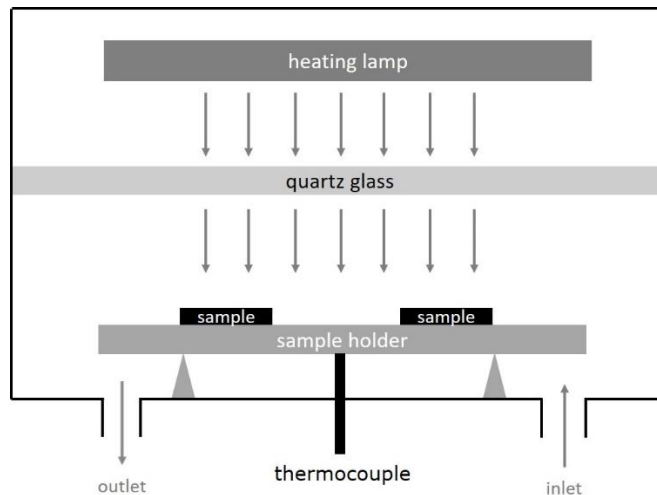
Figure 9. A scheme of an RTP oven. The upper part contains the heating lamp and is separated to the reaction chamber by a quartz glass. Over the inlet the desired gas runs into the chamber. Over the outlet vacuum can be drawn or the gas can leave the chamber.

Finally, the chips were mounted on PCB-boards from *Hofmann Leiterplatten* (with 50 contacts) and subsequently bonded with gold wires providing electrical contact (Figure 10). Mounting and bonding was done in the production line of Infineon Technologies AG Regensburg.
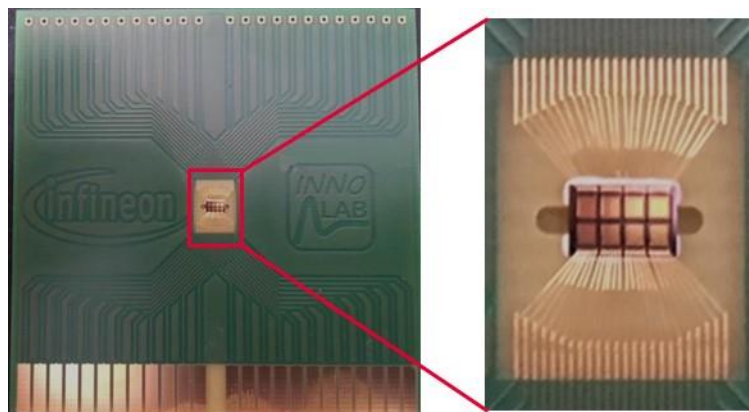

Figure 10. The fully engineered sensor on a PCB-board and ready for gas measurements. On the bottom the broad band contact pads for electrical signal transmission from all 8 sensors and heaters. The insert on the right side shows a magnification of the sensor fields.

3.6 Characterization of Sensor Chips

Optical Characterization

All pictures were recorded under visible light or under an excitation wavelength of 408 nm (blue laser) with following lenses: 5x, 10x, 20x, 50x and 100x.

Electrical Characterization

Electrical measurements were done on a Suess PA200 prober at room temperature. As parameter analyzer an Agilent 4155C was used. Therefore two-point measurements were made to characterize the sensor resistance and resistance distribution. Two needles were connected to the contact pads of every single sensing structure and a voltage in the range of from -0.1 V to +0.1 V was applied. Finally, the current was measured and the resistance was calculated using Ohm's law.

Raman Spectroscopy

For the dispensed GO layers, Raman spectra were recorded on a Thermo Scientific DXR Raman microscope with a 532 nm excitation laser (8 mW) and an exposure time of 0.2 s with 40 exposures. To investigate the homogeneity of the deposited GO layer, spectra were recorded every 10 µm over a total length of 500 µm.

FIB-Cut

The cuts were done on a Helios 600 from FEI. First, to get smother edges at the FIB-cut itself, all samples were sputtered with platinum (2 µm). Then the samples were bombarded with gallium ions at the centre of the sensor field across three gold fingers to create the cut. Finally, the SEM images were recorded at a voltage of 15 kV. Data evaluation was done with the Software "ImageJ".

All FIB-Cuts and the corresponding SEM images were done by Marion Römer in the Failure Analysis of Infineon Technologies AG Regensburg.

3.7 Gas Measurements

All gas measurements were made with a homemade gas measuring station. The station consists out of two mass flow controllers (Tylan 2900 Series from Mycrolis) to mix the gases to the desired concentration and 8 Agilent 3458A multimeters (one for each sensor field) to record the sensor response. The measurement temperature was controlled by a home-made FPGA-board which was able to control the sensor via the embedded heating structure of the sensor device. The MFCs, the FPGA-board and the multimeters are controlled by the computer. A schematic illustration of the gas station is shown in Figure 11. As carrier gas synthetic air (N_2: 80 %, O_2: 20 %) was used. Over the MFCs the desired NO_2 concentration 5 ppm, 10 ppm respectively 15 ppm was set. The overall flow rate was 500 sccm (Flowrate of synthetic air plus flowrate of NO_2). Measuring temperatures were 30 °C, 100 °C and 200 °C. Before every measurement, the sensor was heated up to 200°C for 60 s, to remove adsorbed humidity or gases from the environment. At the end of every gas measuring experiment, the sensor was heated again up to 200 °C for 60 s to recover the sensor and to remove still adsorbed NO_2 from the sensor surface.
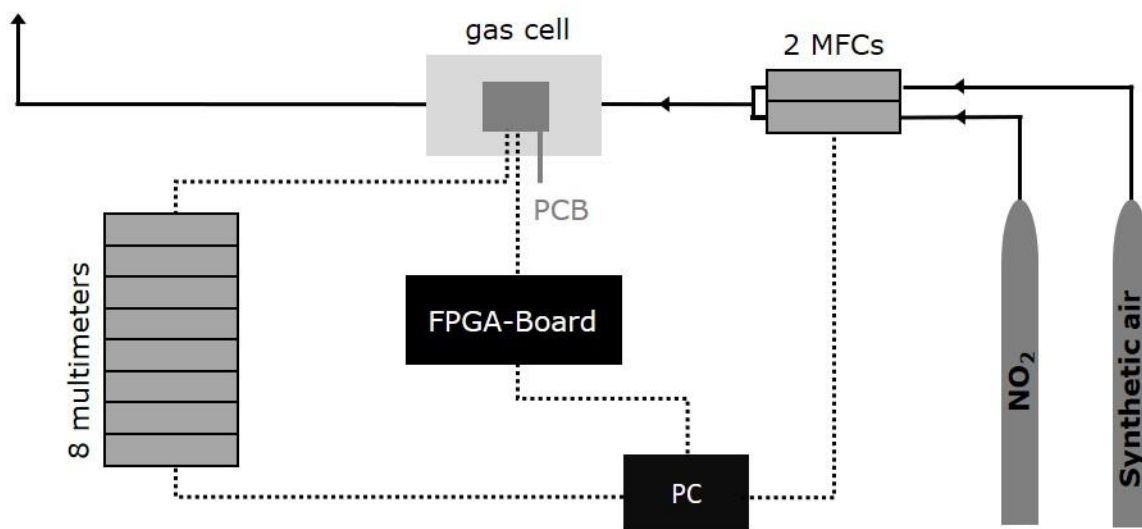

Figure 11. The schematic illustration of the homemade gas measuring station. Black lines show the gas part. Dashed lines show the communication between the different parts. With this setup it is possible, to control the heater temperature or the gas concentration (set by the MFCs) automatically by the PC.

4 Results & Discussion

4.1 Large-scale Graphene Oxide Synthesis and Purification

Due to the high surface-to-volume ratio [6], nanomaterials present outstanding properties which are completely different to their bulk materials [7] and are used for a high number of different applications, e.g., drug delivery [8], energy storage [9], catalysis [10], (nano-) electronics [11], or bio- and chemo sensing [12, 13]. This is also true for the class of 2D nanomaterials, which is characterized by a sheet-like structure. Here, the lateral size of the sheets ranges from several nanometres up to a few micrometres and even larger whereas the thickness of these sheets is only one or few atoms [6]. The most prominent representative of these class is graphene, a one-atom thick hexagonal carbon lattice and was firstly produced 2004 by Geim and Novoselov via scotch tape method [2]. Nowadays, further syntheses are known to fabricate graphene. These syntheses are categorized in top-down and bottom-up methods [14]. Top-down approaches starts with graphite. Here, the relatively weak interlayer forces will be separated into individual sheets down to mono- or few layers and graphene will be obtained, e.g., through mechanical or chemically exfoliation [15]. Bottom-up methods start with low molecular carbon sources as building blocks from which graphene is finally assembled, e.g., through chemical vapour deposition (CVD) or epitaxial growth on silicon carbide wafers [16]. The synthesis of choice is influenced by several aspects. First, the final application itself, since all mentioned syntheses produce different types of graphene which differ in flake size, defect density and number of layers [17]. This has to be taken into account, since these parameters drastically influence the outstanding properties of graphene like electrical conductivity, electrochemical activity or chemical inertness [18], [19]. Second, for industrial applications the scalability, the price and time factors are very important [20]. Therefore, the chosen synthesis must be up-scalable. Next to this, the transfer of graphene must not be neglected, since it can become very challenging and time consuming [21].

Due to its scalability, price, time and transfer factors, chemically exfoliated graphene fulfils all these parameters best. Graphene, which is synthesized by chemical exfoliation, is very often called GO, since strong oxidizing chemicals introduce oxygen containing defects, e.g., hydroxy-, epoxide-, carbonyl- or carboxyl- groups into the carbon lattice [22]. These defects have a huge influence on the dispersibility of GO in water, since they make the GO more hydrophilic and thus easily dispersible in water [23]. Since GO suspensions are stable in water, the so obtained graphene can be easily transferred onto the target substrate by dispensing or ink-jet printing [24].

Several techniques to synthesise GO are already described in literature. The most famous syntheses routes are Hummers method, Hofmann method and the Staudenmaier method [25]. All methods mainly differ on the types of chemical oxidants used to get an oxidation effect on the graphite starting material. Whereas Hummers method uses concentrated sulphuric acid, potassium permanganate and sodium nitrate to achieve the oxidation, the Hofmann method and the Staudenmaier method uses concentrated sulphuric acid, nitric acid and potassium chlorate [26, 27]. Due to this the advantages are clearly on the side of GO, prepared by Hummers method, because no toxic and explosive gases like ClO_2 or NO_x form during the synthesis, which leads to a less complex experimental apparatus and reduced safety regulations [28]. Figure 12 shows the advantages and disadvantages of Hummers, Hofmann and the Staudenmaier method.
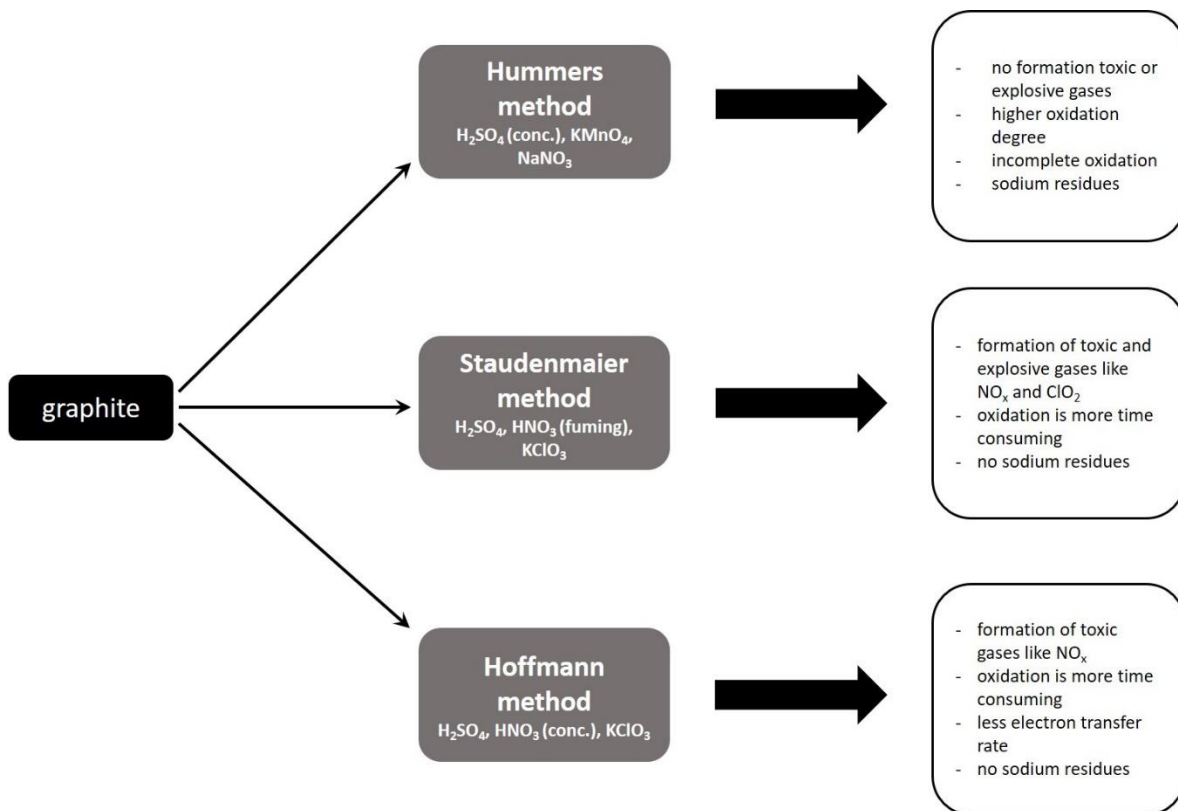
Figure 12. An illustration of different GO syntheses with their corresponding advantages and disadvantages and their oxidizing agents.

Nevertheless, challenging for all types of GO syntheses are the reduction of ionic contaminations which are depending on the applied synthesis and the agents used [25]. Especially, by using the Hummers method in the semiconductor industry, the sodium concentration after synthesis has to be reduced as far as possible, since sodium ions have a negative influence on the lifetime and reliability of semiconductor devices [29]. Therefore, it is necessary to introduce further purification steps which are able to reduce the sodium impurities down to the ppb range. Here, continuous methods like dialysis are more efficient and therefore, more promising than further centrifugation steps or a discontinuous dialysis in a beaker [30].

4.1.1 Purification of Graphene Oxide Synthesis

Typically, ionic contaminations of GO synthesised by using the Hummers method are sodium, manganese, and sulphur containing compounds like sulphate ions since $NaNO_3$, $KMnO_4$ and H_2SO_4 are used in the synthesis. Contaminations in the range of thousands of ppm are already reported in literature, e.g., 2290 ± 160 ppm manganese and 96 ± 7 ppm sodium [25] or up to 1-2% sulphur [31] directly after GO synthesis. Contaminations in such dimensions have to be avoided in the semiconductor industry especially such sodium impurities. Here, it is already known, that sodium is able to migrate into non-conducting layers and make them conductive which results in a decreased life time or in a device failure [29]. Deionized water, which is used in the semiconductor industry has a sodium content of smaller than 1 ppb [32]. Therefore, it is necessary that the sodium content of the GO suspension is as close as possible to the one of the deionized water. Although the production costs of semiconductor components often amount to only a few cents, a long service life is desirable, since these components cannot be easily replaced. Furthermore, the contaminants can be introduced into other semiconductor components or applications during the production which are relevant to the safety of the user, e.g., pressure sensors for car airbags. Next to sodium also sulphur contaminations have to be observed and minimized since it is known, that sulphur is able to poison the sensor layer [30] which will interfere with the final application. To reduce these ionic contaminations after GO synthesis, centrifugation, filtration, and dialysis are common techniques [30]. Here, a continuous diafiltration was introduced into the GO purification, where 2 L GO suspension were purified at the same time. Additionally, the efficiency of such continuous dialysis is much higher and the process itself is much faster compared to discontinue dialysis methods like conventional dialysis tubes in a beaker or centrifugation. To obtain information about the efficiency of the diafiltration process, every 2 L ICP-AES analyses of the permeate were done and are shown in Figure 13.
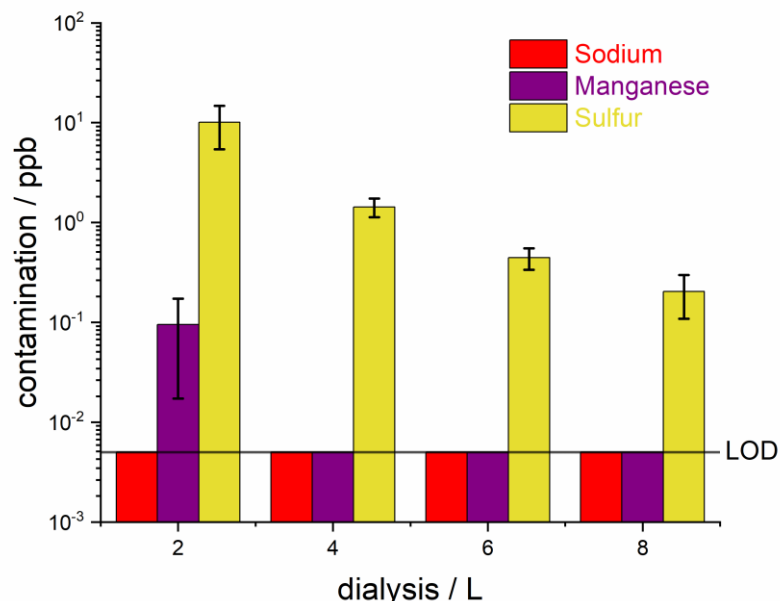
Figure 13. ICP-AES measurements of the permeate of the diafiltration after 2 L, 4 L, 6 L and 8 L. The black horizontal line indicates the LOD of the ICP-AES device at 0.005 mg/mL. Every column is averaged out of three dialysis (batches A1 - A3).

In the permeate after 2 L of dialyses only sulphur (around 10 ppm) and manganese (around 0.1 ppm) were detectable. All other elements like sodium were under the LOD of 0.005 ppm. Whereas no further manganese was detectable in the permeate after 4 L, sulphur (around 1.5 ppm) was still detectable. Further dialysis led to a further decreasing amount of sulphur. After 6 L of dialysis 0.44 ppm of sulphur, which correspond to 0.44 mg/L, were detected and after 8 L 0.22 ppm of sulphur (0.22 mg/L). Since continuous dialysis is very water consuming and only 0.2 mg/L sulphur were detectable in the permeate between 6 and 8 L the purification was stopped after 8 L. A faster and continuous measuring method would be conductivity measurements for example by using an electrode. Here, ionic impurities in the range of 5 µg/L to 250 µg/L can be determined, whereby this large range depends on the type of ion [33]. But this approach is not really feasible because the total ion content is displayed and not every single ion species can be broken down. Especially here, a resolution of the individual ions would be very interesting since the investigated impurities will be completely washed out at different times.

In order to make the different graphene suspensions better comparable for their characterization, the GO concentration of every batches was determined after

8 L of dialysis by gravimetric analysis. A determination of the GO concentration before the purification would be possible, but these concentrations may be defective due to the large number of contaminants. The results of the gravimetric analysis are shown in Table 2. The corresponding error analysis is shown with the example of GO Batch A1 in the appendix.

Table 2. Gravimetric analysis after 8 L of dialysis of all GO synthesis. For the batches A1 - A3 graphite as starting material was used which contains at least 99% carbon. Batches B1 - B3 are made out of graphite with a carbon content of at least 87%.

Batch	GO Concentration mg/mL	$\emptyset_{GO\ Concentration}$ mg/mL
A1	2.90 ± 0.06	
A2	2.41 ± 0.06	2.67 ± 0.25
A3	2.69 ± 0.06	
B1	2.98 ± 0.06	
B2	2.73 ± 0.06	2.72 ± 0.27
B3	2.45 ± 0.05	

All batches show concentrations in the range of 2.4 mg/mL to 3.0 mg/mL and are stable. In general, for too highly concentrated suspensions it has to be keept in mind that they favour agglomeration. Since two different graphite starting materials for the batches A1 - A3 respectively B1 - B3 were used, the concentrations between these were also compared. Here no differences between the starting materials can be seen. A reason could be, that the manufacturer of the graphite starting materials only declares such big differences in the carbon content due to quality standards (> 99% carbon content for the batches A1 - A3 and a carbon content > 87% for batches B1 - B3), but in fact, these two materials are almost identical. By comparing the average GO concentration of both graphite starting materials just very slight differences can be observed with an average GO concentration of around 2.7 ± 0.3 mg/mL.

To be able to make a detailed statement about the success of the dialysis the theoretical concentrations in ppm of sulphur, manganese and sodium after GO synthesis were calculated. Therefore, the weighted-in mass of sulphur, manganese, and sodium for the final volume of 2 L were calculated and are as follows: Sulphur 1.55×10^5 ppm, manganese 4.69×10^3 ppm, and sodium 6.09×10^2 ppm. In contrast to that, the final batches were diluted to a concentration of 0.5 mg/mL since this is in a concentration range where later the system integration of GO should take place. This sample were investigated by ICP-AES after complete dialysis (8 L) and are shown in Table 3.

Table 3. Contaminations of GO batches after final dialysis of 8 L at a GO concentration of 0.5 mg/mL.

Batch	Mn ppm	S ppm	Al ppm	Fe ppm
A1	0.060	4.000	0.027	0.018
A2	0.120	3.700	0.031	0.012
A3	0.160	4.400	0.035	0.030
B1	0.320	6.900	0.070	0.067
B2	0.120	3.600	0.130	0.028
B3	0.110	3.600	0.150	0.028
Ø$_{Batches}$	0.15 ± 0.09	4.4 ± 1.3	0.07 ± 0.05	0.03 ± 0.02

Sodium except for batch B1 (sodium content of 0.015 ppm) is generally under detection limit of ICP-AES of 0.005 ppm (corresponds to 0.005 mg/L). The contamination of aluminum, iron and manganese are in the range of around 0.1 ppm (corresponds to 0.1 mg/mL), and sulphur of around 5 ppm (corresponds to 5 mg/mL). Compared to the theoretical calculated values of sulphur 1.55×10^5 ppm, manganese 4.69×10^3 ppm, and sodium 6.09×10^2 ppm less than 0.1‰ of every ionic contamination is remaining in the final GO stock suspensions and more than 99.99% were removed. Furthermore,

the amount of sulphur removed in the last dialysis step (6-8 L) is just 0.2 ppm compared to around 5 ppm remaining in the GO stock suspension. Next to this also the time component for such dialyses is a factor for industrial applications. Purification by centrifugation is also not the ideal technique, since centrifugation is a discontinuous technique and the GO must be re-dispersed after each centrifugation step. Therefore, it is reasonable to stop the dialysis after 8 L. Comparing both graphite starting materials, no difference in terms of ionic contaminations can be observed after dialysis by using ICP-AES except that the iron content of B1 - B3 is slightly increased compared to A1 - A3. Furthermore, the fluctuations within the batches have the same order as the fluctuation between both graphite starting materials. This shows that the chosen starting graphite material has no influence on the ionic contamination of the GO suspensions. The kind of contaminations is in accordance with literature, but they are up to two orders of magnitude smaller due to successful dialysis [34], [35]. Furthermore, the results of ICP-AES show, that all impurities can be neglected for determination of the GO concentration via gravimetric analysis (Table 2) since all ionic impurities are in the very low ppm range.

Comparing the ionic impurities within the GO batches, no significant differences were observed, which means the purification of GO suspensions (Hummers method) was successfully performed. At a GO concentration of 0.5 mg/mL the detected impurities were around 4.4 mg/L for sulphur, around 0.15 mg/L for manganese, and around 7 µg/L for sodium. These concentrations indicate, that the developed purification procedure was successfully implemented whereby the ionic contaminations were reduced to a satisfactory level for manufacturing processes in the semiconductor industry.

4.1.2 Characterization of Graphene Oxide Batches

After the determination of the GO concentration and its impurities, a detailed material monitoring of the synthesised GO suspensions is necessary. Therefore, several techniques for a GO characterization are already described in literature [36], e.g., UV-Vis-, Raman spectroscopy, or XPS. Every method has its own strengths and weaknesses but also limitations. UV-Vis analysis is used for concentration determination and gives a first indication on the chemical composition of GO. The optical band gap of GO can be determined through a Tauc plot. Raman spectroscopy gives information about the oxidation degree, and therefore the number of defects can be determined by calculating the I_D/I_G-ratio. To get detailed information on the kind of defect (epoxide, carbonyl or carboxyl) XPS is the method of choice. Besides these techniques, NMR-relaxation time measurements were performed to characterize the GO suspensions, since here no sample preparation is necessary, and the samples are not affected by sample preparation.

To detect potential measurement errors of the gravimetric analysis in terms of GO concentration, UV-Vis spectra of all GO batches were recorded. Therefore, some points have to be taken into account for measuring GO suspensions by using UV-Vis spectroscopy. First, the ability to scatter incident light which decreases the transmittance and second the fact, that GO suspensions have a strong ability to absorb light with an absorption coefficient of 39.7 L g^{-1} cm^{-1} at a wavelength of 230 nm [37]. Since there is no molecular formula for graphene or GO and therefore no defined molar mass, the molar decadic absorption coefficient can't be calculated for graphene containing suspensions. Instead of that, the absorption coefficient of such suspensions must be expressed in the following unit: L g^{-1} cm^{-1}. To avoid the scattering and to reduce the high absorption, GO suspension was diluted, since then the scattering and the absorption is reduced. Next to the GO concentration also information about the composition of GO can be obtained because besides the peak maximum at around 230 nm ($\pi \rightarrow \pi^*$: transition of sp^2-domains) also a shoulder appears at a wavelength of around 300 nm which indicates the n $\rightarrow \pi^*$ transition of carbonyl

groups [38]. The recorded UV-Vis spectra of all GO batches show slight differences in intensity and are shown Figure 14 (A). Every UV-Vis spectrum consists of three single spectra. The coloured shadow represents the standard deviation of every GO batch.
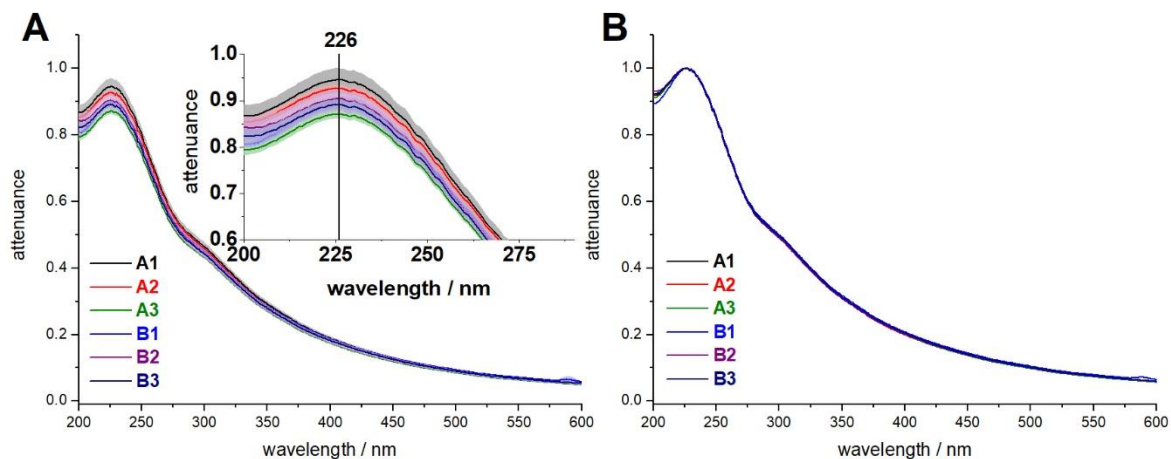

Figure 14. UV-Vis spectra of Graphene batches at GO concentration of 0.025 mg/mL. The colored lines indicate the average spectrum of three single measurements with the corresponding standard deviation (colored shadows). **(B)** Normalized spectra (at λ_{Max} = 226 nm) of all GO batches.

For the final validation of GO concentration, the averaged absorbance ($A_{overall}$) at 226 nm (18 spectra: six batches a three measurements) was determined, and the averaged absorbance coefficient of GO ($\alpha_{Overall}$ = 36.3 ± 1.1 L g^{-1} cm^{-1}) was calculated by the Beer-Lambert law. Finally, the concentration (c_{UV-Vis}) of every single GO batch was calculated by the averaged absorption coefficient ($\alpha_{overall}$) and the averaged absorbance ($A_{GO\ batch}$) of every single batch. The obtained concentrations (c_{UV-Vis}) and the deviation compared to gravimetric analysis ($c_{gravimetric\ analysis}$) are shown in Table 4.

Table 4. Comparison and deviation between gravimetric analysis and UV-Vis spectroscopy of GO batches.

Batch	$C_{Gravimetric\ Analysis}$ mg/mL	$C_{UV\text{-}Vis}$ mg/mL	Δc mg/mL	Δc %
A1	2.90 ± 0.06	3.02 ± 0.08	0.12	4.14
A2	2.41 ± 0.06	2.46 ± 0.03	0.05	2.07
A3	2.69 ± 0.06	2.58 ± 0.03	0.11	4.09
B1	2.98 ± 0.06	2.96 ± 0.03	0.02	0.67
B2	2.73 ± 0.06	2.72 ± 0.06	0.01	0.37
B3	2.45 ± 0.06	2.41 ± 0.03	0.04	1.63

Despite the slight absorbance differences in the UV-Vis spectra, it can be concluded, that the GO concentration of every batch was calculated correctly by gravimetric analysis. The corresponding normalized spectra (at λ_{max} = 226 nm) of all materials (Figure 14 (B)) show, that the ratios between λ_{226} and λ_{300} are identical. This is a first hint, that all GO batches have the same oxidation state, due to the fact, that no differences in terms of n → π* transition can be observed and are as previously reported [39, 40]. Next to the concentration and the chemical composition in terms of carbonyl functionalities, the UV-Vis spectra contain even more information, e.g., the band gap which is defined as the energetic distance between valence band and conduction band. Here, a photon needs an energy which is equal or greater than the band gap of the investigated material, that it can be absorbed by the material and an electron gets excited from the valence band into the conduction band. Whereas ideal graphene has a band gap of zero [41], GO is characterized by a band gap in the range from several electron volts up to non-conductive behavior (> 4.0 eV), which is caused by the oxygen functionalization [42] and correlates with the number of oxygen atoms in the carbon lattice [43]. Based on the absorption data, the optical band gap of GO can be estimated from Tauc plots [44]. Here, the wavelength of the absorption spectra is converted into the energy (eV) and represents the x-axis

of the Tauc plot. The y-axis is obtained when the energy (E in eV) will be multiplied with the absorption A of GO and the corresponding absorption coefficient α and finally squared with itself. The same absorption coefficient (36.3 L g^{-1} cm^{-1}) was taken as for the determination of GO concentration above. After transformation, a linear fit in the range of 4.75 eV to 5.25 eV (grey area) was generated and extended to the x-axis. The point of intersection between x-axis and linear fit represents the band gap of the investigated material in electron volt. In Figure 15 (A) the UV-Vis spectra before transformation are given and in Figure 15 (B) the corresponding Tauc plots of GO batch A1 with their determined band gap of 4.33 eV are shown.
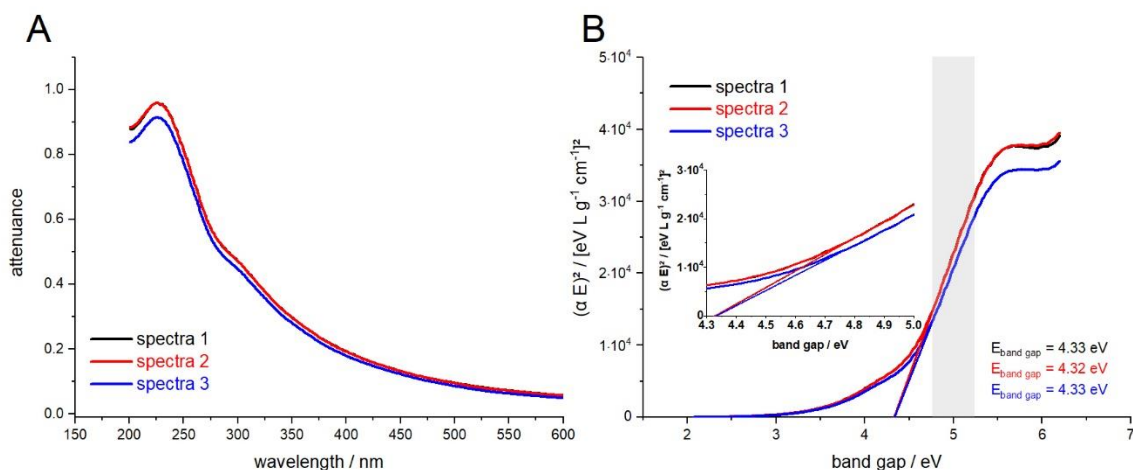

Figure 15. (A) Absorption spectra of GO batch A1. **(B)** Corresponding Tauc plots of GO batch A1 for the determination of the band gap. For the x-axis, the wavelength is transferred into electron volts. For the y-axis, the absorbance multiplied with the absorption coefficient (α) and the binding energy and squared by itself. Finally, a linear fit is generated (grey area: from 4.75 eV to 5.25 eV) and the obtained linear fit is extended to the x-axis. The point of intersection (x-axis and linear fit) corresponds to the band gap.

In the same way, the band gaps of all other GO batches were determined, are shown in Table 5 and are as previously reported [45]. Comparing the band gaps, all batches show non-conductive behavior (> 4.0 eV) with a band gap of 4.32 eV - 4.33 eV. Furthermore, no differences between the batches can be observed. Even more, the calculated standard deviation of 0.01 eV is very small. This leads to the conclusion, that the number of oxygen atoms within the carbon lattice and therefore the oxidation degree between the GO batches is the same. Also, the graphite starting material used has no influence on the band gap of the synthesized GO.

Table 5. The optical band gaps (E_g) of all GO batches. Determined by transferring the UV-Vis spectra into Tauc plots.

Batch	Band Gap (E_g) eV	$\emptyset$ Band Gap (E_g) eV
A1	4.33 ± 0.01	
A2	4.32 ± 0.01	4.32 ± 0.01
A3	4.32 ± 0.01	
B1	4.32 ± 0.01	
B2	4.33 ± 0.00	4.32 ± 0.01
B3	4.32 ± 0.01	

To get deeper understanding into the structure of GO, Raman spectra of all GO batches were recorded. During the synthesis of graphene or graphene related materials like GO, structural changes take place which can be investigated by Raman spectroscopy. The Raman spectrum of graphene exhibits two very prominent peaks. The first peak is named as the G-peak at around 1580 cm^{-1} and is attributed to the stretching of the C-C bond in sp^2-hybridized carbon materials [38, 46]. The second peak, the so-called 2D-peak at around 2690 cm^1 causes due to the double resonant Raman scattering with two-phonon emissions. For single layer graphene single symmetric peak with a FWHM of around 30 cm^{-1} is observed. By adding one layer after the other, the FWHM of the 2D-peak increases and splits into several overlapping peaks [46]. This splitting takes place, since the symmetry of graphene is lowered when the number of layers is increased. The FWHM values of the 2D-peak for GO ranges from 144 cm^{-1} to over 200 cm^{-1} [47, 48]. When defects interrupt the honeycomb carbon lattice of graphene, e.g., in the case of GO, a further peak appears in the Raman spectrum. The so-called D-peak at around a 1350 cm^{-1} which is attributed to the increased disorder in the sp^2-hybridized graphene lattice and correlates with the number of defects [49]. Due to this, the I_D/I_G-ratio is an indicator for the number of defects and therefore for the oxidation degree of

GO [50]. The averaged Raman spectra with their corresponding I_D/I_G-ratios of all GO batches are shown in Figure 16.
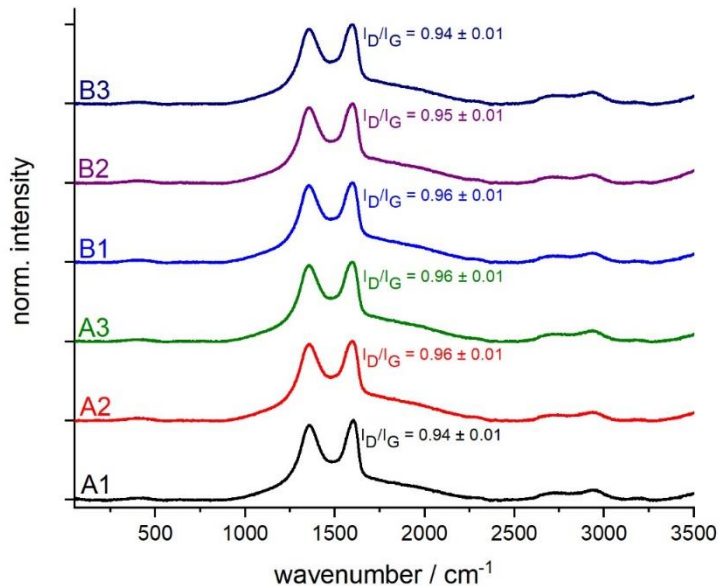

Figure 16. Normalized Raman spectra of all GO batches and their calculated I_D/I_G-ratio. Every spectrum displays the averaged line scan over a distance of 500 µm. Therefore, Raman spectra – were recorded every 25 µm, each containing 40 exposures.

The Raman spectra of all batches show the prominent peaks at 1355 cm^{-1} (D-peak), at 1590 cm^{-1} (G-peak) and around 2715 cm^{-1} (2D-peak) and are as previously reported [51]. Also, the averaged FWHM of the 2D-peak is around 180 cm^{-1} and fits very well to the literature. Furthermore, the determined I_D/I_G-ratios are very similar and in the range between 0.94 and 0.96. This indicates, that all batches have the same number of defects within the graphene carbon lattice and therefore the same oxidation degree, which is a further indication, that the chemical composition of all GO batches are identically. In addition to that, investigations into the statistically Raman spectroscopy were made. Therefore, 25 Raman spectra where each spectrum consists out of 40 exposures were recorded for every GO batch, the I_D/I_G-ratios were determined and statistically evaluated. These ratios are shown as Box plot diagram in Figure 17.
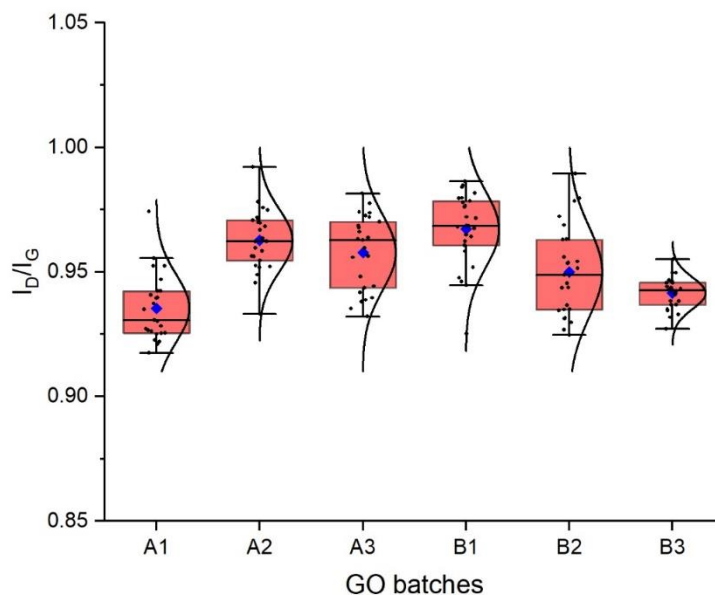
Figure 17. I_D/I_G-ratios of all GO batches (25 spectra per batch) plotted as Box plot. The blue point represents the average I_D/I_G-ratio of every batch. The red box shows the range, where 50% of the I_D/I_G-ratios are present. The black antennas exhibit the other 50% of the determined ratios, whereas 25% of all ratios are above the red box and 25% are below. The black horizontal line within the red box shows the median of all ratios.

Comparing the average, respectively the median values of all GO batches slight differences of around 0.01 can be observed. Next to this, the antennas which indicates the highest and lowest 25% of the ratios show, that the distributions within the samples are larger (around 0.03) than differences of the averages of all batches. On the one hand, this suggests, that the number of defects and therefore, the oxidation degree within the GO batches are the same. On the other hand, Raman spectroscopy reaches its limitations in terms of lateral resolution and is not able to resolve the defects in the carbon lattice accurately. Also, the large error bars are not advantageous for a good comparison between the GO batches.

Next to this, the FWHM of the 2D-peaks correlates with the number of graphene layers. Therefore, the FWHM of every Raman spectrum was determined. The obtained averaged values with their deviation are shown in Table 6. Moreover, by using the I_D/I_G-ratio the distance (L_D) between two defects can be calculated with the following equation (eq. 1) from *Cancado et al.* [52].

$$L_D = \sqrt{\frac{4.3 \times 10^3}{E_L^4} \left(\frac{I_D}{I_G}\right)^{-1}} \qquad\qquad eq.\ 1$$

where E_L is the laser energy (here 2.33 eV which corresponds to 532 nm).

The calculated defect to defect distances of the GO batches are shown in Table 6.

Table 6. Determined FWHM$_{2D}$ of GO batches and the calculated defect to defect distance of GO batches according to Cancado.

Batch	FWHM$_{2D}$ cm^{-1}	L$_D$ nm
A1	178.6 ± 10.5	12.48 ± 0.09
A2	182.0 ± 7.0	12.31 ± 0.08
A3	190.2 ± 4.3	12.34 ± 0.10
B1	184.5 ± 8.2	12.28 ± 0.09
B2	189.4 ± 8.3	12.39 ± 0.12
B3	191.8 ± 3.8	12.44 ± 0.04
Ø$_{Batches}$	**186.1 ± 5.2**	**12.38 ± 0.08**

The FWHMs of all GO batches are very similar around 186 cm^{-1} and in a range as already reported [47, 48]. The calculated distance between two defects are also very similar and no differences between the GO batches exists. The calculated distance indicates that the honeycomb lattice is largely intact [53]. Also, these two parameters allow the conclusion, that all the synthesized GO batches are identical in terms of number of defects and number of layers.

To investigate the defects of GO not only in terms of presence and number of defects but also in terms of kind of defects, XPS measurements were done. Here, due to small shift (few eV) in the binding energy, conclusions about the binding partners and the kind of defects can be drawn. By performing XPS measurements, always a survey spectrum is recorded. Due to this, also

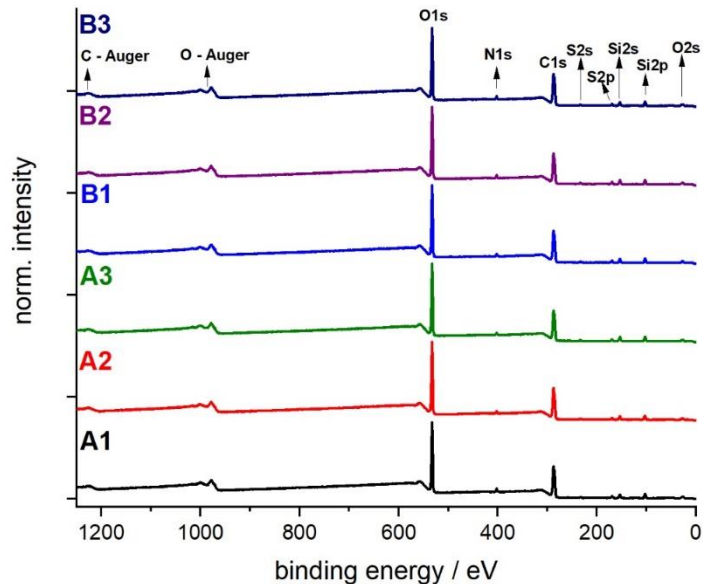contaminations can be detected in parallel. These XPS survey spectra are shown in Figure 18.

Figure 18. The normalized XPS survey spectra of all GO batches. Main components are carbon (C1s-peak at 286 eV) and oxygen (O1s-peak at 532 eV) with slight impurities of nitrogen, sulphur, and silicon.

Next to the expected C1s- and O1s-peak also nitrogen (N1s at 400 eV), sulphur (S2s at 232 eV and S2p at 169 eV), and silicon (Si2s at 154 eV and Si2p at 103 eV) could be found. These mentioned impurities have a completely different origin. The sulphur, which was already detected by ICP-AES comes from the large amount of sulphuric acid, which is used in the Hummers method. Since silicon was under the LOD of ICP-AES, it can be concluded, that the N1s, the Si2s and Si2p peaks result from Si_3N_4 containing substrate.

To obtain deeper information like the kind of defects, detailed C1s and O1s spectra of all batches were recorded. First, the background was rectified by a so called "shirley correction" [54]. Then the different peaks (for every binding type on peak) were fitted into the C1s respectively O1s spectra until the fit is in agreement with the corresponding recorded XPS spectrum. These recorded spectra of all GO batches are shown in Figure 19 (A) respectively in Figure 19 (B).
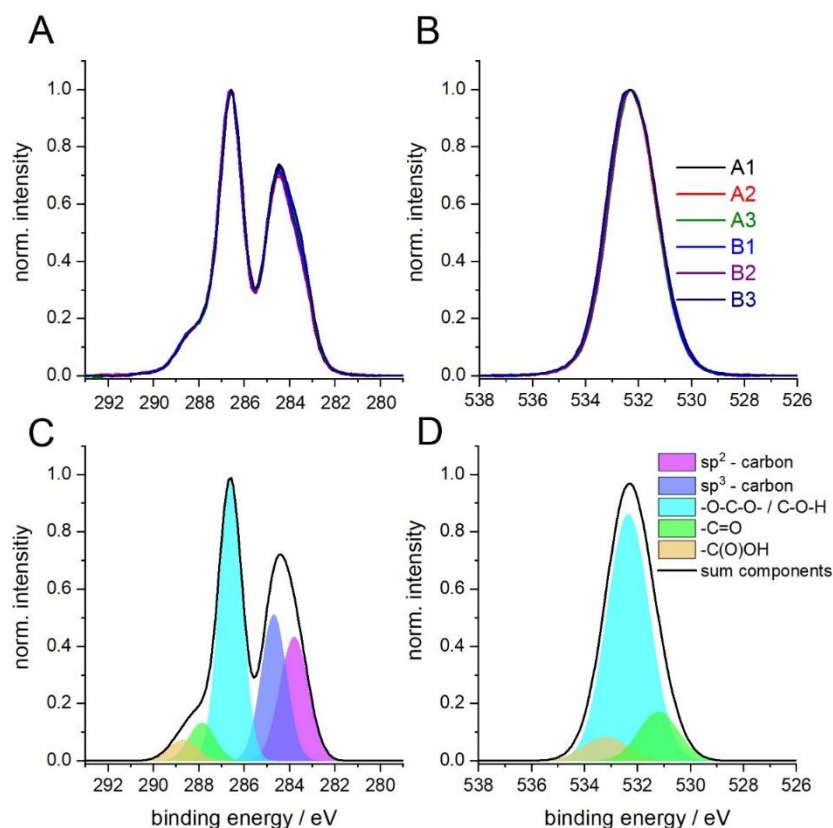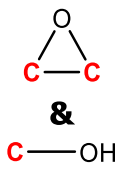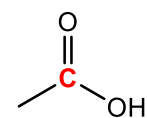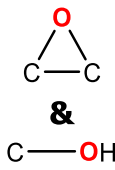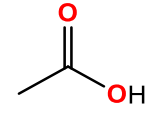
Figure 19. (A) XPS C1s-peak of all batches with corresponding O1s-peak **(B)**. **(C)** individually fitted components of C1s-peak corresponding to **(A)**. **(D)** individually fitted components of O1s-peak corresponding to **(B)**.

The XPS C1s spectra of all GO batches, show the presence of a sp^2- and sp^3-hybridized carbon at 283.8 eV respectively 284.7 eV within the GO lattice. In all C1s spectra the common GO defects like -O-C-O- and -C-OH, which are assigned to epoxide- and alcohol-groups at286.6 eV, -C=O, which are associated to ketones, quinones and aldehydes at 287.9 eV and -C(O)O-, which corresponds to esters- and carboxyl-groups at 288.6 eV are present (Figure 19 (C)). The O1s-spectra confirm the attendance of -C-O-C- respectively -C-OH at 531.2 eV, -C=O groups at 532.3 eV and -C(O)O- groups at 533.2 eV (Figure 19 (D)). All groups are as previously reported [55].

Next to the qualitative determination, qualitative quantification can be done by XPS. There a few aspects must be taken into account. First, how the sample was excited; by a Mg_α- or an Al_α-X-ray radiation. Secondly, the cross-section and the sensitivity factors have to be taken into account, since these are depending on the investigated elements [56]. All these empirical parameters and factors can
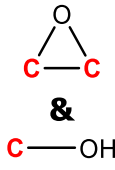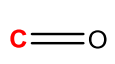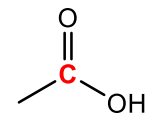
be entered into the software, or are considered by the software itself. For the correction, the peaks areas of the different groups get corrected and normalized by multiplying with these cross-section and sensitivity factors. Finally, the so-obtained corrected peak areas will be compared with the sum of all groups of the C1s and the O1s detail spectra. Finally, the software (Unifit 2012) quantifies the different components, like epoxide, carbonyl, carboxyl, sp^2-, or sp^3-hybridized carbon based on the C1s and O1s detail spectra by using the normalized peak areas. Due to this, a credible data evaluation can be obtained. The qualitative quantification of the synthesized GO batches is given in Table 7.
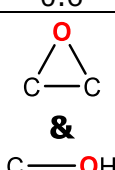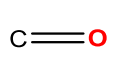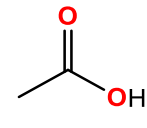
Table 7. The detailed quantification of the individual components of the XPS C1s and XPS O1s spectra of all batches. All calculations were done by using the XPS evaluation software "Unifit 2012". Measurements recorded in February 2020 at TH Deggendorf in Taisnach.

C1s spectra	sp^2	sp^3	epoxide & C—OH	C=O	carboxyl C—OH
	%	%	%	%	%
A1	15.7	16.3	28.3	4.5	2.7
A2	14.8	15.6	29.2	3.8	2.9
A3	15.2	16.0	28.2	4.1	2.5
B1	15.2	15.9	28.9	4.3	2.5
B2	14.8	15.0	29.0	4.2	2.3
B3	15.8	15.7	27.5	5.2	2.4
Ø Batches	**15.3 ± 0.4**	**15.7 ± 0.5**	**28.5 ± 0.6**	**4.3 ± 0.5**	**2.5 ± 0.2**
O1s spectra			epoxide & C—OH	C=O	carboxyl C—OH
			%	%	%
A1			25.3	4.7	2.6
A2			25.0	5.7	3.0
A3			25.4	5.5	3.0
B1			25.9	4.9	2.4
B2			26.6	5.2	2.9
B3			25.9	5.1	2.4
Ø Batches			**25.7 ± 0.6**	**5.2 ± 0.4**	**2.7 ± 0.3**

By comparing the sp^2- and sp^3-hybdrized carbon content just slight difference between the GO batches can be observed, whereas the ratio between sp^2- and sp^3-hybridized carbon is around 1. Furthermore, for all batches the number and kind of defects are very similar. The most present kind of defect is the epoxide-respectively the alcohol-group with 28.5%, followed by carbonyl-groups with 4.3% and carboxyl-groups with 2.5%. Since the formation of any carboxyl- or ester-group requires the breaking of C-C bonds, which may result in an overoxidation and CO_2 formation, the relatively low presence of these defects is therefore reasonable [57]. Even more, carbon content of 66.7% ± 0.7% and oxygen content of 33.6% ± 0.7% are totally constant for all GO batches. The differences in quantification between C1s and O1s spectra are due to the fact that the LOD is around 0.1 - 1.0% [58, 59]. Furthermore, the quantification by using the O1s spectrum is not as accurate as quantification by using the C1s spectrum due to the shape of the O1s peak. All XPS results in terms of binding energy, number and kind of defects as well the carbon to oxygen ratio is as previously reported [60, 61]. Also, the fact, that only around 15% of the carbon atoms are sp^2-hybridized and therefore able to conduct electrical current, shows that the band gap of 4.3 eV (non-conductive behaviour) determined by UV-Vis spectroscopy is consistent. Based on the successful qualification and quantification of oxygen containing defects by XPS (Table 7), these measurements were compared with 4 years old XPS measurements. The measurements recorded in 2016 were done at a different XPS device compared to the XPS measurements recorded in 2020. The comparison of the average's values of all GO batches are shown in Table 8.

Table 8. Comparison of XPS measurements after 4 years. All calculations were done by using the XPS evaluation software "Unifit 2012. Measurements recorded in 2016 were performed at Osram Opto Semiconductors GmbH Regensburg. Measurements recorded in 2020 were made at TH Deggendorf in Taisnach.

C1s spectra	sp^2	sp^3	C—C (epoxide, O bridge) & C—OH	C=O	C(=O)OH (carboxyl)
	%	%	%	%	%
2020	15.3 ± 0.4	15.7 ± 0.5	28.5 ± 0.6	4.3 ± 0.5	2.5 ± 0.2
2016	10.2 ± 1.1	17.5 ± 1.3	30.4 ± 0.6	5.7 ± 0.3	2.0 ± 0.2

O1s spectra	C—C (epoxide, O bridge) & C—OH	C=O	C(=O)OH (carboxyl)
	%	%	%
2020	25.7 ± 0.6	5.2 ± 0.4	2.7 ± 0.3
2016	26.2 ± 0.9	4.2 ± 1.0	3.7 ± 0.7

Both XPS measurements fit very well to each other. Especially by taking into account that the XPS measurements were done at different XPS devices. Regarding credibility and reliability, the XPS spectra recorded in 2020 are more preferable, because these spectra were recorded in a more detailed way. Furthermore, these measurements demonstrate, that no material degradation takes place.

Since all characterization used techniques based on optical methods, whereby the GO suspension has to be strongly diluted, e.g., UV-Vis spectroscopy or the GO suspension has to be transferred on substrates, e.g., Raman and XPS spectroscopy, which change the chemical environment drastically, NMR–relaxation time measurements for further characterization were done. The big advantages of NMR-relaxation time are, that neither any dilution nor any sample preparation is needed [5]. The only necessary step is to transfer the GO

suspension into an NMR-tube. For NMR-relaxation time measurements it has to be remembered, that not complete structures – as usual in the organic chemistry – are investigated. Here, the interface between dispersed nanomaterial surface and dispersing agent is studied in a relation to other samples. The finally measured NMR-relaxation time depends on the fact, if the solvent molecules are attached to the nanomaterial (surface molecules) or free in suspension (bulk molecules) [62]. A schematic illustration of a graphene containing suspension with both molecule types is shown in Figure 20.
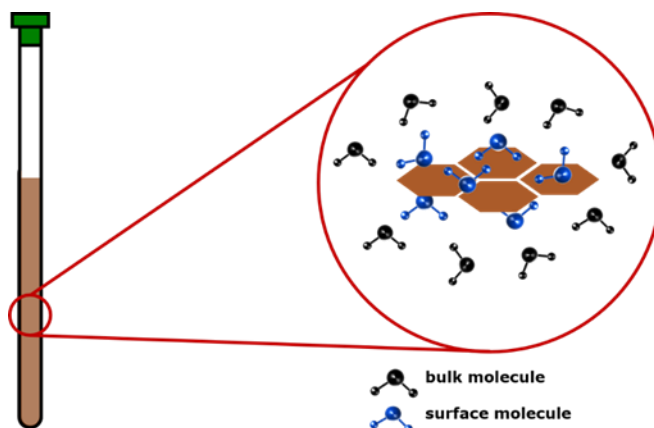

Figure 20. An illustration of a GO suspension in an NMR tube with both kinds of liquid molecules. The blue surface molecules are characterized by the attachment to GO flakes whereas the black bulk molecules are free in the suspension and do not wet the GO flake surface.

The "surface molecules" describe the molecules which are wetting the suspended nanomaterial. The "bulk liquid" refers to the molecules which have no direct contact to the nanomaterial. Both liquids differ significantly in relaxation times since molecular motion is slower compared to the bulk liquid at the solid-liquid interface [63]. This motion corelates with a zone of reduced diffusion, which is equivalent to a zone of increased viscosity close to the interface [64]. In this zone of increased viscosity, the relaxation time is shorter than in the bulk liquid and aligned protons can easier relay their energy to their surroundings [64]. The size of this zone with greater viscosity is influenced by the concentration of the dispersed nanomaterial [5], the flake size respectively the flake size distribution of the nanomaterial [65] and the wettability, the ability of the dispersing agent to wet the nanomaterial surface [66].

Summarized, the measured NMR relaxation time of suspensions is an average of "liquid molecules" and "surface molecules". An increased number of surface molecules lead to shorter average relaxation time as seen in equation 2 [67].

$$R_{av} = \psi_p SL\varphi_b (R_s - R_b) + R_b \qquad\qquad eq.\ 2$$

where R_{av} is the average relaxation rate, ψ_p is the particle volume to liquid volume ratio, S is the total surface area per unit particle density, R_s is the relaxation rate for "surface molecules" weight, L is the surface layer thickness of liquid, φ_b is the bulk particle density; and R_b is the relaxation rate of "bulk molecules". Hereby, the relaxation rate is the reciprocal value of the relaxation time.

Figure 21 (A) shows the results of NMR-relaxation time measurements at different GO concentrations and Figure 21 (B) the NMR-relaxation times of all GO suspensions at constant concentration of 2 mg/mL. All GO batches show a linear behaviour between GO concentration and NMR-relaxation rate, but also a large distribution within the slope among each other can be observed.
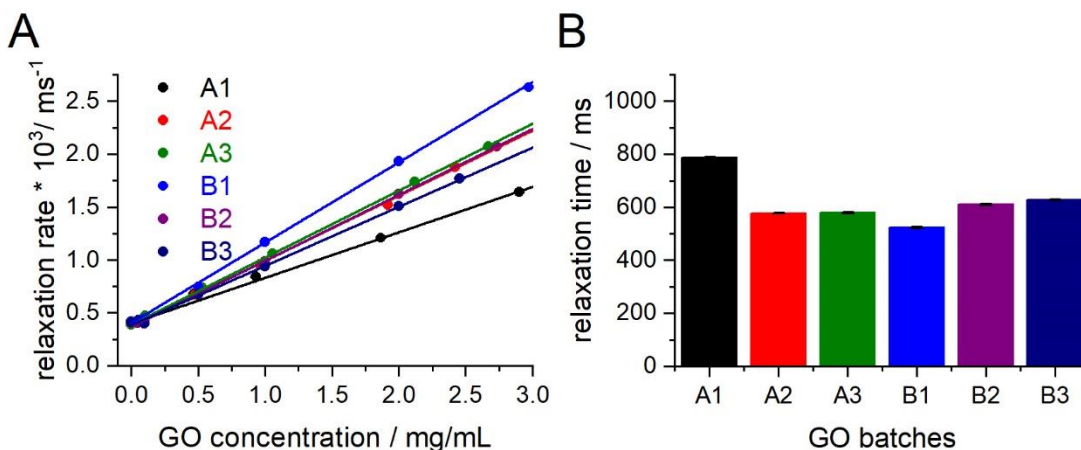
Figure 21. (A) The different GO batches at different concentrations plotted vs. NMR-relaxation rate. **(B)** Relaxation time of the different GO batches at a concentration of 2 mg/mL.

A first impression could be, that the determination of the concentration of the GO batches is erroneous, but therefore UV-Vis spectroscopy and gravimetric analysis are in a too good accordance to each other. Also, possible differences in terms of the chemical composition or oxidation degree, which leads to different hydrophily and therefore different wettability between the GO flakes and the dispersing agent, can be excluded, since XPS, UV-Vis-, and Raman

spectroscopy don't determine any differences like this between the GO batches. As consequence of this, the GO batches have the same chemical composition but different flake size distributions and therefore a different total surface amount which leads to the distribution in NMR-relaxation. These differences in GO flake size distribution were not to be expected since such a GO suspension consist of a large ensemble of GO flakes which is based on a normal distributed GO flake size distribution. A possible reason for the large distribution of the GO concentration (ranging from 2.4 mg/mL up to 3.0 mg/mL) as well as the GO flake size distribution could be the manually decanting during the centrifugation steps of the GO purification. While the most GO flakes are completely collected on the bottom of the centrifuge tube, a certain amount of the smallest flakes remain in the supernatant and will be subsequently removed by manually decanting.

To sum it up, all six GO batches were characterized in terms of concentration, number and kind of defects by UV-Vis, Raman spectroscopy and XPS. Moreover, a first impression on the GO flake size was received by NMR-relaxation time whereby further investigations are necessary. All the different characterization techniques used have advantages and disadvantages respectively limitations for the process control of GO. By using the same synthesis protocol for future syntheses, the concentration of GO can be determined only by UV-Vis spectroscopy since the time consumption is strongly reduced compared to gravimetric analysis. Next to the reduced time consumption of UV-Vis spectroscopy first impressions on the chemical structure can be easily generated by Tauc plots. For deeper characterization mainly in terms of number and kind of defects, XPS should be preferred over Raman spectroscopy, since the obtained findings are more profound, although the data generation and evaluation of XPS is more time consuming and complex than for Raman spectroscopy. Equally conceivable would be, that the synthesized GO batches will be characterized after UV-Vis spectroscopy by NMR-relaxation time. Therefore, a lower and upper limit has to be defined. If the GO batch is between the two defined limits, the batch can be used for further processing otherwise a detailed characterization by XPS is necessary. However, it might be necessary to compare a larger number of GO batches.

4.1.3 Characterization of sonicated Graphene Oxide Suspensions

GO suspensions prepared by chemical exfoliation contain a large ensemble of flakes with a distribution from several micrometres down to a few nanometres in size [68]. To investigate the size respectively size distribution of such suspension several techniques are already described in the literature [6], such as LM, SEM, TEM, or AFM. Unfortunately, the method of choice depends on the lateral size of the investigated graphene flakes. The throughput as well the sample preparation for the flake size characterization should not be underestimated and can represent a significant time aspect. Furthermore, the sample preparation of all these techniques needs a transfer, where the sample can no longer be in suspension and the flakes must be dried on the substrate, which changes the chemical environment of the graphene flakes drastically. Even more, flake overlapping, or flake wrinkles make a flake size determination by using these microscopic techniques impossible. Due to these limitiations, the characterization of large GO ensembles isn't straight forward and NMR-relaxation time could be a good alternative method to characterize the surface area of such large GO ensembles. To apply NMR-relaxation time and to characterize the dependency of the GO flake size, it is necessary to separate small flakes from the larger ones or to reduce the average flake size and compare it with flakes that are not reduced in size. Some techniques are already described in literature to separate flakes with different sizes like centrifugation [69] or to reduce the flake size with liquid cascade [70]. But as already described in the chapter above, NMR-relaxation time depends not only on the total surface area and chemical composition but also on the GO concentration. Since centrifugation and liquid cascade generates GO suspensions with different GO concentrations, additional weight determinations of each GO suspension would be necessary. To eliminate this problem, a method must be chosen whereby the GO concentration stays constant and the average flake size gets reduced. Both aspects will be fulfilled by an ultrasonic treatment of GO suspension by a sonotrode [71]. To investigate the influence on the graphene flake size, GO

batch A1 was chosen and sonicated for 1 min, 5 min, 10 min respectively 20 min by a strong sonication treatment (70 W). In Figure 22 the results of NMR-relaxation time measurements after different sonication times are shown.
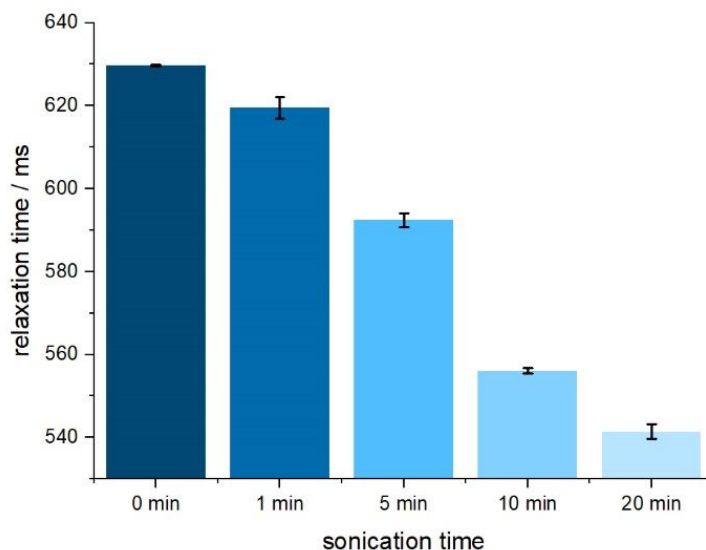
Figure 22. T2 - NMR-relaxation time of GO batch A1 at 2.9 mg/mL after different sonication times of 0 min, 1 min, 5 min, 10 min, 20 min. Sonication decreases the NMR-relaxation time as well the average flake size which is correlating to smaller GO flakes.

It can be clearly seen that a longer sonication time leads to a decreased NMR-relaxation time. This is corresponding to an increased ratio of surface to bulk molecules in the suspension and therefore to a smaller average flake size [72]. Via ultrasonic treatment the NMR-relaxation time is decreased from 630 ms (non-sonicated) down to 540 ms for 20 min sonication and fits very well to the theory of NMR-relaxation time [5]. To confirm these results and to get an overview on the magnitude of the GO flake size reduction by sonication SEM images were recorded and are shown in Figure 23.

Figure 23. SEM images of GO flakes at a GO concentration of 0.002 mg/mL on Si_3N_4 coated silicon wafer after different sonication times: **(A)** without sonication, **(B)** after 1 min, **(C)** after 5 min and **(D)** after 10 minutes of sonication.

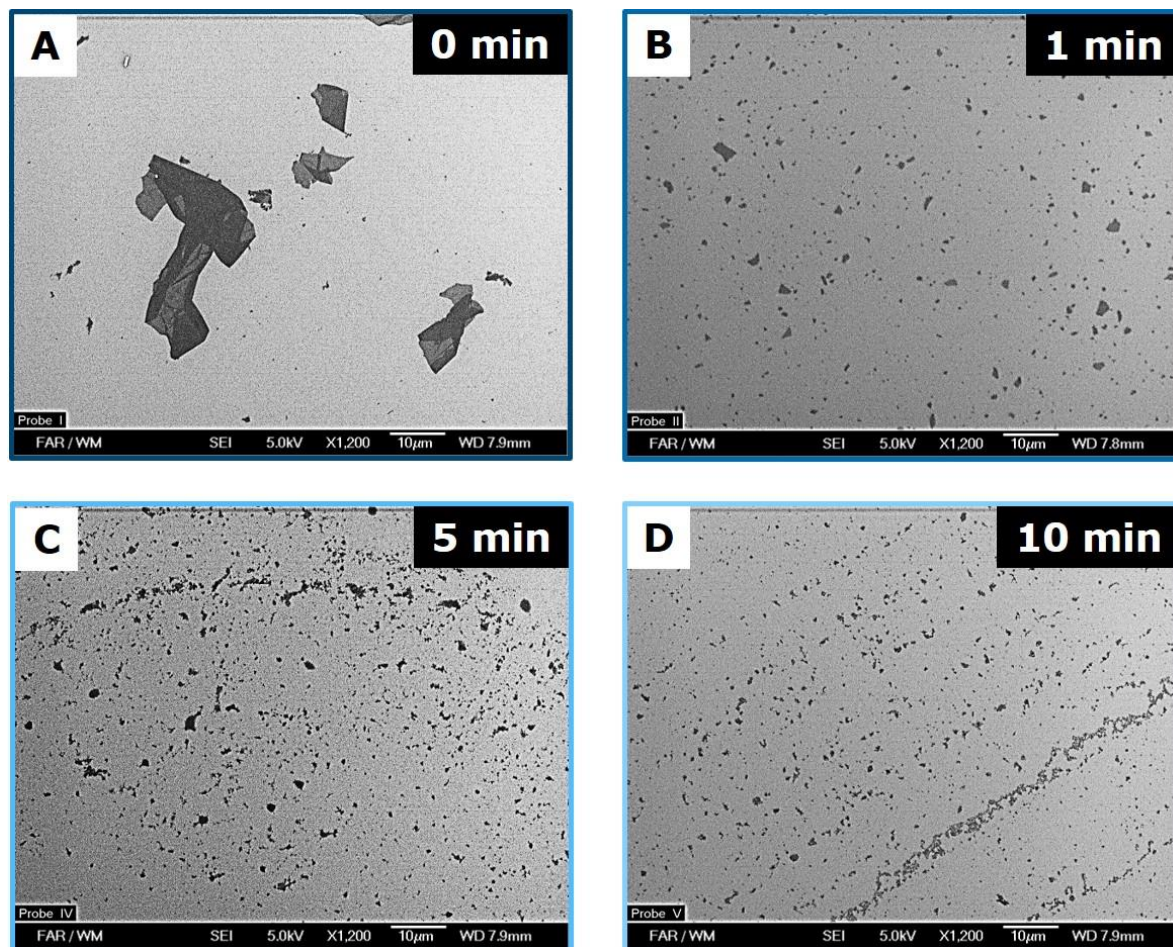Here, it is clearly visible, that ultrasonic treatment leads to decreased GO flake sizes. The non-sonicated GO flakes in Figure 23 (A) show a Feret diameters [73] up to 20 µm. Already after 1 min of sonication (Figure 23 (B)) the GO flake size is reduced to an Feret diameter of around 3 - 5 µm. After 5 min (Figure 23 (C)) respectively 10 min (Figure 23 (D)) only a few flakes with a Feret diameter larger than 3 µm can be seen. Here, most of the GO flakes are smaller than 2 µm. As already described above, GO flake folding is a big issue for a credible GO flake size determination. Whereas this folding can only be observed at large GO flakes, small GO flakes prefer the coffee-ring formation. Despite the high dilution (0.002 mg/mL) a slight coffee-ring formation can be seen in Figure 23 (C) and (D). Coffee-ring formation takes place, when suspensions are dried and the GO flakes, driven by a capillary flow due to the different evaporation rates across the deposited droplet, move to the droplet edges [74]. All these factors show,

that a credible and reliable flake size determination of such GO suspensions is not straight forward by using SEM or other microscopic techniques. Nevertheless, SEM confirms NMR-relaxation time measurements, where ultrasonic treatment reduces the average GO flake size. Furthermore, SEM shows, that NMR-relaxation time is able to investigate suspensions in terms of surface area containing a large ensemble with a broad flake size distribution.

A further method to characterize suspensions in terms of particle respectively flake size is DLS [75]. Here, the changes in the scattering intensity, which depends on the particle size (Brownian motion) are investigated. By recording a time dependant correlation of these scattering intensities, the diffusion coefficient can be obtained. Using the Stokes–Einstein equation the hydrodynamic radius of dispersed particles can be calculated. The results of these DLS measurements are shown in Table 9 and confirm the NMR-relaxation time measurements, as well as the SEM images.

Table 9. DLS measurements of GO batch A1 at concentration of 0.025 mg/mL after different sonication times. Every radius is based on three single measurements.

Sonication Time min	$r_{hydrodynamic}$ nm
0	not measurable
1	991 ± 18
5	348 ± 19
10	247 ± 13
20	223 ± 1

Nevertheless, DLS has some disadvantages compared to NMR. Due to the high absorption coefficient of GO and multiple scattering it is necessary to dilute the suspension since otherwise credible DLS measurements are not obtainable [76]. Second, by using DLS it is not possible to measure particles larger than 10 µm [77] and lastly the methods measure the hydrodynamic radius of spherical particles (Stokes–Einstein equation) whereas GO flakes are a 2D

material [75, 78]. Also bending and folding of the GO flakes in suspension have a huge impact on the DLS results and therefore on the reliability of size determination. This results in an underestimation of the measured size using DLS, especially for large sheets since here folding is preferred [79]. Moreover, the measured hydrodynamic radius is not identical with the geometric radius, which can be measured by microscopic determination like SEM, TEM or AFM, since particle and solvent form a solvation shell. This shell can be attached strongly to the particle surface which leads to larger particles and an overestimation in particle size. Due to all of this, the size values, which are obtained, are not accurate and give only a quick indication of the GO flake size respectively a trend.

By using NMR-relaxation time, DLS and SEM it was shown, that an ultrasonic treatment reduces the GO flake size. Furthermore, NMR-relaxation time measurements could prove the decreased flake size without any sample preparation. Since not only size of the GO flakes influences the NMR-relaxation time, further characterizations mainly in terms of chemical composition are necessary. This should identify if ultrasonic treatment influences not only the flake size but also the chemical composition of the GO flakes. Therefore, UV-Vis spectra after different sonication times were recorded and are shown in Figure 24.
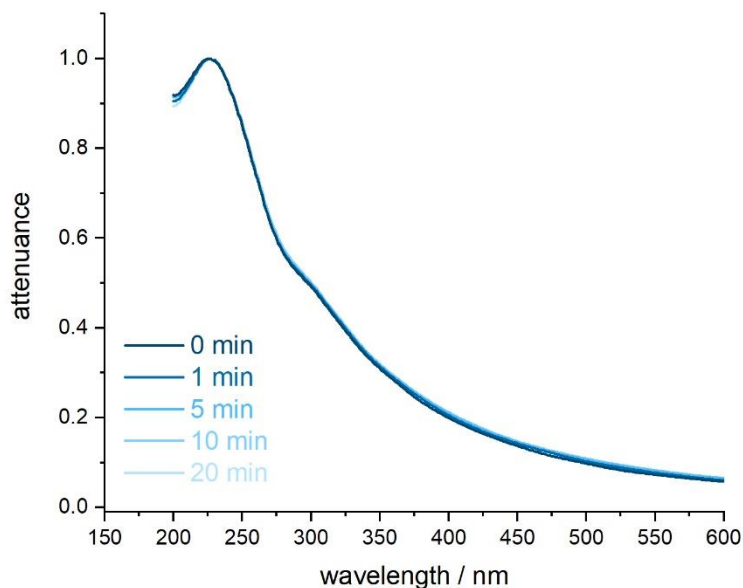
Figure 24. Normalized UV-Vis spectra of GO batch A1 after different sonication times at a GO concentration of 0.025 mg/mL.

As already described in the chapter (4.1.2), UV-Vis spectra of GO suspensions show two characteristic points. First, the $\pi \rightarrow \pi^*$ transition at around 230 nm, which corresponds to the transition of sp^2-domains and the shoulder ($n \rightarrow \pi^*$) at around 300 nm, which corresponds to the transition of carbonyl groups [38]. After sonication no differences between the samples can be observed in the UV-Vis spectra. This illustrates, that the ultrasonic treatment has no influence on the chemical composition of the GO flakes. Furthermore, for all suspensions, the peak maximum (λ_{Max}) is present at 226 nm. This shows, that the size respectively the distance between two sp^2-domains is constant, since λ_{Max} would be blue-shifted by decreased sp^2-domains respectively redshifted by increased sp^2-domains like rGO [80]. Nevertheless, it is also possible, that the non-sonicated GO flakes are already highly oxidized, whereby the distance between two sp^2-domains within the non-sonicated GO flakes is larger than the GO flake size itself of the sonicated samples. In this case, structural changes between non-sonicated and sonicated flakes can't be detected by UV-Vis spectroscopy.

Also, the optical band gaps of GO after sonication were calculated in the same way as already mentioned in chapter 4.1.2 by transferring the recorded UV-Vis spectra into Tauc plots [44]. The calculated optical band gaps are shown in

Table 10. As for the peak maximum λ_{Max}, no difference can be seen for the calculated band gaps of GO after different sonication time. Therefore, UV-Vis spectroscopy shows, that ultrasonic treatment neither has an influence on the chemical composition of the GO flakes nor on the sp^2-domains within the GO flakes.

Table 10. The optical band gaps (E_g) after different sonication times. E_g was determined by transferring the UV-Vis spectra into Tauc plots.

Sonication Time min	Band Gap (E_g) eV
0	4.33 ± 0.01
1	4.33 ± 0.01
5	4.32 ± 0.01
10	4.31 ± 0.01
20	4.32 ± 0.01

Moreover, the sonicated GO suspensions were further characterized by Raman spectroscopy to obtain a more detailed picture if sonication influences the number of defects within GO flakes. The so recorded, averaged and normalized Raman spectra and their corresponding I_D/I_G-ratios after different times of ultrasonic treatment are shown in Figure 25.
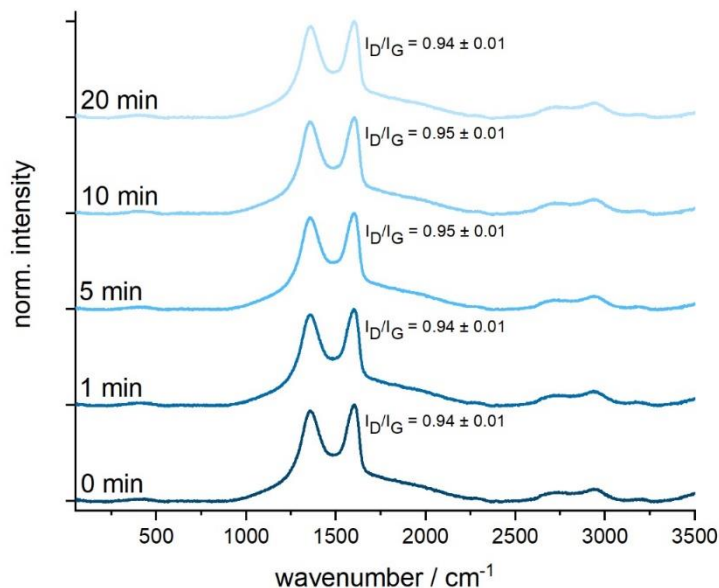
Figure 25. The averaged and normalized Raman spectra of GO batch A1 after different sonication times and their corresponding I_D/I_G-ratios.

All Raman spectra show the presence of the prominent D-peak (1355 cm^{-1}), the G-peak (at 1590 cm^{-1}) and the 2D-peak (at around 2715 cm^{-1}) and are as previously reported [51]. Moreover, the FWHM of the 2D-peak is identical (183.45 ± 2.68 cm^{-1}) across all suspensions and therefore not influenced by ultrasonic treatment. Raman spectroscopy shows, that no further defects are introduced since the I_D/I_G-ratio isn't influenced by the ultrasonic treatment. This result is in agreement with UV-Vis spectroscopy and the corresponding band gaps. As for the GO batches, Raman spectra were recorded, the corresponding I_D/I_G-ratios were determined and statistically evaluated. These ratios are shown as a Box plot diagram in Figure 26.

Figure 26. I_D/I_G-ratios of GO batches A1 (25 spectra per batch) plotted as Box plot. The blue point represents the average I_D/I_G-ratio of every batch. The red box shows the range, where 50% of the I_D/I_G-ratios are pre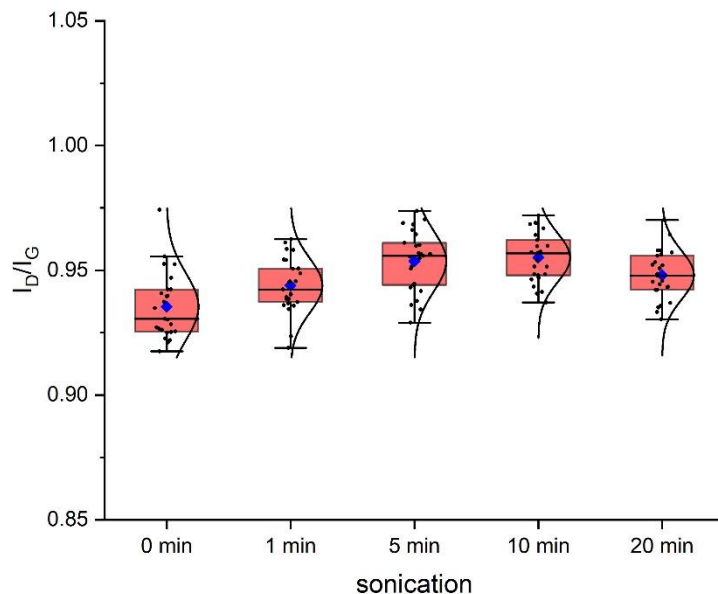sent. The black antennas exhibit the other 50% of the determined ratios, whereas 25% of all ratios are above the red box and 25% are below. The black horizontal line within the red box is the median of all ratios.

Comparing the average respectively median values of the GO suspensions slight differences of around 0.01 can be seen, but no correlation between I_D/I_G-ratio and sonication time can be observed. Also, the distribution (around 0.03) which is indicated by the antennas (highest and lowest 25% of the values), stays constant. This shows, that the number of defects and therefore the oxidation degree remains constant and isn't influenced by sonication. Also, the FWHM of the 2D-peak as well the defect to defect distance (L_D) were determined as described in chapter 4.1.2 and are shown in Table 11. Here, neither the FWHM nor the defect to defect distance is influenced by the ultrasonic treatment which indicates, that ultrasonic treatment reduces the GO flake size and does not introduce further defects or reduce the defect to defect distance.

Table 11. Determined $FWHM_{2D}$ of GO batch A1 after different sonication times and the calculated defect to defect distance (L_D) of GO batches according to Cancado.

Sonication Time min	$FWHM_{2D}$ cm^{-1}	L_D nm
0	178.6 ± 10.5	12.48 ± 0.09
1	184.1 ± 7.7	12.43 ± 0.07
5	184.4 ± 11.5	12.37 ± 0.08
10	186.8 ± 7.6	12.36 ± 0.06
20	183.3 ± 9.3	12.41 ± 0.06
Ø	**183.5 ± 3.0**	**12.41 ± 0.05**

To exclude, that the number of defects stays constant during sonication, whereas the kind of defects changes due to ultrasonic treatment, the sonicated GO samples were further investigated by XPS.

These spectra after different sonication times are shown in Figure 27. All C1s spectra show the presence of a sp^2- and sp^3-hybridized carbon at 283.8 eV respectively 284.7 eV [55]. Furthermore common GO defects like -O-C-O- and -C-OH, which are assigned to epoxide- and alcohol-groups at 286.6 eV, -C=O, which are associated to ketones, quinones and aldehydes at 287.9 eV and -C(O)O-, which corresponds to esters- and carboxyl-groups at 288.6 eV are present. Also, the O1s-spectra confirm the attendance of -C-O-C- respectively -C-OH, -C=O and C(O)O- groups at 531.2 eV, 532.3 and respectively 533.2 eV as previously reported [55].

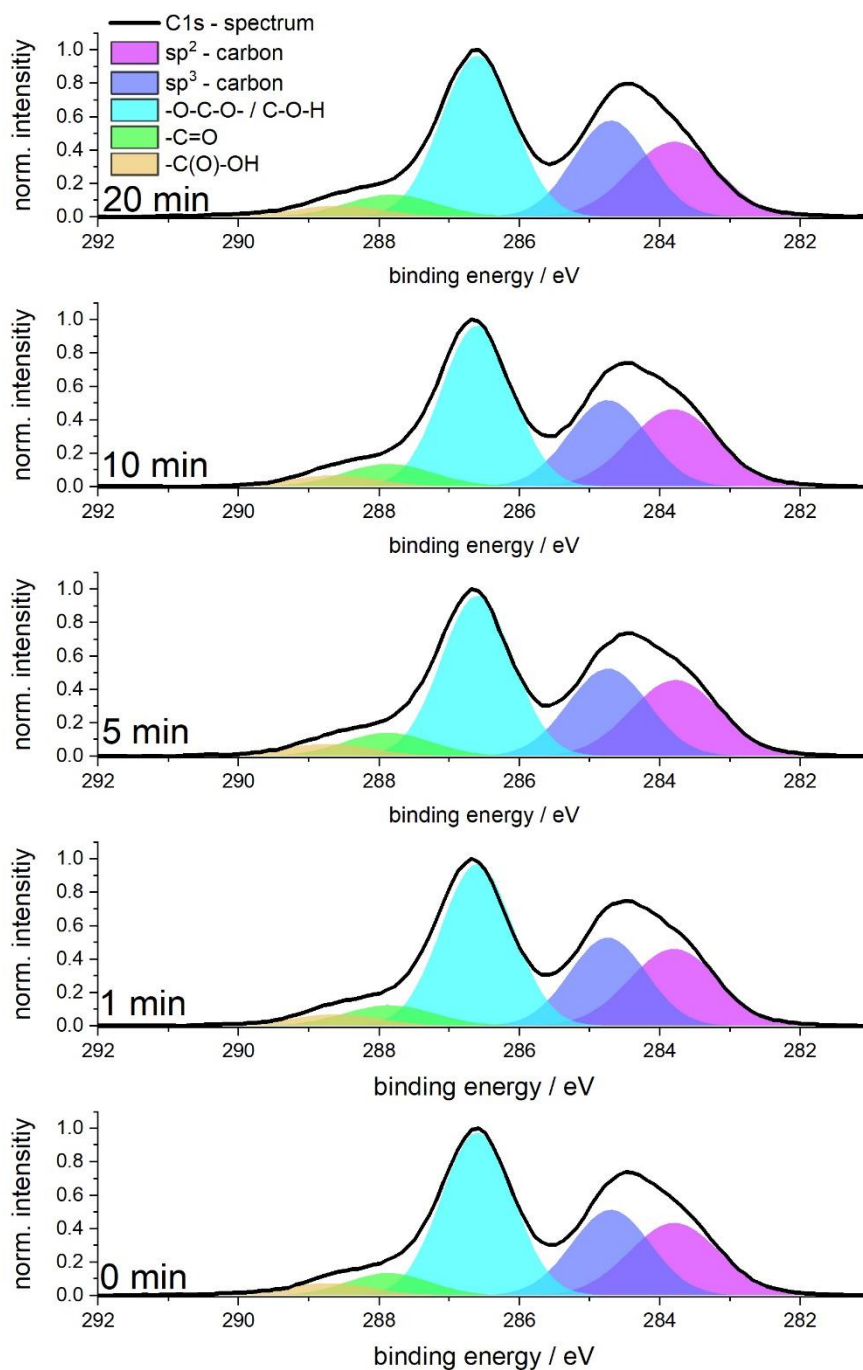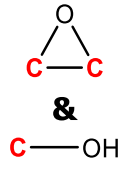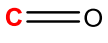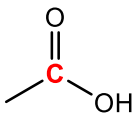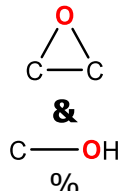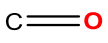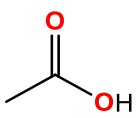**Figure 27.** The detailed XPS C1s spectra of GO batch A1 after 0 min, 1 min, 5 min, 10 min, and 20 min of ultrasonic treatment.

The quantitatively determination of the single compounds was done in the same way, as for the GO batches and is shown in Table 12.

Table 12. The detailed quantification of the individual components of the XPS C1s and O1s spectra (GO batch A1) after different sonication times. Evaluation was made by "Unifit 2012". Measurements were made at TH Deggendorf in Taisnach.

C1s spectra	sp^2	sp^3	C–O–C & C–OH	C=O	COOH
	%	%	%	%	%
0 min	15.7	16.3	28.3	4.5	2.7
1 min	16.4	16.1	28.1	4.4	2.5
5 min	15.9	16.4	27.0	4.7	2.6
10 min	16.5	16.1	27.3	4.8	2.4
20 min	15.9	17.2	27.8	4.7	2.4
Ø	**16.1 ± 0.3**	**16.4 ± 0.4**	**27.7 ± 0.6**	**4.6 ± 0.2**	**2.5 ± 0.1**
O1s spectra			C–O–C & C–OH	C=O	COOH
			%	%	%
0 min			25.3	4.7	2.6
1 min			25.5	4.7	2.3
5 min			26.2	4.8	2.4
10 min			26.0	4.7	2.4
20 min			25.1	4.5	2.5
Ø			**25.6 ± 0.5**	**4.7 ± 0.1**	**2.4 ± 0.1**

Between the sample slight changes can be observed which do not correlate with the duration of the ultrasonic treatment or the NMR-relaxation time. Even more, the carbon content (67.3% ± 0.5%) respectively oxygen content (32.7% ± 0.5%) stays constant, which indicates, that no further oxygen is introduced into the carbon lattice. These results confirm the Raman- and UV-Vis spectroscopy, including the determined band gaps.

As relaxation mechanism after photoionization, besides X-ray fluorescence, the Auger effect can also take place in an XPS measurement. In such an Auger process (3 electron process), an excited energetic state of a single-ionized atom (such as that produced by the emission of a photoelectron (2 electron process)) decays without radiation, with the emission of an additional electron. In XPS, therefore, both photoelectron and Auger electron lines appear. For the characterization of graphene or graphene related materials, especially the Auger C_{KLL}-peak (1190 eV - 1250 eV) is of great interest, due to participation of carbon valence orbitals the sp^2/sp^3-ratio can be investigated [81-83]. Therefore, the first derivative of the C_{KLL} spectrum has to be formed. The distance (D) between the most positive maximum and most negative minimum in the first derivative represents to the so-called D-parameter. This D-parameter depends on the ratio of sp^2/sp^3 carbon and ranges from 13 eV for diamond (pure sp^3-hybridization) up to 21 eV for graphite (pure sp^2-hybridization). The measured C_{KLL}-peak after ultrasonic treatment for 0 min, 1 min, 5 min, 10 min and 20 min, the derivatives and the corresponding D-parameters are shown in Figure 28. These derivatives were obtained by the XPS evaluation software "Unifit 2012". For this purpose, the C_{KLL} spectra were smoothed for three times and finally derived. The distance in eV between minimum and maximum of the corresponding derivatives was finally determined.
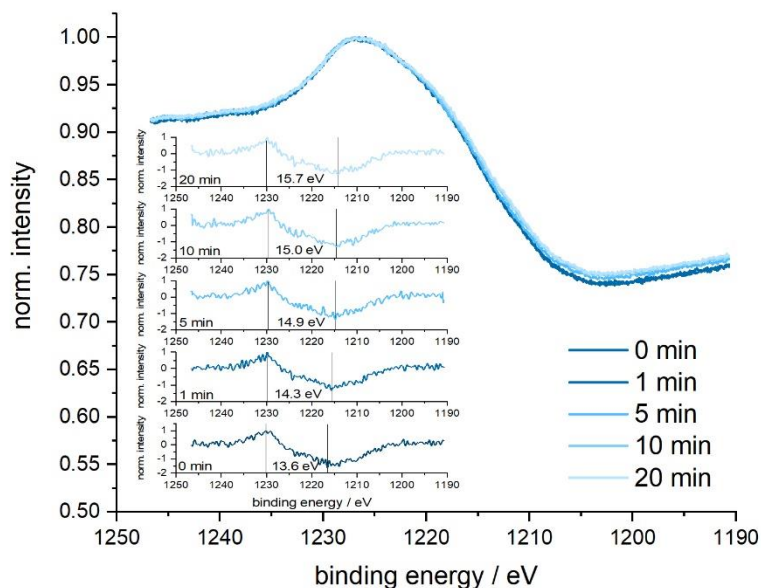
Figure 28. The Auger C_{KLL} spectra of GO batch A1 after different sonication times. <u>Insert:</u> The corresponding first derivatives of the C_{KLL} spectra and their D-parameter.

It is clearly visible, that ultrasonic treatment leads to an increased distance between maximum and minimum which corresponds to an increased D-parameter value. Whereas the D-parameter without ultrasonic treatment is 13.6 eV, the parameter increases over 14.9 eV after 5 min of sonication up to 15.7 eV after 20 min of ultrasonic treatment. This trend shows, that the fraction of sp^2-hybridized carbon atoms is increased after ultrasonic treatment. First, this result is not in agreement with XPS quantification as in (Table 12), where the values of sp^2- and sp^3-hybridized carbon from the C1s signal are constant for different sonication times. However, it must be taken into account that these quantifications are achieved by fitting of the individual components until they are as close as possible to the measured XPS detail spectrum. This may lead to certain inaccuracies. It is also conceivable that the changes due to ultrasonic treatment are lower than the signal to noise ratio of the measurements itself. Therefore, the usage of the D-parameter may be advantageous because is there no need to fit, to obtain information about the sp^2- and sp^3-fractions of GO.

The carbonyl to epoxide ratio, which corresponds to the edge to area ratio of the GO flakes as well the D-parameter are plotted against the flake size in Figure 29.
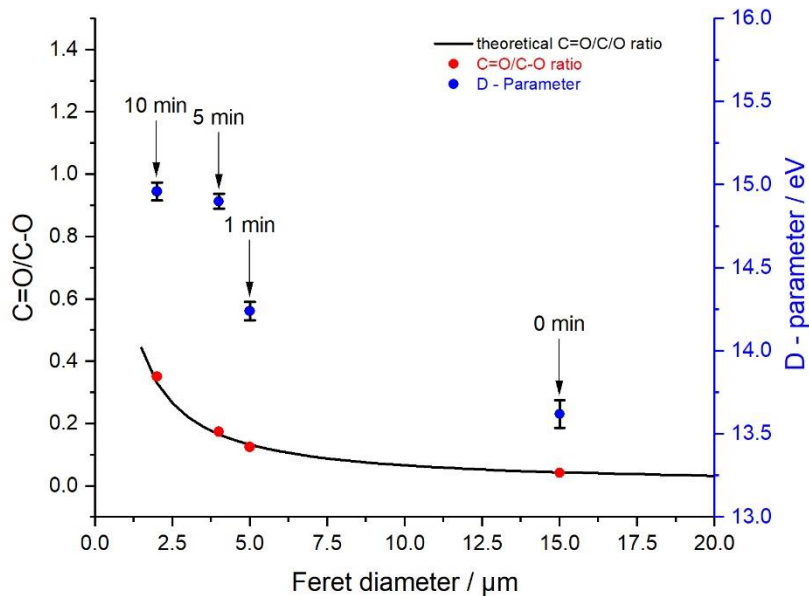
Figure 29. Dependency of the carbonyl to epoxide ratio (C=O/C-O ratio) and D-parameter against the lateral GO flake size (Feret diameter) after different sonication times.

Based on the increased D-parameter after sonication the following model can be set up. Oxygen containing defects have a preferred position within the GO flake, with epoxy containing groups in the middle of the GO flakes and carbonyl groups at the GO flake edges. Ultrasonic treatment breaks the GO flakes at epoxide containing groups into the smaller fragments. The newly formed edges are saturated by carbonyl groups which originate from the epoxy groups. This leads to an increased fraction of sp^2-hybridized carbon after sonication. A transformation of an epoxide group into a carboxyl group can be excluded since a break of a C-C bond would be required [57]. An introduction of oxygen atoms due to sonication can be excluded since the oxygen content as well the carbon content of GO is the same as before ultrasonic treatment.

In addition to that, Figure 30 shows the comparison of the D-parameter and the mean values of the I_D/I_G-ratio, which are already discussed in Figure 26.
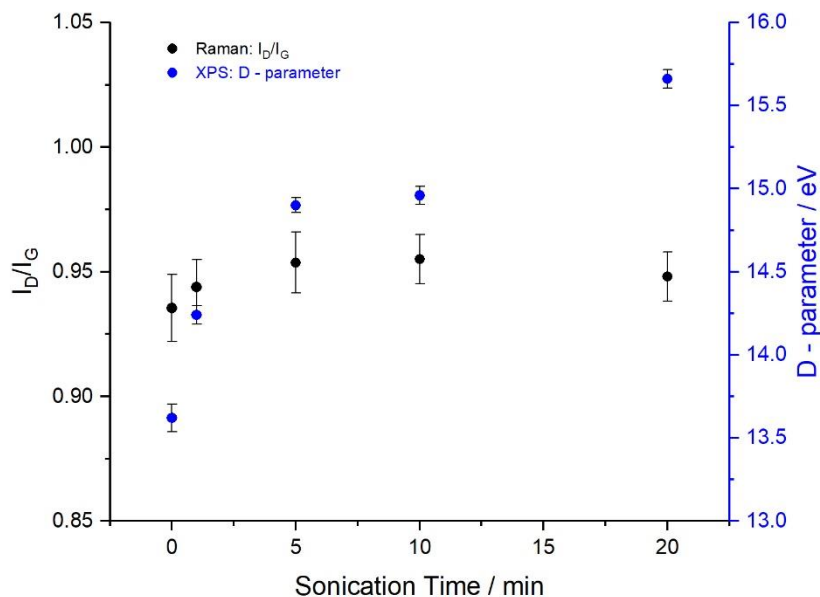
Figure 30. Comparison of the mean values of the I_D/I_G-ratio and the D-parameter after different sonication times.

Comparing the D-parameter which shows a strong influence after sonication, the I_D/I_G-ratios exhibit only slight changes when the mean values are compared and the error bars are neglected. However, oxygen containing groups are characterized by Raman spectroscopy only by the number and not by the kind of defect. Therefore, Raman spectroscopy measures the same I_D/I_G-ratio, when an oxygen containing group is transferred into another defect due to ultrasonic treatment. Moreover, *Cancado et al.* report, that the I_D/I_G-ratio reaches a maximum at a defect to defect distance of 3 nm. Due to this, XPS should be preferred to get a more detailed picture especially concerning the qualification of defects within the carbon lattice. Here, the stronger sensitivity of the D-parameter against the flake size compared to C1s and O1s spectra is based on the investigation of different classes of electrons. Whereas C1s or O1s spectra observe the electrons of the 1s shell of the respective atom which are very close to the atomic nucleus the C_{KLL}-peak investigates the valence electrons of the carbon atoms which are part of the bindings within the graphene lattice. Based on this, the C_{KLL}-peak is a very revealing parameter which gives a good overview on the hybridisation in GO. Nevertheless, a C_{KLL} detail spectrum with low signal

to noise ratio needs around 1 h measuring time and it must be carefully evaluated how much information is needed.

4.2 System Integration of Graphene Oxide Suspensions

The transfer of the graphene is a very critical point, since it can be damaged [21] due to chemical or mechanical stress [84]. Next to a reliable transfer, also the price and the time factor of the graphene transfer has to be taken into account for industrial purpose [85]. As for the graphene synthesis, several techniques for the graphene transfer are already described in literature, e.g., mechanical exfoliation, polymer assisted transfer, continuous transfer or transfer-free methods, which include the synthesis directly on the desired substrate [86]. Since all these transfer techniques include chemicals, the graphene transfer can be divided into two groups: wet chemical methods and dry chemical methods where the transfer experiment is done in wet respectively dry environment [21]. Unfortunately, all these mentioned methods use graphene flakes, which are already attached to a synthesis-dependent substrate like scotch tape, polymers, nickel or copper [86]. To transfer suspended graphene several techniques are already described in literature, e.g., drop-casting [87], spin-coating [88], micro-dispensing, respectively ink-jet printing [89] and are compared in Table 13. Next to a high process control which is based on a reliable and reproducible transfer, also the automation capability on wafer scale is an important factor in the semiconductor industry [85]. Due to this, drop casting and spin-coating are not the method of choice since their scalability is poor. Here micro-dispensing as well as ink-jet printing are the superior methods. The main difference between these two techniques is the droplet size, which is deposited on the target substrate. This differences in droplet size leads to various requirements for the graphene deposition. Especially, for ink-jet printing these requirements like viscosity or droplet formation are much higher than for micro-dispensing. By micro-dispensing, aqueous suspensions can be deposited. This is not possible for inkjet printing, since this technique is limited on suspensions consisting of organic solvents.

Table 13. Overview and comparison of commonly used deposition techniques for suspended graphene ink.

Deposition Technique	Advantages	Disadvantages
Drop-Casting	- cheap - no hardware	- inhomogeneous layer - less throughput - large deposition volume
Spin-Coating	- cheap - large areas	- semi-automated - no defined spot sizes - large deposition volume
Ink-Jet Printing	- wafer-scale ready - fully automatable - defined spot size	- hardware - complex ink preparation - additives
Dispensing	- wafer-scale ready - fully automatable - defined spot size	- hardware - less variable spot size than ink-jet printing

The ability to form droplets and therefore the printability can be investigated by the dimensionless figures of merit like Reynolds-, Weber-, and Ohnesorge numbers which describe the fluid rheological properties [24-90]. Furthermore, by adding organic additives [91-93] these numbers can be influenced positively, which results in printability in general or enhanced printability. Nevertheless, such additives may interfere with the later application and have an influence on the electrical conductivity or sensitivity [94]. Due to this, the ink formulation is more complicated than for micro-dispensing [95]. An advantage of ink-jet printing is the fact, that smaller droplets get deposited, which results in a higher lateral resolution and therefore in a higher variable spot size. However, ink-jet printing is less robust than micro-dispensing, so in the following micro-dispensing will be used as method to deposit GO.

Since GO exhibits non-conductive behaviour, it is necessary to reduce GO for regaining the electrical conductivity. In principle, there are two methods, which are commonly used. First, GO can be reduced chemically by hydrazine or other reductive agents directly in suspensions [96, 97]. Unfortunately, the obtained

rGO suspensions show less stability in simple aqueous solvent systems, which leads to agglomerations and further impurities, based on the chosen reducing agent [35]. Therefore, the thermal reduction of GO in an RTP-oven by using a reducing gas atmosphere [98] is the preferred method. Next to this, the whole thermally reduction of the deposited GO can be done on wafer-scale. Finally, the deposited sensor layers will be analysed in electrical characterization, since the readout of the final sensor application should be done electrically. This readout has several advantages compared to optical or immunological sensor applications since electrical hardware is cheap and can be easily miniaturized. Furthermore, the electrical characterization of the sensor layers can be done on wafer-scale and is already a very commonly used technique in the semiconductor industry, to characterize products respectively applications.

4.2.1 Homogenous and reliable Graphene Deposition by Micro - dispensing

In general, it is a challenge depositing graphene containing suspensions, while avoiding coffee-ring formation, since the coffee-ring has different properties like electrical conductivity compared to the rest of the deposited area. The formation of the coffee-ring takes place, when the solvent of the suspension evaporates whereas the dispersed flakes moves to the droplet edges driven by capillary forces, the so-called Marangoni effect [74, 99]. This can be overcome by a deposition at higher temperature, which results in a faster solvent evaporation, whereas the time for the graphene motion to the droplet edge is too short [100]. Also, the addition of surfactants would be possible [101], but that's not an option here since additives as these would have to be removed after the transfer. Furthermore, the wettability between the GO suspension and the substrate is an important factor for homogenous graphene layers. In the case of poor wettability, it is necessary to increase the surface energy of the substrate which results in an enhanced wettability for aqueous suspensions [102]. Oxygen plasma was used for sample pre-treatment which additionally removes

impurities on the surface as well as residues of the photoresist since these also have a negative influence on the wetting properties of the deposited GO. Since a continuous GO deposition is also part of a homogeneous layer, different GO concentrations were deposited and characterized by laser microscopy in order to investigate, at which GO concentration a closed and continuous layer is formed. The recorded images are shown in Figure 31.
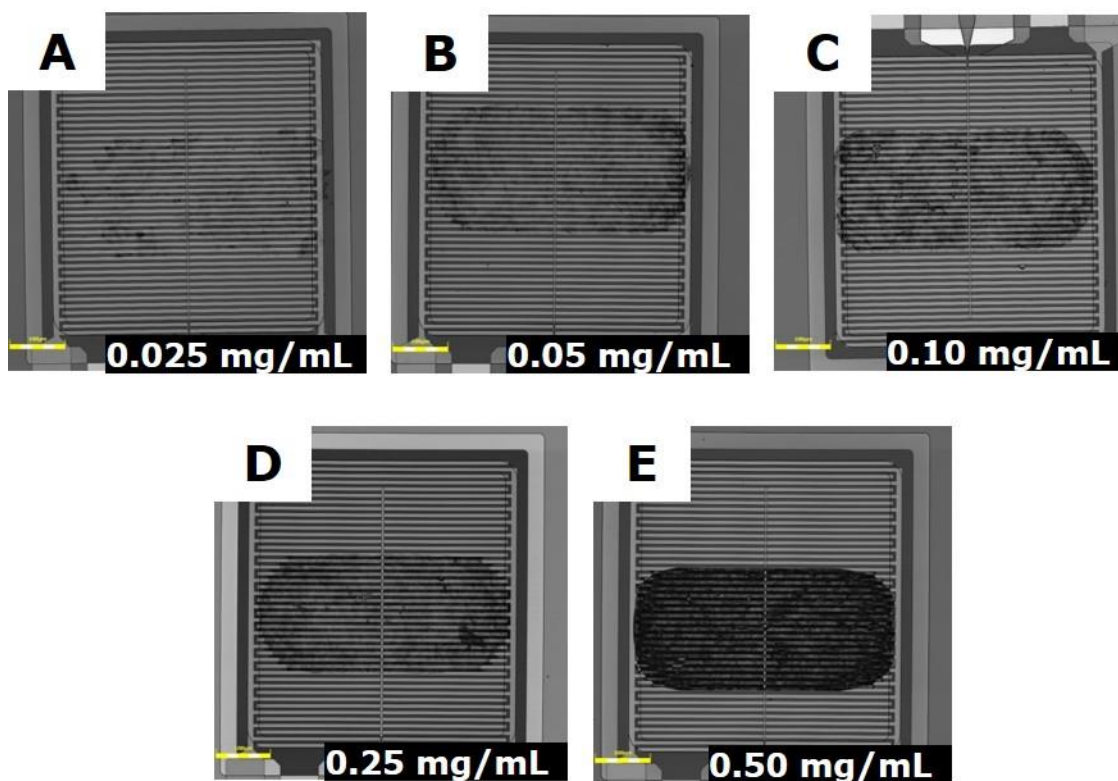
Figure 31. Laser microscopic images of micro-dispensed GO suspension with different concentrations at 20x magnification. **(A)** 0.025 mg/mL, **(B)** 0.05 mg/mL, **(C)** 0.1 mg/mL, **(D)** 0.25 mg/mL and **(E)** 0.05 mg/mL.

Neither shape nor size of the droplet are dependent from the GO concentration which indicates, that the dispensing process is not influenced by the viscosity of the suspension. This makes the comparison between the different GO concentrations much easier, since it can be assumed that the spot area (450 µm x 200 µm), in which the deposition takes place, is constant. Moreover, the images show, that the amount of GO at the concentrations of 0.025 mg/mL respectively 0.05 mg/mL (Figure 31 (A) and (B)) is not enough to fill the spot area completely. However, coating of the spot area is an important factor, since otherwise the active electrode area would be varying which would influence

properties like the sensitivity of the final application. GO concentrations at 0.25 mg/mL or higher (Figure 31 (D) and (E)) are able to fill the spot area completely. For the deposition at a GO concentration of 0.1 mg/mL it is not clearly visible, if the brighter areas of the deposited spot are covered by GO flakes. Therefore, it will be assumed, that completely covered spot areas will be reached at a GO concentration of 0.25 mg/mL. The deposited GO exhibits sharp spot edges for all GO concentrations without any coffee-ring formation. All these findings show well controllable and homogenous GO deposition by micro-dispensing. Next to this, the chosen process parameters such as the deposition temperature and the oxygen plasma before deposition influences the GO deposition in a positive way as predicted.

Next to a continuous deposition also a constant layer thickness of deposited GO is important to reduce drastic changes in electrical resistance within the deposited GO spot. Therefore, sections across the gold fingers were made using FIB-Cut and, imaged by SEM. In Figure 32, the FIB-Cut SEM images show, that GO layer thickness is correlating with the GO concentration. For the GO concentrations of 0.025 mg/mL and 0.05 mg/mL (Figure 32 (B) and (C)) the GO layers are below 10 nm and very difficult to observe. For increasing GO concentration (Figure 32 (D) – (F)) the GO layer thickness increases as well. The cavity in Figure 32 (F) is due to imperfect metallization during the chip fabrication and not due to bad wetting of the graphene material. Furthermore, the deposited GO encloses the observed gold fingers completely with a constant layer thickness at all concentrations.
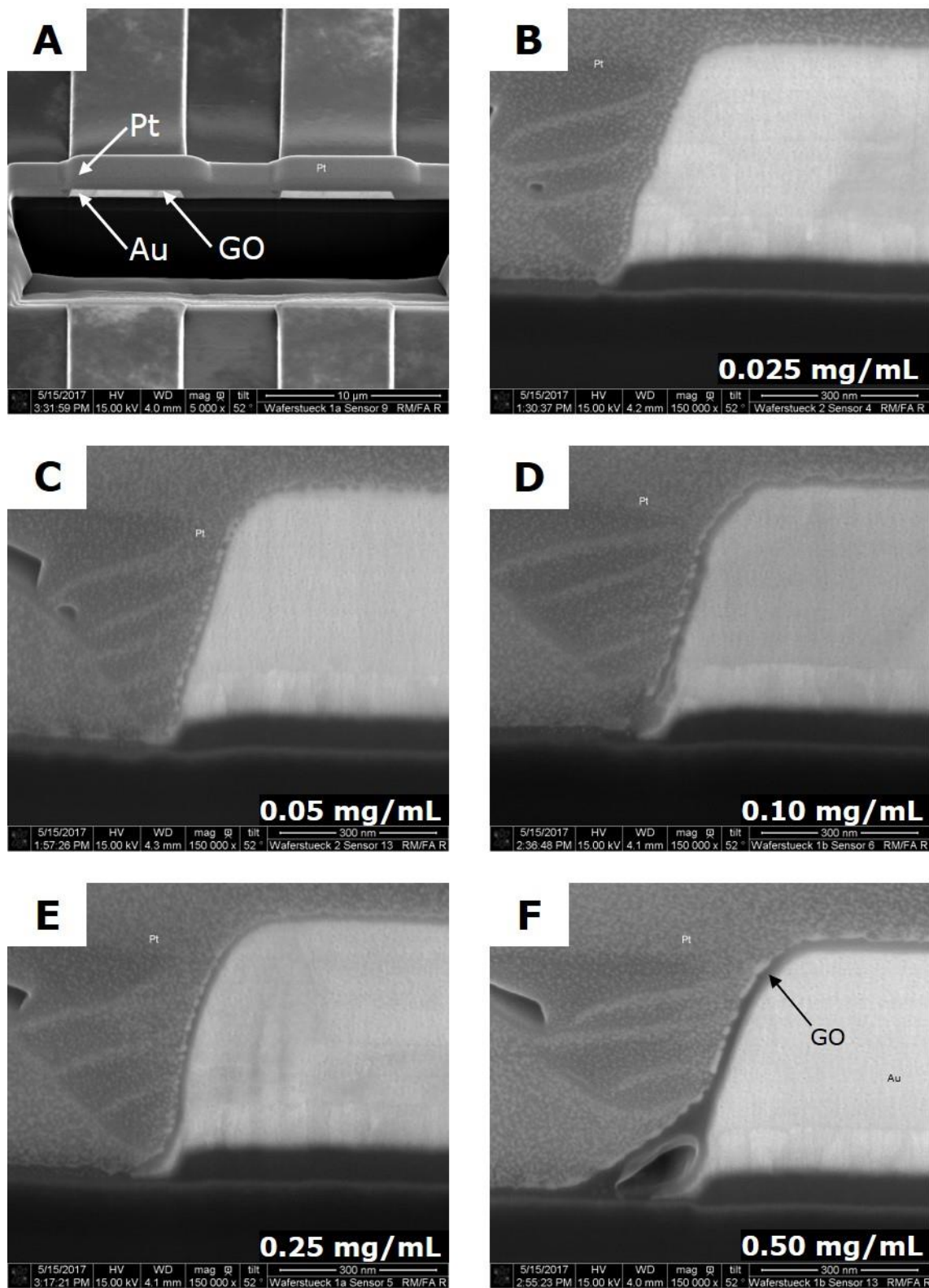
Figure 32. FIB-Cuts SEM images of micro-dispensed GO at different concentrations. **(A)** Overview with cut across two fingers, **(B)** at 0.025 mg/mL, **(C)** 0.05 mg/mL, **(D)** 0.10 mg/mL, **(E)** 0.25 mg/mL and **(F)** 0.50 mg/mL.

Finally, the GO thicknesses were analyzed with the software imageJ and are shown in Table 14. Here, a large increase of the layer thickness between 0.05 mg/mL and 0.10 mg/mL was observed. This large difference indicates, that GO concentration of 0.1 mg/mL or lower cannot cover the micro-dispensed spot size (450 µm x 200 µm) completely with a continuous layer. Due to the optical results of laser microscopy and FIB-Cut SEM a GO concentration of 0.25 mg/mL is necessary to get a homogenous and continuous layer deposition by micro-dispensing.

Table 14. Layer thicknesses of deposited GO at different concentrations determined FIB-Cut SEM and analyzed by the software imageJ.

GO Concentration mg/mL	GO Layer Thickness nm
0.025	7.85 ± 1.19
0.05	9.25 ± 1.61
0.10	17.64 ± 0.68
0.25	22.86 ± 1.95
0.50	24.04 ± 0.65

Next to the optical characterization, the structural homogeneity of the deposited GO layer was analysed by Raman spectroscopy [103]. Therefore, Raman line scans were recorded and the defect density (I_D/I_G) was investigated along the micro-dispensed spot. Figure 33 shows the I_D/I_G-ratios (average of three individual scans) of micro-dispensed GO at 0.05 mg/mL, which represents an inhomogeneous layer and 0.25 mg/mL which represents a homogeneous layer.
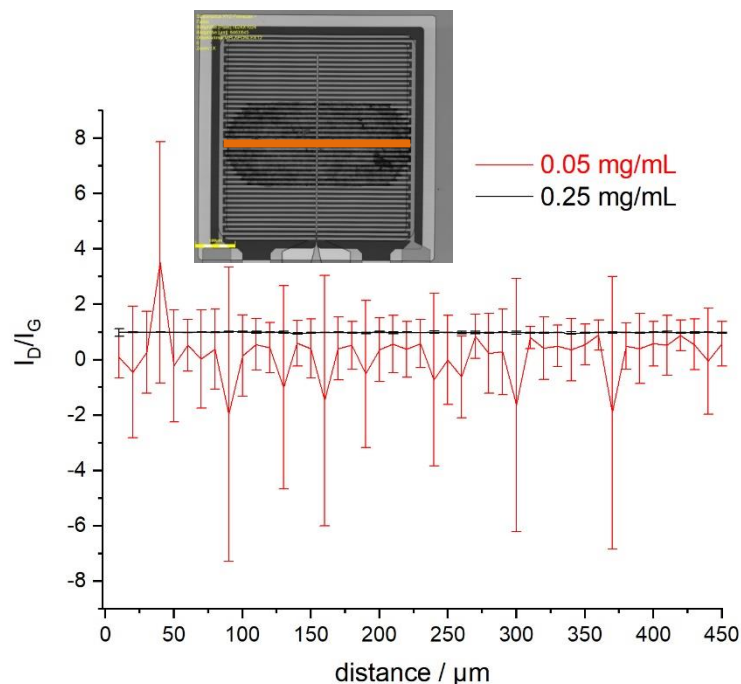
Figure 33. Averaged I_D/I_G-ratio of three single line scans along the deposited GO spot at 0.05 mg/mL (red) and 0.25 mg/mL (black).

The I_D/I_G-ratio at 0.05 mg/mL shows a large distribution (0.96 ± 0.35) which is equivalent to non-homogenous layer based on a non-continuous dispensing. The I_D/I_G-ratio at 0.25 mg/mL displays nearly no distribution. This corresponds to the optical characterization and exhibits a continuous GO layer formation. Furthermore, the ratio shows, that the deposition at 0.25 mg/mL is very homogeneous which also can be expressed by the overall I_D/I_G-ratio of 0.98 ± 0.02. After the thermal reduction, the layer was also analysed by a Raman line scan as before. The oxidized and reduced material I_D/I_G-ratios along the deposited layers are shown in Figure 34.
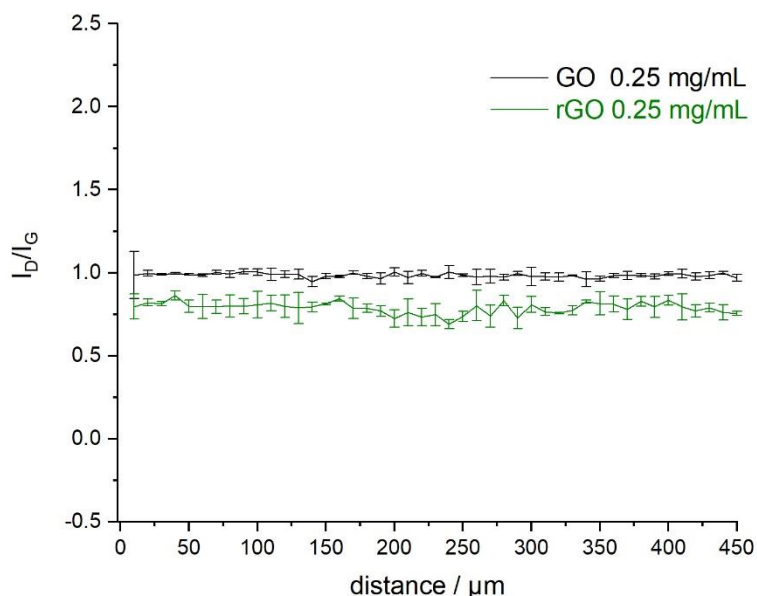
Figure 34. Averaged I_D/I_G-ratio of deposited GO spot 0.25 mg/mL before (black) and after the reduction of GO (green).

The decreased I_D/I_G-ratio of 0.70 ± 0.03 (compared to 0.98 ± 0.02 for unreduced GO) exhibits a successful thermal reduction to rGO [104].

Another aspect that has been disregarded until now is the deposited volume per spot during the micro-dispensing process, since an increased deposition volume leads to a larger respectively thicker spot which results in a decreased electrical resistance [105, 106]. The micro-dispensed layers were analyzed electrically by U-I measurements. Here, the voltage was swept, and the current was measured. Finally, the sensor resistance was calculated based on Ohm's law. The electrical characterization of such deposited rGO layers have some more advantages. Unlike FIB-Cut SEM, electrical characterization can be done automatically in a high throughput and is a non-destructive characterization technique when not too much power is applied. Moreover, a reproducible sensor layer resistance with narrow distribution is from great interest, because the effort involved in measuring as well as data evaluation like developing an algorithm can be reduced for the final sensor application. The electrically characterization of the deposited rGO layers are shown in Figure 35.
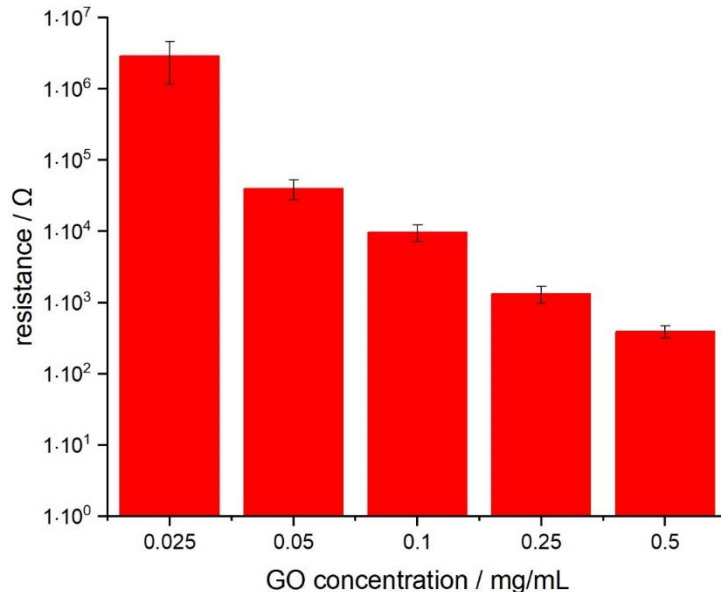
Figure 35. Electrical resistance of micro-dispensed rGO layers at different GO concentration

A drastic influence of the GO concentration on the electrical resistance can be observed. GO concentration of 0.025 mg/mL respectively 0.05 mg/mL show resistances in the MΩ-range. All other concentrations (higher than 0.10 mg/mL) exhibit resistances in the kΩ-range. Since the number of adsorption sites correlates with the electrical resistance of the sensor layer, too low electrical resistances should be avoided due to reduced sensitivity [107]. Therefore, a sensor layer resistance in the low kΩ-range is very desirable for such applications. A further important aspect is, that the electrical resistance of the deposited GO layers has to fit to the ASIC. If this is not the case, the sensor response quality can be reduced, e.g., by an increased signal to noise ratio. According to electrical resistance and the optical characterization, layers dispensed with a GO concentration of 0.25 mg/mL have shown the best results. Furthermore, the electrical resistance correlates to the layer thickness (FIB-Cut SEM), as already described in literature [105, 106] and confirm the findings of the electrical characterization and laser microscopy. The high deviation in resistance (around 25%) is still remaining a challenge and it is desirable to reduce the deviation for a better process control by at least a factor 2 to 3 (< 10%). A reason for the deviation could be, that the GO flake sizes influences the resistance of the deposited GO, because in the case of smaller graphene

flakes more flake to flake connections are needed to get an electrical layer which may decrease the electrical conductivity.

In general, it could be shown by optical, spectroscopical and electrical characterizations, that GO concentrations of around 0.25 mg/mL or higher form homogeneous and continuous GO layers of 450 μm x 200 μm in size. Therefore, aqueous suspended GO can be used without any addition of stabilizing agents. Also, the formation of a coffee-ring effect was successfully avoided by increasing the surface energy via oxygen plasma. A comparison of deposited GO layers with and without oxygen plasma are shown in Figure 36.
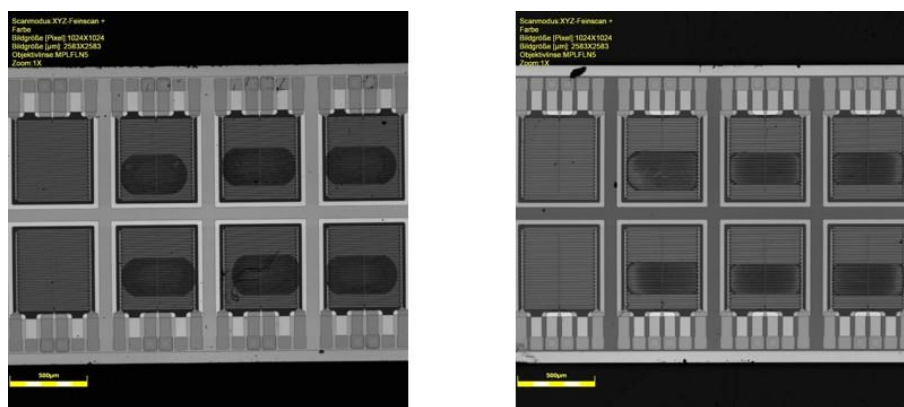
Figure 36. Left: Micro-dispensed GO layers after an oxygen plasma treatment. **Right:** without oxygen plasma treatment.

4.2.2 Influence of the lateral Graphene Oxide flake size on the Micro – dispensing process

GO suspensions contain flakes in the range of a few nanometers up to a few micrometers and their properties, e.g., young modulus, viscosity or electrical conductivity [108] are influenced by the lateral size. Based on this, further investigations regarding the flake size and their system integration were performed. Therefore, the GO suspensions after 1 min respectively 10 min ultrasonic treatment (as already mentioned in chapter 4.1.3) were used. For the suspensions a GO concentration of 0.25 mg/mL was chosen, because the best layer homogeneity was achieved. After micro-dispensing the GO layers were finally characterized. In Figure 37 the laser microscopy pictures of the deposited GO after different sonication times are shown.
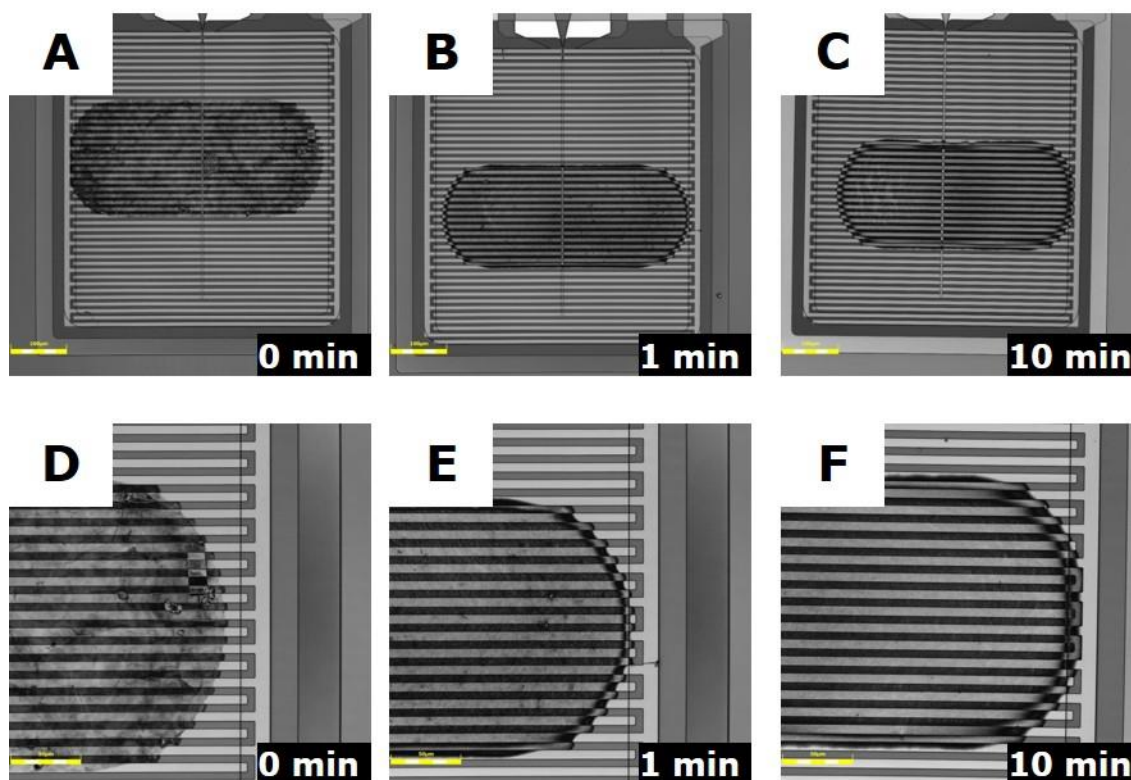
Figure 37. Laser microscopy images of micro-dispensed GO layers which were sonicated for different times at a concentration of 0.25 mg/mL. **(A)** - **(C)** at a magnification of 20x and **(D)** - **(F)** at a magnification of 50x.

Whereas no coffee-ring formation can be seen without ultrasonic treatment (Figure 37 (A) and (D)), a strong coffee-ring formation takes place after sonication (Figure 37 (B), (C), (E) and (F)). Furthermore, the coffee-ring formation correlates strongly with the sonication time and therefore with the lateral GO flake size [109], whereas the deposited graphene layer thickness is strongly reduced with increased sonication time. Consequently, a non-negligible amount of GO is located in the coffee-ring. Moreover, a discontinuous layer after 10 min of ultrasonic treatment can be observed (brighter spots on the left side in Figure 37 (C)). All these findings show, that the GO system integration is strongly influenced in terms of layer thickness and coffee-ring formation by the GO flake size. To get more knowledge about the uniformity and the reduction of GO layer thickness, FIB-Cuts followed by SEM images were performed with these samples. Therefore, the samples were cut in the center of the sensor field (across three gold fingers as in chapter 4.2.1) and are shown in Figure 38.
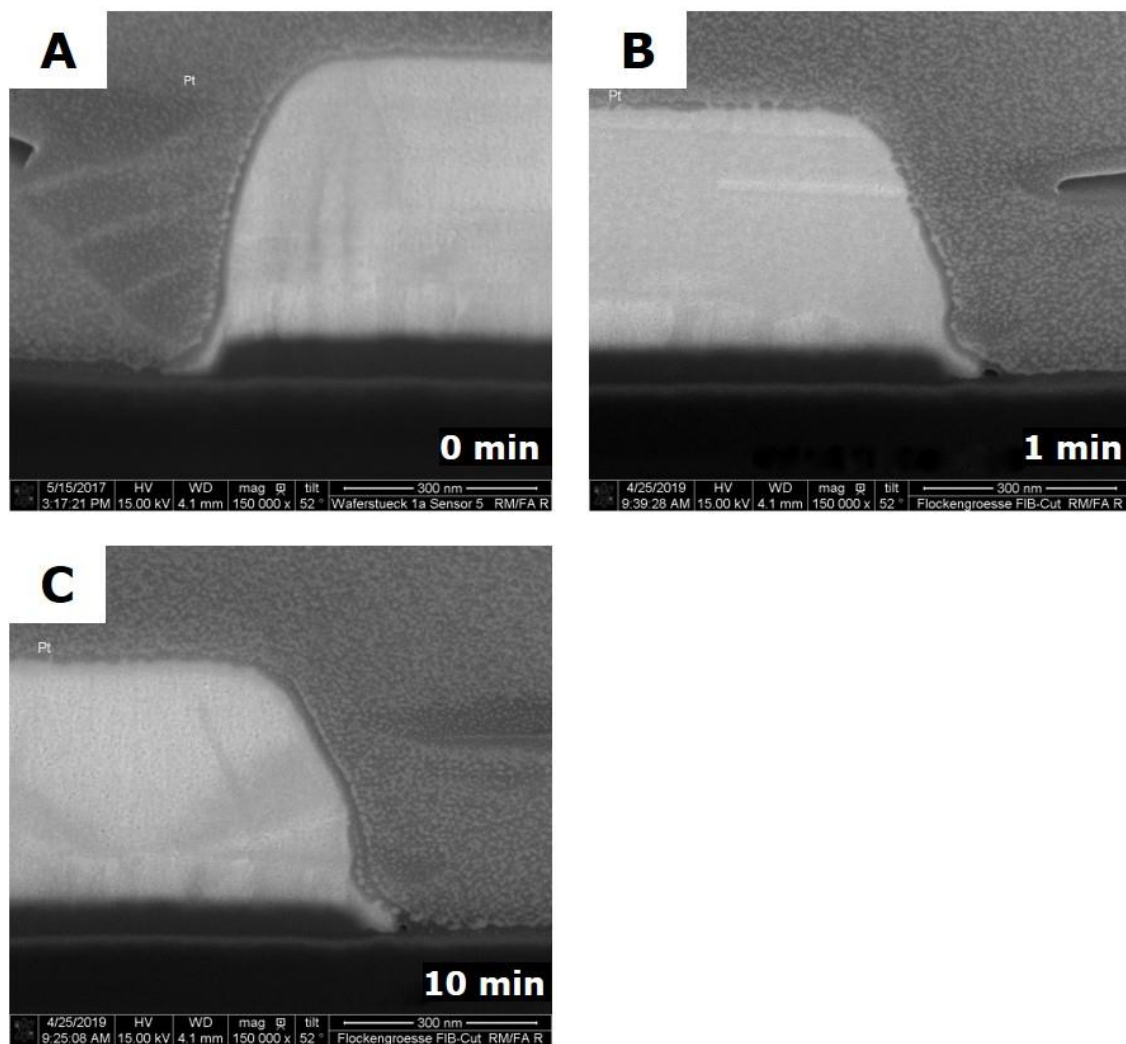
Figure 38. FIB-Cut SEM images after different sonication times at a GO concentration of 0.25 mg/mL, **(A)** without sonication, **(B)** after 1 min of sonication and **(C)** after 10 min of sonication.

By comparing the FIB-Cut SEM images, the difference in layer thickness is confirmed. The corresponding GO layer thicknesses were determined on top of the corresponding gold finger by using the software imageJ and is shown in Table 15.

Table 15. GO layer thickness on top of the gold finger after different sonication times at a constant GO concentration of 0.25 mg/mL determined by FIB-Cut-SEM and imageJ.

Sonication Time min	GO Layer Thickness nm
0	22.86 ± 1.95
1	15.39 ± 2.97
10	15.07 ± 5.02

The determined GO layer thicknesses are in agreement with the laser microscopy images. Moreover, non-sonicated GO flakes form a continuous layer with a constant layer thickness, whereas smaller GO flakes are not able to form a constant layer thickness distributed over the complete gold finger at the same dispensing parameters. Here, the GO layer thickness on top of the gold finger is reduced compared to the side which explains the decreased GO layer thickness for smaller GO flakes. Next to this, an additional reason for the reduction of GO layer thickness is the strong coffee-ring formation, because a high amount of the GO flakes is located at the droplet edge. Since the GO flakes are reduced in lateral size after sonication, a final reason for the decreased layer thickness could be, that smaller GO flakes form thinner and denser layers compared to larger GO flakes. To investigate structural changes of GO after dispensing, Raman line scans were performed. Figure 39 compares these line scans after 0 min and 10 min of sonication.
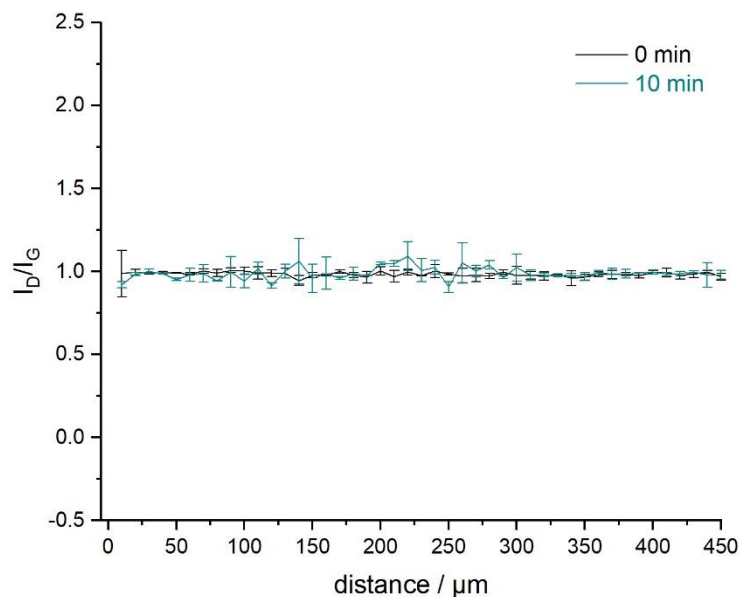
Figure 39. Averaged I_D/I_G-ratio of deposited GO spot 0.25 mg/mL without sonication (black) and after 10 min of sonication (turquoise).

Both Raman line scans show together with the Raman measurements of the GO characterization, that the system integration via micro-dispensing has no influence on the I_D/I_G-ratio of GO, which means that micro-dispensing introduces no further defects and the structural disorder of GO is unchanged. Moreover, no structural differences between sonicated and non-sonicated GO layers can be seen by comparing the I_D/I_G-ratios of 0.98 ± 0.02 for the non-sonicated one and 0.97 ± 0.10 for the sonicated (10 min) one. Nevertheless, the sonication leads to a decreased layer homogeneity, which is indicated by the larger deviation of the I_D/I_G-ratios. All these findings are in agreement with the optical findings of laser microscopy and the FIB-Cut SEM images. After the thermal reduction to regain the electrical conductivity, the electrical resistances of the non-sonicated and sonicated samples were finally determined by electrical measurements. The obtained resistances after 0 min, 1 min and 10 min of ultrasonic treatment and their corresponding deviations are shown in Table 16.

Table 16. Electrical characterization of micro-dispensed rGO layers after different sonication times.

Sonication Time min	Electrical Resistance kΩ
0	1.34 ± 0.36
1	1.14 ± 0.13
10	7.63 ± 3.04

By comparing the electrical resistances, no trend can be seen where sonication time and electrical resistance corelates to each other. This is initially unexpected, but may be explained as follows: Already after 1 min of ultrasonic treatment, the coffee-ring formation takes place, which results in a partially increased layer (coffee-ring) thickness and therefore in a decreased electrical resistance. Moreover, the flakes still have a lateral size of around 5 µm and therefore show a good flake to flake conductivity since the π-stacking over a quite large area is still possible. On the other hand, further ultrasonic treatment leads to a further reduction of the lateral GO flake size down to 2 µm and therefore to a reduced area where π-stacking between the flakes is possible, which finally results in an increased electrical resistance. Next to this, the large deviation after 10 min of sonication of nearly 40% shows, that the reproducibility and therefore the process stability of small GO flakes is very poor by micro-dispensing.

All these results show, that the lateral GO flake size has a big impact on the formation of a continuous and homogeneous GO layer via micro-dispensing. Especially, the coffee-ring formation is preferred drastically by smaller GO flakes due to the favored Marangoni effect.

4.3 Micro - dispensed reduced Graphene Oxide Layers for NO$_2$ Gas Sensing

Gas sensing technologies are playing a more and more crucial role in our society, due to the need of environment, emission and air quality monitoring, especially for the qualification and quantification of harmful or toxic gases [110, 111]. In literature already several materials are described which are commonly used for gas sensing applications, e.g., CP [112], MOX [113] or carbon nano materials including graphene and graphene related materials [114]. Every class of materials has its own advantages and disadvantages in terms of selectivity, response respectively recovery time and operating temperature. The latter is of particular interest when the gas sensing application should be used as a mobile instrument, since a raised operating temperature is associated with increased power consumption [111]. The comparatively high operating temperature of MOX-gas sensors [115] results in a reduced selectivity, since all present gas species – analyte and matrix – can be oxidized [116]. By using CPs, graphene or graphene related materials, the operating temperature is drastically reduced. By using graphene, it is even possible to measure at room temperature [110, 117].

Furthermore, it is known that a degeneration of the CP can takes place at ambient conditions which may lead to a slow response and recovery time, and a reduced stability [110]. Due to its large surface to volume ratio and outstanding properties like electron transport properties, efficient adsorption of gas molecules and good signal-to-noise ratio graphene and its related materials are a well-suited material for gas sensing applications [12]. Nevertheless, sensing below an operating temperature of 100 °C the humidity always has to be taken into account which may influence or disturb the sensor response and makes a reliable sensing more difficult [110]. A further advantage of graphene is the increase of sensitivity as well the introduction of selectivity against different gases by functionalization. In literature, various methods are already described by adding metal respectively MOX nanoparticles or by introducing of heteroatoms (doping) or oxygen containing groups into the carbon lattice [118].

106

In general, top-down as well as bottom-up synthesized graphene can be used for gas sensing applications. Nevertheless, the ability of functionalization, scalability and the production costs have to be taken into account for the consumer market applications. Therefore, GO respectively rGO are the graphene types of choice, since here all mentioned requirements are fulfilled. Moreover, in the case of GO respectively rGO, the oxygen containing groups are already present which increases the ability for further functionalization. Next to this, oxygen containing groups as well vacancies or aromatic rings are also binding sides for gas molecules and therefore essential for the gas detection [118, 119].

The detection of gases by graphene-containing sensor devices is based on changes in conductivity when the sensed species gets adsorbed at the sensor layer which connects to two interdigitated electrodes on an insulating substrate. Here, it must be differentiated between electron-withdrawing and electron-donating species. Electron-withdrawing molecules such as NO_2 gets adsorbed by the graphene which shows p-type semiconductor behaviour. These electron-withdrawing gases improve the doping level and increase the electrical conductivity which corresponds to a decreased resistance. The opposite happens if electron-donating molecules such as NH_3 are adsorbed. Here a decreased conductivity respectively increased resistance can be observed. Finally, the changes in conductivity can be measured and correlated to the gas concentration. Therefore, different techniques are already described in literature like chemiresistors, field effect transistors or impedance sensors [111]. In general, the electrical detection but especially chemiresistors, have huge advantages compared to other detection techniques such as miniaturization, fabrication, low cost and power consumption [110].

4.3.1 Micro - dispensed reduced Graphene Oxide against NO$_2$ sensing at different Temperatures

The performed gas measurements should show that the sensor fabrication starting from the selected graphene material and its synthesis to the graphene transfer by micro-dispensing up to the mounting of the fabricated sensors on PCB-boards allows a characterization of the produced gas sensors via chemiresistive readout. A gas measuring station and the developed gas measuring cell itself which is closed by the sensor mounted PCB-board were implemented. Here, the impermeability of the measuring cell, the control of the sensor heater and the electrical readout of the sensor fields were investigated and has been checked for their functionality and applicability. Especially, the sensor responses of the prepared sensors were investigated more thoroughly.

Low temperatures can influence the sensing properties like a poor sensor recovery, a long sensor recovery time or a decreased sensitivity. Additional heating steps which means that the sensor respectively the sensor layer get heated, can help to overcome such problems whereby adsorbed gas molecules will be removed faster and the initial sensor response will be obtained [120]. Especially by using unreduced GO, too high operation temperatures have to be avoided, since such temperatures have a drastical influence on the chemical composition of GO sensor layer. Already at temperatures higher than 200 °C oxygen containing groups are removed from the carbon lattice [121] which results in a sensor layer degeneration and therefore in a decreased life time.

For the gas measurements, the p-type semiconducting behaviour of rGO is used. By continuous adsorption and desorption with synthetic air as carrier gas, the influence of the sensing temperature on the sensor performance was investigated. Therefore, continuous gas measurements against 5 ppm, 10 ppm and 15 ppm NO$_2$ were performed at temperatures of 30 °C, 100 °C and 200 °C. The measured sensor responses and the sensor recoveries are shown in Figure 40.
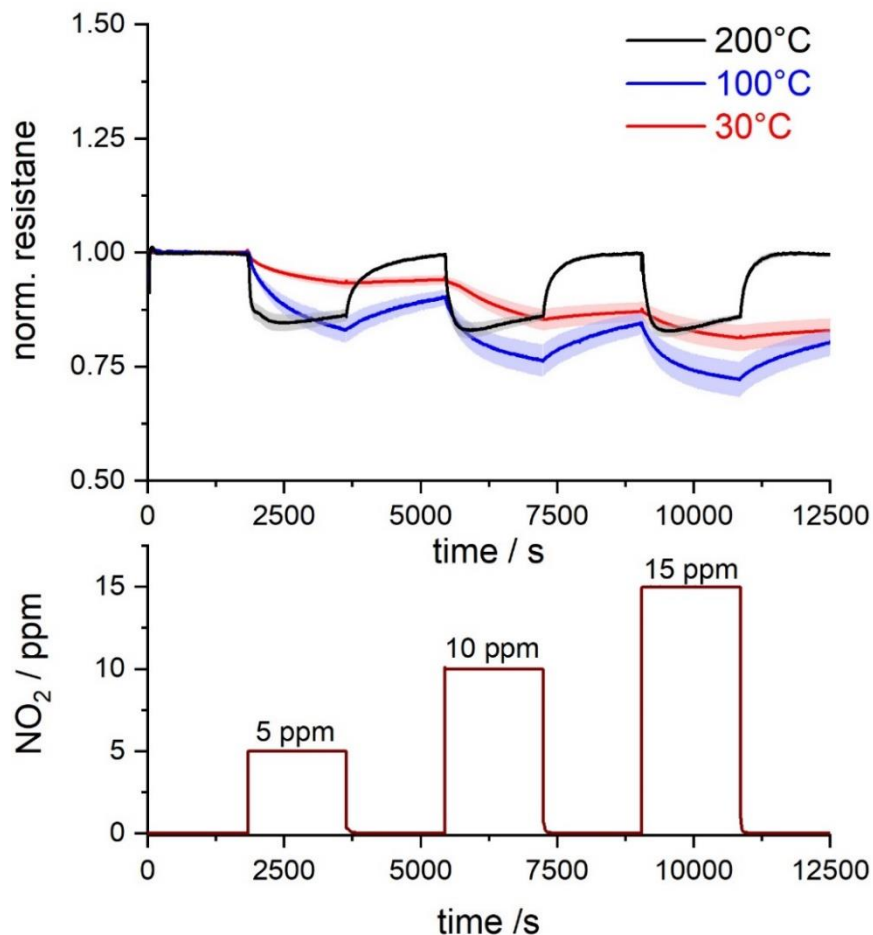
Figure 40. Changes in electrical resistance of dispensed rGO sensor layer during exposure of 5 ppm, 10 ppm and 15 ppm NO_2 at 200 °C (black), 100 °C (blue) and 30 °C (red). Every curve is obtained out of three sensors whereas the corresponding standard deviation is shown as colored shadows. The NO_2 gas flow (brown) is shown below.

For all temperatures, a decreased sensor resistance can be observed, when the dispensed rGO sensor layer is exposed to NO_2 molecules. Next to this, the sensors show totally different sensor recovery performance and NO_2 sensitivity. Whereas the sensor gets completely recovered at temperatures of 200 °C, the recovery at 30 °C respectively 100 °C is anything but complete. This incomplete sensor regeneration at temperatures below 100 °C also indicates that NO_2 gas molecules get strongly adsorbed on the rGO sensor layer, even in case of long purging with synthetic air.

Next to the sensitivity also the recovery performances of the sensor at 30 °C, 100 °C and 200 °C were determined and are shown in Table 17. The sensor recovery is strongly depending on the sensing temperature. Especially, at 30 °C the sensor recovery is very poor with a sensor recovery of around 1.5% during

the regeneration with synthetic air. The regeneration increases up to around 8% at temperatures of 100 °C. At 200 °C a complete sensor regeneration takes place within 1000 s. Next to this, the NO_2 sensitivity is increased at higher temperatures compared to 30 °C. Furthermore, the constant sensor response at temperatures at 100 °C or higher may indicate that the sensor surface and its binding sides are already saturated. It is also conceivable that an equilibrium between adsorption and desorption has been achieved, since desorption is favoured by applying high temperatures.

Table 17. Sensor performance at different sensing temperatures of micro-dispensed rGO.

Temperature °C	Sensor Signal %			Sensor Recovery %		
	5 ppm	10 ppm	15 ppm	5 ppm	10 ppm	15 ppm
30	6.7 ±1.1	8.7 ±2.8	5.9 ±3.6	0.8 ±0.5	1.7 ±3.2	1.7 ±3.9
100	16.6 ±2.8	13.9 ±5.3	11.6 ±4.5	7.7 ±4.2	7.7 ±4.2	8.3 ±1.0
200	13.0 ±1.4	13.2 ±2.1	12.4 ±0.5	13.2 ±0.8	13.2 ±0.8	12.2 ±0.45

The results show, that good NO_2 sensitivity is already reached at 100 °C. However, the regeneration at this temperature is not completely. Since the sensor recovery is complete at 200 °C, these sensors should work at an operating temperature of 200 °C. It would be also possible, that the sensor detects NO_2 at 100 °C. After one measuring step, a heating step at 200 °C will be introduced, which leads to complete sensor regeneration and reduced power consumption.

4.3.2 Influence of the lateral flake size of Reduced Graphene Oxide on the Sensor Performance

Because of the coffee-ring formation, the GO layer continuity and layer homogeneity is strongly influenced by the lateral GO flake size (as already shown and discussed in chapter 4.2.2). GO suspensions with different lateral GO flake sizes were micro-dispensed and the sensor performance regarding NO_2 sensitivity and sensor recovery were characterized. The results are shown in Figure 41.
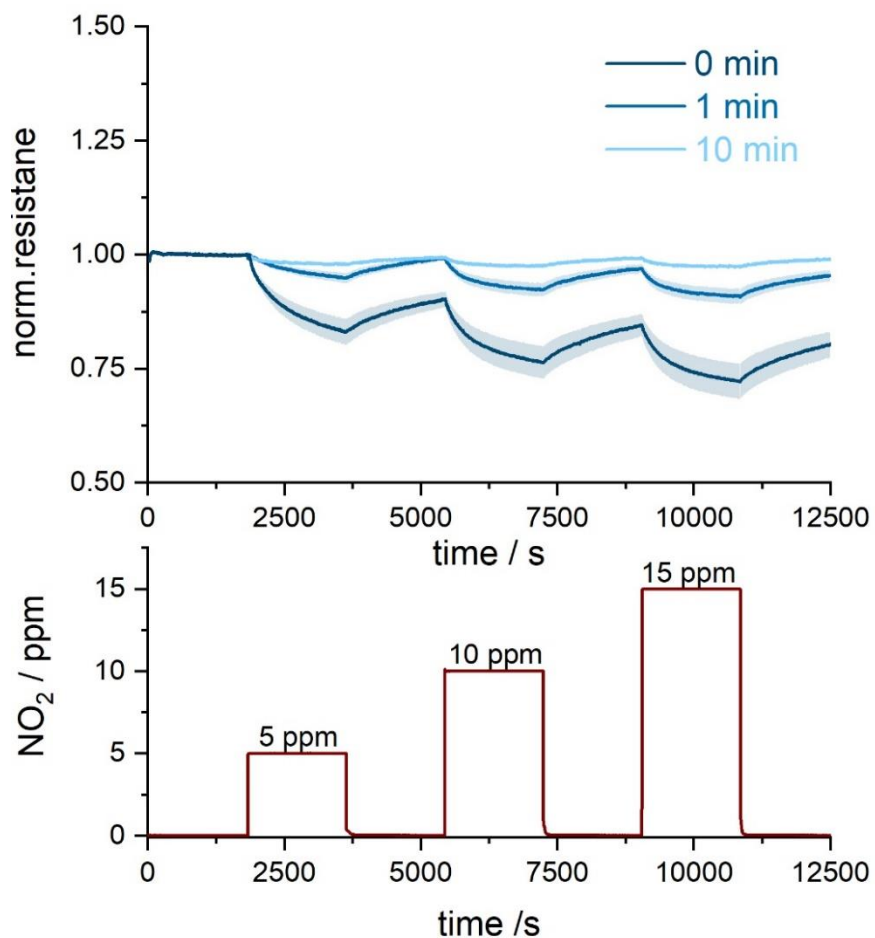
Figure 41. Changes in electrical resistance of dispensed rGO sensor layer (c(GO)=0.25 mg/mL) at 100 °C after 0 min (dark blue), 1 min (medium blue) and 10 min (bright blue) of ultrasonic treatment. Every curve is obtained out of three sensors whereas the corresponding standard deviation is shown as colored shadows. The NO_2 gas flow (brown) is shown below.

All sensors show a reduction in electrical resistance after exposure to NO_2. Nevertheless, the size of signal change is strongly influenced by the ultrasonic

treatment. Whereas the sensor with the largest GO flakes show a signal change of 16.7% for 5 ppm NO_2, the sensitivity of sensors with sonicated flakes is decreased down to 4.2% after 1 min of sonication respectively down to 2.4% after 10 min of sonication. Therefore, it can be concluded, that the ultrasonic treatment has a strong influence on the NO_2 sensitivity. Furthermore, the measurement show that all sensors do not recover completely, but the recovery is slightly better for smaller GO flakes. The detailed signal changes after NO_2 exposure as well the corresponding sensor recovery are shown in Table 18.

Table 18. Sensor performance at 100 °C of micro-dispensed rGO (c(GO)=0.25 mg/mL) after different ultrasonic treatment.

Sonication Time min	Sensor Signal %			Sensor Recovery %		
	5 ppm	10 ppm	15 ppm	5 ppm	10 ppm	15 ppm
0	16.7 ±2.8	13.8 ±3.8	12.1 ±4.5	7.0 ±3.2	8.0 ±4.2	8.5 ±4.6
1	4.2 ±1.1	6.8 ±1.8	6.1 ±1.8	4.2 ±1.2	4.6 ±1.7	4.9 ±2.1
10	2.4 ±0.1	1.8 ±0.4	1.8 ±0.3	1.5 ±0.3	1.6 ±0.3	1.9 ±0.3

Besides this, all sensors show a comparable sensor behaviour as well as sensor signal after the exposure of 5 ppm, 10 ppm respectively 15 ppm NO_2 which may show that all binding sites are already blocked by NO_2 molecules and the complete sensor is saturated. For further investigations, mainly in terms of sensor recovery, the experiment which is shown in Figure 42 was repeated at 200 °C.
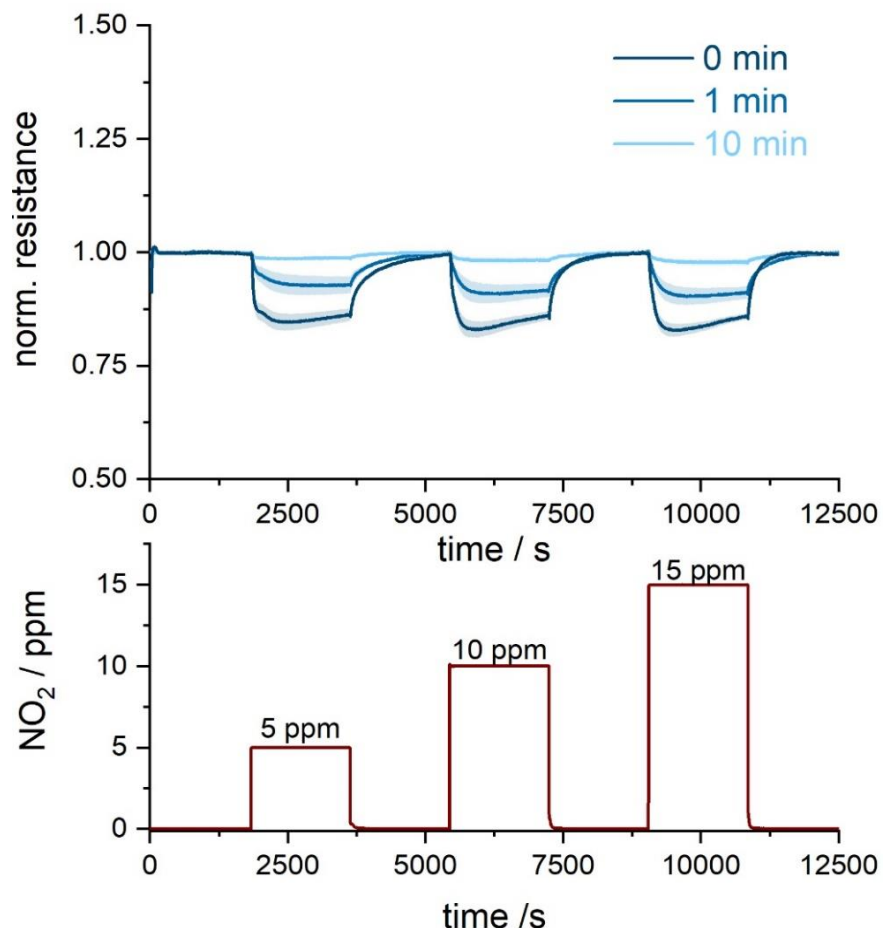
Figure 42. Changes in electrical resistance of dispensed rGO sensor layer (c(GO)=0.25 mg/mL) at 200 °C after 0 min (dark blue), 1 min (medium blue) and 10 min (bright blue) of ultrasonic treatment. Every curve is obtained out of three sensors whereas the corresponding standard deviation is shown as colored shadows. The NO_2 gas flow (brown) is shown below.

Here, for all sensor devices a complete senor regeneration can be observed after purging with synthetic air. This leads to the conclusion, that ultrasonic treatment has a strongly influence on the NO_2 sensitivity whereas the binding strength between sensor layer and NO_2 is almost independent of the lateral GO flake size. The big differences in NO_2 sensitivity are due to the coffee-ring formation. This formation leads to a thicker GO layer at the edges and therefore to a reduced electrical resistance. As a result, the electrical current runs only through the coffee-ring which leads to a strongly reduced active electrode area and to a strongly reduced sensitivity.

The detailed sensor responses as well sensor recoveries at an operating temperature of 200 °C are shown in Table 19.

Table 19. Sensor performance at 200 °C of micro-dispensed rGO (c(GO)=0.25 mg/mL) after different ultrasonic treatment.

Sonication Time min	Sensor Signal %			Sensor Recovery %		
	5 ppm	10 ppm	15 ppm	5 ppm	10 ppm	15 ppm
0	13.4 ±1.4	13.9 ±1.1	13.5 ±0.7	13.5 ±1.5	13.6 ±1.0	13.6 ±0.7
1	6.9 ±1.9	8.4 ±1.5	9.1 ±1.4	7.1 ±1.3	8.5 ±1.6	9.0 ±1.4
10	1.1 ±0.3	1.6 ±0.7	2.2 ±0.8	1.3 ±0.4	1.8 ±0.6	2.1 ±0.8

To sum up, the performed gas measurements show, that the NO_2 sensitivity is strongly influenced by the lateral GO flake size. Small GO flakes lead to a strong coffee-ring formation and therefore a reduced layer homogeneity. It is mandatory, that larger GO flakes will be used for such gas sensor applications to obtain a higher sensitivity. Due to this, such suspensions should not be exposed to too much ultrasonic treatment. Moreover, the sensor regeneration is not depending on the lateral GO flake size but is influenced by the operating temperature. Therefore, it is recommended, that the NO_2 sensing should be done at around 100 °C, whereas for the sensor regeneration heating steps up to 200 °C should be introduced to get a fully signal recovery.

The different NO_2 sensitivity shows, that a detailed material characterization is very important, especially in the case of graphene and graphene related materials, because this class of material shows an extreme bandwidth in terms of number of layers, number of defects and lateral flake size. Since the lateral flake size of graphene is not an indication of quality based on the definition of graphene, it is mandatory to observe and characterize the lateral graphene flake size and investigate the influence on the final application. For GO or stable graphene-containing suspensions this can be done by using NMR-relaxation time.

5 Conclusion & Future Perspectives

In today's world, the technological advances of recent decades have had an extremely strong influence on the modern life. Very often the boundaries of the possible were reached or were very close. To overcome these physical limitations, the development and discovery of new materials or new techniques is mandatory. One such new material – perhaps even the most famous one – is graphene which was already discovered in 2004 by Geim and Novoselov [2], and was hyped into new near unknown dimensions due to its outstanding properties like mechanical strength, chemical inertness or electrical properties [122-124]. Besides the promising theory, graphene was also able to celebrate success in a high number of applications, e.g., high-power electrical or radio frequency devices, batteries, and bio- and chemo-sensors, or as membrane for water purification [125-128]. However, the big breakthrough has not yet been achieved. Among other things, this can be explained by the fact that graphene is described as a one atom thick layer with a defect-free honeycomb carbon lattice whereas the lateral flake size of graphene is not defined. Due to this, graphene can't be described in a molecular formula. Moreover, it is very challenging to meet this definition in reality; mainly in terms of defects within the carbon lattice and the number of layers [129]. As a consequence, people already talk about graphene, even though they work with few-layer graphene, or with graphene which has a high number of defects present within the carbon lattice. Also, the different graphene syntheses lead to different kinds of graphene materials in terms of lateral graphene flake size, number of layers respectively defect density. Due to this, a detailed characterization of graphene is necessary to obtain a complete and reliable picture. Nevertheless, the broad variation of different graphene syntheses relating to different properties has a huge advantage, because the graphene can be chosen specifically for the graphene transfer regarding the final application [130].

5.1 Key Findings

In this thesis the graphene synthesis via Hummers method was scaled up and examined for applicability. The synthesized GO was characterized by optical, spectroscopical and electrical techniques to obtain a comprehensive picture of the material properties. The impurities of the GO suspensions were investigated in order to enable integration into the production facilities of the semiconductor industry. By assembling a diafiltration after the GO synthesis the degree of contaminations required in semiconductor industry has been achieved.

The characterization studies of the synthesis gave a detailed picture of the synthesized GO batches. The oxygen content of all GO-batches does not vary, which results in a reliable oxidation control during the synthesis. Since the lateral flake size of graphene is not mentioned in the definition of graphene, experiments based on different lateral GO flake sizes were realized. Here, it was demonstrated, that ultrasonic treatment reduces the lateral GO flake size whereby the defect density and the oxygen content of GO remain unchanged. However, the D-parameter of the Auger C_{KLL} line depicts an increased fraction of sp^2-hybridized carbon atoms of smaller flakes compared to larger flakes. These findings enable the introduction of NMR-relaxation time for the quality management. After defining an upper and lower limit, GO suspensions can be characterized and conclusions about the surface area which corresponds to the lateral GO flake size can be drawn. Due to this, GO suspensions can be characterized in terms of stability or agglomeration by NMR-relaxation time.

Besides a detailed material characterization, a reproducible and well-investigated graphene transfer is mandatory whereby the graphene will not be damaged. The application of oxygen plasma leads to enhanced wetting properties between interdigit gold structure and GO suspension. A constant GO spot size of 450 µm x 200 µm was obtained independent of lateral flake size and GO concentration via micro-dispensing. To cover such a spot size continuously, a GO concentration of 0.25 mg/mL is needed. It was also demonstrated, that

smaller GO flakes have a preferred ability to form a coffee-ring formation based on the Marangoni effect which results in a reduced GO layer homogeneity.

In addition to that, the results of the performed NO_2 gas measurements show, that the NO_2 sensitivity of dispensed rGO sensor layers is mainly depending on the lateral GO flake size whereby smaller GO flakes have a strongly reduced NO_2 sensitivity compared to larger ones. The sensor regeneration is driven by the temperature. For a complete sensor regeneration, a temperature up to 200 °C is necessary and is almost independent of the lateral GO flake size.

In general, it could be shown, that GO synthesized by Hummers method was successfully up-scaled and introduced into the semiconductor industry. The resulting aqueous GO suspensions were prosperously transferred by micro-dispensing on interdigit gold electrodes. After thermal reduction of GO the prepared sensors show promising results for the NO_2 detection whereas the NO_2 sensitivity is strongly influenced by the lateral GO flake size.

5.2 Remaining Challenges

To reduce the effort of the GO purification, both the necessity as well as the time factor, $NaNO_3$ should be exchanged, e.g., by KNO_3. The critical concentration of potassium is higher than the concentration of sodium, since the ability to migrate within the semiconductor devices is reduced due to the increased ion radius of potassium. First approaches, to remove $NaNO_3$ and replace it by KNO_3, are already described [131]. By replacing $NaNO_3$ the lateral GO flake size must be observed since larger GO flakes show a decreased coffee-ring formation and an enhanced NO_2 sensitivity and are therefore favoured.

In general, a standardization of the graphene characterization has to be defined, to enable the comparison of graphene and graphene related materials of different research groups all around the world. At least a standard of characterization for the defect density within the graphene material is desirable. Furthermore, improved characterization will help to divide graphene obtained by

different synthesis strategies more strictly into different classes, e.g., exfoliated graphene, oxidized graphene, micro- or respectively nano-graphene [129]. Such a conceivable and logical classification is shown in Figure 43.
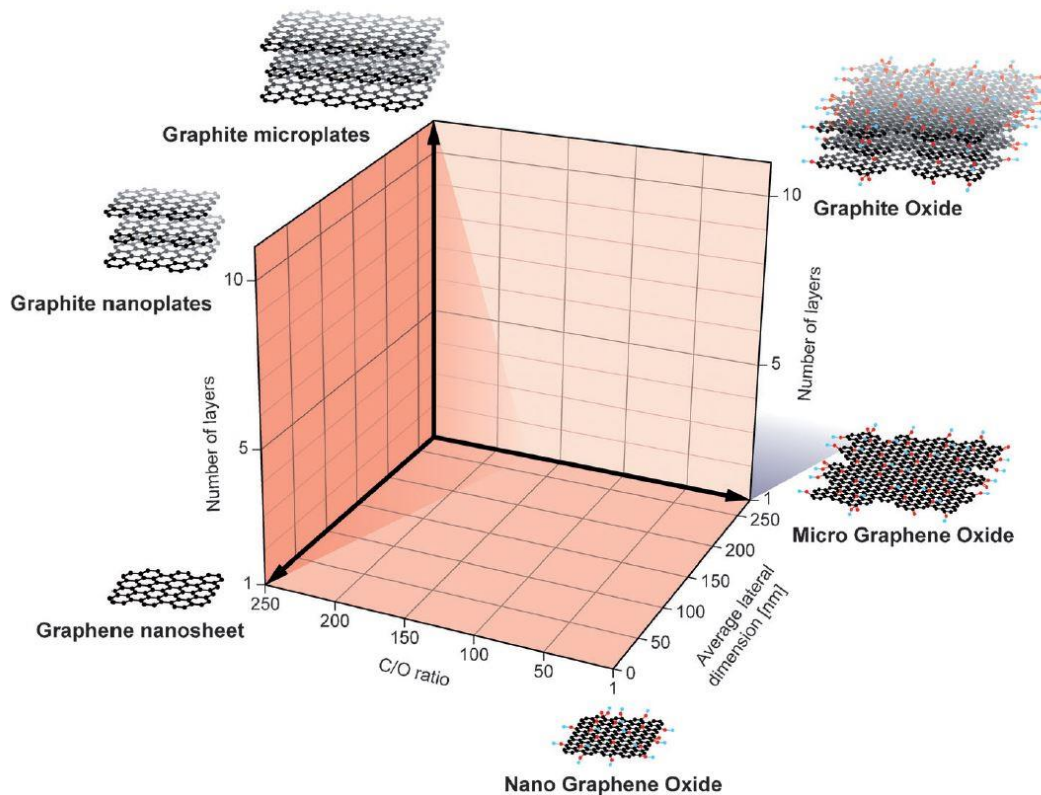
Figure 43. Categorization grid for different Graphene types based on the three fundamental Graphene parameters: C/O-ratio (x-axis), number of layers (y-axis) and lateral flake size (z-axis). Idealized examples of the different types of Graphene are shown at the corners of the diagram.

Reprinted with permission from [129].

The introduction of new graphene characterizing values would be very helpful. For the future, graphene should be characterized - especially for top down methods - by the lateral flake size distribution. This could be done quite similar to polymers which are already classified by the molar mass distribution (M_w) [132].

For the industrial scale, characterization techniques with a high throughput are mandatory. However, techniques like HR-TEM, AFM and XPS which are already commonly used due to their high spatial resolution have a very limited throughput and a complex sample preparation. Therefore, further improvements

such as new test procedures or concepts which reduces the measuring time must be developed.

Also, the implementation of a gas sensor device needs further research. Since a mobile phone has a typical period of use of three years such a sensor device has to work for at least the same time. Therefore, stability and reliability tests are needed where extreme temperatures like -20 °C or +60 °C are tested. Since smartphones are also being used more and more often during sport activities, the influence of human sweat on the sensor device must also be investigated for the final introduction to the consumer market.

5.3 Future Directions

In the last decades, the environmental air monitoring generated increased interest. Next to the detection and monitoring of NO_x, atmospheric aerosol or other gases like CO, CO_2, H_2 or CH_4 could be monitored. As already described in literature, GO can be modified with different metal nanoparticles which introduce selectivity against different gases. The addition of platinum respectively palladium nanoparticles leads to an increased sensitivity and selectivity against hydrogen [133], whereas the assembly of GO with copper oxide nanoparticles leads to sensing properties against carbon monoxide [134]. By combining such different modified sensor fields, a sensor array can be generated, where these different modified sensor fields generate a various response behaviour after the exposure to certain gases. Based on the different sensor behaviour, conclusions about the respective gas can be drawn and quantified by the response intensity [135]. After reaching the marketability, such sensor arrays can be introduced into mobile phones or smart home devices. Such devices could monitor the indoor air quality of living rooms or offices and respond, for example, if the CO_2 concentration is too high. Next to this, also outdoor monitoring is conceivable for these arrays. Here, the emissions of traffic or industry can be observed.

Next to selectivity, a good sensor device is characterized by an issue-specific sensitivity against the monitored gas whereby the critical and harmful concentration of the investigated gas species is taken into account. Otherwise, a reliable gas detection is not possible which shown by the MAK values, of the following gases: CO_2 has a MAK value of 9100 mg/m³ (4973 ppm). This is more than 2 orders of magnitude higher than the MAK values of CO of 35 mg/m³ (which corresponds to 30 ppm) or NO_2 of 0.95 mg/m³ (which corresponds to 0.5 ppm). The measuring range, which means the ability of the sensor to recognize the analyte molecules in the desired concentrations, must be also taken into account. Only then such an application is ready for the market and easily usable for the customers.

6 Summary

This thesis describes an up-scaled graphene synthesis via Hummers method, its purification as well the system integration by micro-dispensing for chemiresistive NO_2 gas detection on large industrial scale. **Chapter 1** provides an overview about the current trends in optical characterization techniques of 2D carbon nanomaterials, especially graphene. Here, the focus is the advantages, disadvantages as well the limitations of the current characterization techniques based on lateral flake size, number of layers, morphology, chemical functionalities and graphene dispersions. In **Chapter 2** the aim of the work respectively the motivation is presented as the preparation, purification and characterization of graphene as well as the system integration for the semiconductor industry and its potential for the environmental and air quality monitoring.

The experimental setups as well as the measuring parameters of the chosen characterization techniques and sample preparation is described In **Chapter 3**. Also, the route of GO synthesis (Hummers method) including its purification (diafiltration), the system integration (micro-dispensing), the sensor chip and sensor design (interdigit gold electrodes), and the gas measuring station are described respectively explained.

In **Chapter 4** the processes starting from the graphene synthesis, its purification and characterization over the system integration to the final sensor application are discussed. In a first part, an up-scaled graphene synthesis derived by Hummers method was established and diafiltration was applied for purification whereas the level of ionic contaminations could be reduced in such an extent, that the obtained graphene suspensions are usable in the semiconductor industry. Subsequently, the six synthesized GO batches were characterized and compared to each other. Whereas the chemical structure of the six prepared GO batches are very similar regarding chemical composition, the main finding was, that the lateral GO flake size distribution differs between these batches. Due to this, GO flakes with different lateral size were fabricated and investigated. Here,

typical characterization techniques like Raman or XPS reach their limits, especially in terms of spatial resolution and throughput. Therefore, NMR-relaxation time measurements were applied and demonstrated to be sensitive against different lateral GO flake sizes.

The transfer of GO suspensions via micro-dispensing was optimized and a homogeneous layer on interdigit gold structures was formed. A GO concentration of at least 0.25 mg/mL is needed to create a continuous layer. Moreover, an oxygen plasma enhances the wettability between substrate and GO suspension which prevents any coffee-ring formation. It was demonstrated, that the lateral GO flake size has a huge impact on the GO layer homogeneity, layer continuity and especially on the coffee-ring formation which is strongly favoured by smaller GO flakes.

Finally, the NO_2 sensitivity of the micro-dispensed GO layers was investigated at different operating temperatures by gas measurements. Here it was demonstrated, that the sensor recovery is strongly influenced by the operating temperature, whereas the NO_2 sensitivity is nearly identical for temperatures of 100 °C respectively 200 °C. A full sensor recovery was only observed for temperatures of around 200°C. Moreover, layers with smaller GO flakes have a strongly decreased sensitivity against NO_2 compared to larger ones at 100 °C as well as at 200 °C. Whereas the sensor recovery is not complete at 100 °C and temperatures of 200 °C are needed, the lateral GO flake size has no influence on the recovery. At 200 °C the sensors recover completely for small GO flakes as well as for larger ones.

Chapter 5 provides a succinct discussion of the main findings and insights acquired within this work with respect to the ideal lateral GO flake sizes and dispensing parameters for the system integration of GO suspensions on interdigit gold electrodes for NO_2 sensing.

7 Zusammenfassung

Diese Arbeit beschreibt die Graphensynthese nach der „Hummers Methode", deren Aufreinigung sowie die Systemintegration von GO Suspensionen durch Mikrodosierung zur chemiresistiven NO_2-Gasdetektion im großindustriellen Maßstab. **Kapitel 1** gibt einen Überblick über die aktuellen Trends durch optische Charakterisierungstechniken von 2D-Kohlenstoffnanomaterialien, insbesondere von Graphen. Dabei stehen die Vor und Nachteile sowie die Grenzen der einzelnen Charakterisierungstechniken in Bezug auf die laterale Flockengröße, Anzahl der Schichten, der Morphologie, den chemischen Funktionalitäten und der Charakterisierung von Graphen Suspensionen im Vordergrund. In **Kapitel 2** wird das Ziel der Arbeit beziehungsweise die Motivation vorgestellt wie etwa die Synthese, die Aufreinigung und die Charakterisierung von Graphen sowie die industrietaugliche Systemintegration und deren Potential für die Umwelt- und Luftqualitätsüberwachung.

Die Versuchsaufbauten sowie die Messparameter der gewählten Charakterisierungstechniken und die Probenpräparation werden in **Kapitel 3** beschrieben. Außerdem wird der Weg der GO Synthese (Hummers Methode) einschließlich ihrer Reinigung (Diafiltration), die Systemintegration (Mikro-Dosierung), Sensorchips und Design (interdigitale Goldelektroden) und der Gasmessstand beschrieben beziehungsweise erklärt.

In **Kapitel 4** werden die Prozesse angefangen von der Graphensynthese, deren Aufreinigung und Charakterisierungen über die Systemintegration bis hin zur Sensoranwendung diskutiert. Im ersten Teil wurde eine maßstabsvergrößerte Graphensynthese nach der „Hummers Methode" etabliert. Außerdem wurde eine Diafiltration wurde zur weiteren Aufreinigung angewendet, wobei die ionischen Verunreinigungen soweit reduziert wurden, dass die erhaltenen Graphensuspensionen in der Halbleiterindustrie verwendet werden können. Anschließend wurden die sechs synthetisierten GO Chargen charakterisiert und miteinander verglichen. Während die chemische Struktur der sechs hergestellten GO Chargen hinsichtlich der chemischen Zusammensetzung identisch sind, war

das Hauptergebnis, dass die laterale GO Flockengrößenverteilung zwischen diesen Chargen unterschiedlich ist. Aus diesem Grund wurden GO Flocken mit unterschiedlicher lateraler Größe hergestellt und untersucht. Dabei zeigte sich, dass typische Charakterisierungstechniken wie Raman oder XPS an ihre Grenzen stoßen, insbesondere in Bezug auf die räumliche Auflösung und Durchsatz. Daher wurden NMR-Relaxationszeitmessungen durchgeführt, die sich als empfindlich gegenüber verschiedenen lateralen GO Flockengrößen erwiesen.

Der Transfer von GO Suspensionen mittels Mikrodosierung wurde optimiert und eine homogene Schicht auf interdigitalen Goldstrukturen abgeschieden. Eine GO Konzentration von mindestens 0,25 mg/mL ist erforderlich, um eine kontinuierliche Schicht zu erzeugen. Darüber hinaus verbessert ein Sauerstoffplasma die Benetzbarkeit zwischen Substrat und GO Suspension, wodurch eine Kaffeering-Bildung verhindert wird. Außerdem konnte gezeigt werden, dass die laterale GO Flockengröße einen großen Einfluss auf die Homogenität der GO Schicht, die Schichtkontinuität und insbesondere auf die Bildung eines Kaffeerings hat, die durch kleinere GO Flocken stark begünstigt wird.

Schließlich wurde die NO_2 Empfindlichkeit der mikrodosierten GO Schichten bei verschiedenen Betriebstemperaturen mittels Gasmessungen untersucht. Dabei zeigte sich, dass die Sensorempfindlichkeit stark von der Betriebstemperatur beeinflusst wird, während die NO_2 Sensitivitäten bei Temperaturen von 100 °C bzw. 200 °C nahezu identisch sind. Eine vollständige Sensorregeneration wurde nur bei Temperaturen um 200 °C beobachtet. Darüber hinaus haben Schichten mit kleineren GO Flocken eine stark verminderte Empfindlichkeit gegenüber NO_2 im Vergleich zu größeren sowohl bei 100 °C als auch bei 200 °C. Während die Sensorregeneration bei 100 °C nicht vollständig ist und Temperaturen von 200 °C benötigt werden, hat die laterale GO Flockengröße keinen Einfluss auf die Regeneration. Diese ist unabhängig von der Flockengröße bei 200 °C vollständig.

Kapitel 5 eine kurze und knappe Diskussion der wichtigsten Erkenntnisse und Einsichten, die im Rahmen dieser Arbeit in Bezug auf die idealen lateralen GO Flockengrößen und Dispensierungsparameter für die Systemintegration von GO

Suspensionen auf interdigitalen Goldelektroden für die NO_2-Sensorik gewonnen wurden.

8 References

[1]   C. Soldano, A. Mahmood, and E. Dujardin, "Production, properties and potential of graphene," *Carbon*, vol. 48, no. 8, pp. 2127–2150, 2010, doi: 10.1016/j.carbon.2010.01.058.

[2]   K. S. Novoselov *et al.*, "Electric Field Effect in Atomically Thin Carbon Films," *Science*, vol. 306, no. 5696, pp. 666–669, 2004, doi: 10.1126/science.1102896.

[3]   K. S. Novoselov, V. I. Fal'ko, L. Colombo, P. R. Gellert, M. G. Schwab, and K. Kim, "A roadmap for graphene," *Nature*, vol. 490, no. 7419, pp. 192–200, 2012, doi: 10.1038/nature11458.

[4]   W. S. Hummers and R. E. Offeman, "Preparation of Graphitic Oxide," *J. Am. Chem. Soc.*, vol. 80, no. 6, pp. 1339–1339, 1958, doi: 10.1021/ja01539a017.

[5]   D. Fairhurst, T. Cosgrove, and S. W. Prescott, "Relaxation NMR as a tool to study the dispersion and formulation behavior of nanostructured carbon materials: Relaxation NMR for nanostructured carbons," *Magnetic Resonance in Chemistry*, vol. 54, no. 6, pp. 521–526, Jun. 2016, doi: 10.1002/mrc.4218.

[6]   C. Tan *et al.*, "Recent Advances in Ultrathin Two-Dimensional Nanomaterials," *Chem. Rev.*, vol. 117, no. 9, pp. 6225–6331, 2017, doi: 10.1021/acs.chemrev.6b00558.

[7]   J. Jeevanandam, A. Barhoum, Y. S. Chan, A. Dufresne, and M. K. Danquah, "Review on nanoparticles and nanostructured materials: history, sources, toxicity and regulations," *Beilstein J. Nanotechnol.*, vol. 9, pp. 1050–1074, 2018, doi: 10.3762/bjnano.9.98.

[8]   X. Sun *et al.*, "Nano-graphene oxide for cellular imaging and drug delivery," *Nano Res.*, vol. 1, no. 3, pp. 203–212, 2008, doi: 10.1007/s12274-008-8021-8.

[9]   V. H. R. Souza, M. M. Oliveira, and A. J. G. Zarbin, "Bottom-up synthesis of graphene/polyaniline nanocomposites for flexible and transparent energy storage devices," *J. Power Source*, vol. 348, pp. 87–93, 2017, doi: 10.1016/j.jpowsour.2017.02.064.

[10]   R.-L. Oliveira, C. S. Oliveira, R. Landers, and C. R. D. Correia, "Pd Nanoparticles Immobilized on Graphene Oxide/Silica Nanocomposite: Efficient and Recyclable Catalysts for Cross-Coupling Reactions," *ChemistrySelect*, vol. 3, no. 2, pp. 535–543, 2018, doi: 10.1002/slct.201702693.

[11] M. F. El-Kady and R. B. Kaner, "Direct Laser Writing of Graphene Electronics," *ACS Nano*, vol. 8, no. 9, pp. 8725–8729, 2014, doi: 10.1021/nn504946k.

[12] T. Kuila, S. Bose, P. Khanra, A. K. Mishra, N. H. Kim, and J. H. Lee, "Recent advances in graphene-based biosensors," *Biosens. Bioelectron.*, vol. 26, no. 12, pp. 4637–4648, 2011, doi: 10.1016/j.bios.2011.05.039.

[13] A. Zöpfl, M. M. Lemberger, M. König, G. Ruhl, F. M. Matysik, and T. Hirsch, "Reduced graphene oxide and graphene composite materials for improved gas sensing at low temperature," *Faraday Discuss.*, vol. 173, pp. 403–414, 2014, doi: 10.1039/C4FD00086B.

[14] Md. S. A. Bhuyan, Md. N. Uddin, Md. M. Islam, F. A. Bipasha, and S. S. Hossain, "Synthesis of graphene," *Int. Nano Lett*, vol. 6, no. 2, pp. 65–83, 2016, doi: 10.1007/s40089-015-0176-1.

[15] D. Li and R. B. Kaner, "MATERIALS SCIENCE: Graphene-Based Materials," *Science*, vol. 320, no. 5880, pp. 1170–1171, 2008, doi: 10.1126/science.1158180.

[16] A. T. Smith, A. M. LaChance, S. Zeng, B. Liu, and L. Sun, "Synthesis, properties, and applications of graphene oxide/reduced graphene oxide and their nanocomposites," *Nano Materials Science*, vol. 1, no. 1, pp. 31–47, 2019, doi: 10.1016/j.nanoms.2019.02.004.

[17] R. S. Edwards and K. S. Coleman, "Graphene synthesis: relationship to applications," *Nanoscale*, vol. 5, no. 1, pp. 38–51, 2013, doi: 10.1039/C2NR32629A.

[18] J.-H. Zhong *et al.*, "Quantitative Correlation between Defect Density and Heterogeneous Electron Transfer Rate of Single Layer Graphene," *J. Am. Chem. Soc.*, vol. 136, no. 47, pp. 16609–16617, 2014, doi: 10.1021/ja508965w.

[19] M. Seifert *et al.*, "Role of grain boundaries in tailoring electronic properties of polycrystalline graphene by chemical functionalization," *2D Mater.*, vol. 2, no. 2, p. 024008, 2015, doi: 10.1088/2053-1583/2/2/024008.

[20] S. S. Shams, R. Zhang, and J. Zhu, "Graphene synthesis: a Review," *Mater. Sci.-Poland*, vol. 33, no. 3, pp. 566–578, 2015, doi: 10.1515/msp-2015-0079.

[21] H. C. Lee *et al.*, "Review of the synthesis, transfer, characterization and growth mechanisms of single and multilayer graphene," *RSC Adv.*, vol. 7, no. 26, pp. 15644–15693, 2017, doi: 10.1039/C7RA00392G.

[22] K. Toda, R. Furue, and S. Hayami, "Recent progress in applications of graphene oxide for gas sensing: A review," *Chim. Acta*, vol. 878, pp. 43–53, 2015, doi: 10.1016/j.aca.2015.02.002.

[23] M. Sohail *et al.*, "Modified and improved Hummer's synthesis of graphene oxide for capacitors applications," *Mod. Electron. Mater.*, vol. 3, no. 3, pp. 110–116, 2017, doi: 10.1016/j.moem.2017.07.002.

[24] F. Torrisi *et al.*, "Inkjet-Printed Graphene Electronics," *ACS Nano*, vol. 6, no. 4, pp. 2992–3006, 2012, doi: 10.1021/nn2044609.

[25] C. H. A. Wong, Z. Sofer, M. Kube ova, J. Ku era, S. Mat jkova, and M. Pumera, "Synthetic routes contaminate graphene materials with a whole spectrum of unanticipated metallic elements," *Proceedings of the National Academy of Sciences*, vol. 111, no. 38, pp. 13774–13779, 2014, doi: 10.1073/pnas.1413389111.

[26] H. L. Poh, F. Šaněk, A. Ambrosi, G. Zhao, Z. Sofer, and M. Pumera, "Graphenes prepared by Staudenmaier, Hofmann and Hummers methods with consequent thermal exfoliation exhibit very different electrochemical properties," *Nanoscale*, vol. 4, no. 11, p. 3515, 2012, doi: 10.1039/c2nr30490b.

[27] R. Chawla, P. Singhal, and A. K. Garg, "The Role of the GO Synthesis Process in Regulation of Non-linear Optic Properties," *JOM*, vol. 71, no. 5, pp. 1634–1642, 2019, doi: 10.1007/s11837-019-03395-x.

[28] A. Y. S. Eng, C. K. Chua, and M. Pumera, "Refinements to the structure of graphite oxide: absolute quantification of functional groups via selective labelling," *Nanoscale*, vol. 7, no. 47, pp. 20256–20266, 2015, doi: 10.1039/C5NR05891K.

[29] I. Constant, F. Tardif, and J. Derrien, "Deposition and removal of sodium contamination on silicon wafers," *Semiconductor Science and Technology*, vol. 15, no. 1, pp. 61–66, 2000, doi: 10.1088/0268-1242/15/1/311.

[30] F. J. Tölle, K. Gamp, and R. Mülhaupt, "Scale-up and purification of graphite oxide as intermediate for functionalized graphene," *Carbon*, vol. 75, pp. 432–442, 2014, doi: 10.1016/j.carbon.2014.04.022.

[31] I. Barbolina, C. R. Woods, N. Lozano, K. Kostarelos, K. S. Novoselov, and I. S. Roberts, "Purity of graphene oxide determines its antibacterial activity," *2D Materials*, vol. 3, no. 2, p. 025025, 2016, doi: 10.1088/2053-1583/3/2/025025.

[32] B. Yurash and B. E. Deal, "A Method for Determining Sodium Content of Semiconductor Processing Materials," *J. Electrochem. Soc.*, vol. 115, no. 11, p. 1191, 1968, doi: 10.1149/1.2410937.

[33] P. Kubáň, M. A. Müri, and P. C. Hauser, "Application of a contactless conductivity detector to the determination of inorganic ions in ion chromatography," *Analyst*, vol. 129, no. 1, pp. 82–86, 2004, doi: 10.1039/B311376K.

[34] A. Ambrosi, S. Y. Chee, B. Khezri, R. D. Webster, Z. Sofer, and M. Pumera, "Metallic Impurities in Graphenes Prepared from Graphite Can Dramatically Influence Their Properties," *Angew. Chem. Int. Ed.*, vol. 51, no. 2, pp. 500–503, 2012, doi: 10.1002/anie.201106917.

[35] C. K. Chua *et al.*, "Chemical Preparation of Graphene Materials Results in Extensive Unintentional Doping with Heteroatoms and Metals," *Chemistry - A European Journal*, vol. 20, no. 48, pp. 15760–15767, 2014, doi: 10.1002/chem.201404205.

[36] E. Aliyev, V. Filiz, M. M. Khan, Y. J. Lee, C. Abetz, and V. Abetz, "Structural Characterization of Graphene Oxide: Surface Functional Groups and Fractionated Oxidative Debris," *J. Nanomater.*, vol. 9, no. 8, p. 1180, 2019, doi: 10.3390/nano9081180.

[37] J.-L. Chen and X.-P. Yan, "Ionic strength and pH reversible response of visible and near-infrared fluorescence of graphene oxide nanosheets for monitoring the extracellular pH," *Chem. Commun.*, vol. 47, no. 11, p. 3135, 2011, doi: 10.1039/c0cc03999c.

[38] L. Shahriary and A. A. Athawale, "Graphene Oxide Synthesized by using Modified Hummers Approach," *Int. J.Rrenew.*, vol. 02, no. 01, pp. 58–63, 2014.

[39] L. Zhang, J. Liang, Y. Huang, Y. Ma, Y. Wang, and Y. Chen, "Size-controlled synthesis of graphene oxide sheets on a large scale using chemical exfoliation," *Carbon*, vol. 47, no. 14, pp. 3365–3368, 2009, doi: 10.1016/j.carbon.2009.07.045.

[40] Q. Lai, S. Zhu, X. Luo, M. Zou, and S. Huang, "Ultraviolet-visible spectroscopy of graphene oxides," *AIP Advances*, vol. 2, no. 3, p. 032146, Sep. 2012, doi: 10.1063/1.4747817.

[41] F. Schwierz, "Graphene transistors," *Nature Nanotech.*, vol. 5, no. 7, pp. 487–496, 2010, doi: 10.1038/nnano.2010.89.

[42] V. Gupta, N. Sharma, U. Singh, Mohd. Arif, and A. Singh, "Higher oxidation level in graphene oxide," *Optik*, vol. 143, pp. 115–124, 2017, doi: 10.1016/j.ijleo.2017.05.100.

[43] A. Jilani *et al.*, "Facile spectroscopic approach to obtain the optoelectronic properties of few-layered graphene oxide thin films and their role in photocatalysis," *New J. Chem.*, vol. 41, no. 23, pp. 14217–14227, 2017, doi: 10.1039/C7NJ03614K.

[44] B. D. Viezbicke, S. Patel, B. E. Davis, and D. P. Birnie, "Evaluation of the Tauc method for optical absorption edge determination: ZnO thin films as a model system: Tauc method for optical absorption edge determination," *Phys. Status Solidi B*, vol. 252, no. 8, pp. 1700–1710, 2015, doi: 10.1002/pssb.201552007.

[45] F. Zheng, W.-L. Xu, H.-D. Jin, X.-T. Hao, and K. P. Ghiggino, "Charge transfer from poly(3-hexylthiophene) to graphene oxide and reduced graphene oxide," *RSC Adv.*, vol. 5, no. 109, pp. 89515–89520, 2015, doi: 10.1039/C5RA18540H.

[46] A. C. Ferrari *et al.*, "Raman Spectrum of Graphene and Graphene Layers," *Phys. Rev. Lett.*, vol. 97, no. 18, p. 187401, 2006, doi: 10.1103/PhysRevLett.97.187401.

[47] R. Muzyka, S. Drewniak, T. Pustelny, M. Chrubasik, and G. Gryglewicz, "Characterization of Graphite Oxide and Reduced Graphene Oxide Obtained from Different Graphite Precursors and Oxidized by Different Methods Using Raman Spectroscopy," *Materials*, vol. 11, no. 7, p. 1050, 2018, doi: 10.3390/ma11071050.

[48] H. Chen, W. Du, J. Liu, L. Qu, and C. Li, "Efficient room-temperature production of high-quality graphene by introducing removable oxygen functional groups to the precursor," *Chem. Sci.*, vol. 10, no. 4, pp. 1244–1253, 2019, doi: 10.1039/C8SC03695K.

[49] S. Eigler, C. Dotzer, and A. Hirsch, "Visualization of defect densities in reduced graphene oxide," *Carbon*, vol. 50, no. 10, pp. 3666–3673, 2012, doi: 10.1016/j.carbon.2012.03.039.

[50] I. Childres, L. A. Jauregui, W. Park, H. Cao, and Y. P. Chen, "Raman Spectroscopy of Graphene and related Materials," *New J. Phys*, vol. 19, p. 20, 2013.

[51] A. Kaniyoor and S. Ramaprabhu, "A Raman spectroscopic investigation of graphite oxide derived graphene," *AIP Advances*, vol. 2, no. 3, p. 032183, 2012, doi: 10.1063/1.4756995.

[52] L. G. Cançado *et al.*, "Quantifying Defects in Graphene via Raman Spectroscopy at Different Excitation Energies," *Nano Lett.*, vol. 11, no. 8, pp. 3190–3196, 2011, doi: 10.1021/nl201432g.

[53] S. Grimm, M. Schweiger, S. Eigler, and J. Zaumseil, "High-Quality Reduced Graphene Oxide by CVD-Assisted Annealing," *J. Phys. Chem. C*, vol. 120, no. 5, pp. 3036–3041, 2016, doi: 10.1021/acs.jpcc.5b11598.

[54] M. Repoux, "Comparison of background removal methods for XPS," *Surf. Interface Anal.*, vol. 18, no. 7, pp. 567–570, 1992, doi: 10.1002/sia.740180719.

[55] L. Stobinski *et al.*, "Graphene oxide and reduced graphene oxide studied by the XRD, TEM and electron spectroscopy methods," *J. Electron Spectrosc.*, vol. 195, pp. 145–154, 2014, doi: 10.1016/j.elspec.2014.07.003.

[56] M. Mohai, "XPS MultiQuant: multimodel XPS quantification software," *Surf. Interface Anal*, no. 36, pp. 828–832, 2004, doi: DOI: 10.1002/sia.1775.

[57] S. Eigler and A. Hirsch, "Chemistry with Graphene and Graphene Oxide-Challenges for Synthetic Chemists," *Angew. Chem. Int. Ed.*, vol. 53, no. 30, pp. 7720–7738, Jul. 2014, doi: 10.1002/anie.201402780.

[58] G. Greczynski and L. Hultman, "X-ray photoelectron spectroscopy: Towards reliable binding energy referencing," *Prog. Mater.*, vol. 107, p. 100591, 2020, doi: 10.1016/j.pmatsci.2019.100591.

[59] A. G. Shard, "Detection limits in XPS for more than 6000binary systems using Al and Mg KαX-rays," *Surf. Interface Anal.*, no. 46, pp. 175–185, 2013, doi: 10.1002/sia.5406.

[60] V. H. Pham *et al.*, "Chemical reduction of an aqueous suspension of graphene oxide by nascent hydrogen," *J. Mater. Chem.*, vol. 22, no. 21, p. 10530, 2012, doi: 10.1039/c2jm30562c.

[61] M. P. Araújo, O. S. G. P. Soares, A. J. S. Fernandes, M. F. R. Pereira, and C. Freire, "Tuning the surface chemistry of graphene flakes: new strategies for selective oxidation," *RSC Adv.*, vol. 7, no. 23, pp. 14290–14301, 2017, doi: 10.1039/C6RA28868E.

[62] C. L. Cooper, T. Cosgrove, J. S. van Duijneveldt, M. Murray, and S. W. Prescott, "The use of solvent relaxation NMR to study colloidal suspensions," *Soft Matter*, vol. 9, no. 30, p. 7211, 2013, doi: 10.1039/c3sm51067k.

[63] M. R. Hossain, D. Wray, A. Paul, and P. C. Griffiths, "Probing the surfaces of core-shell and hollow nanoparticles by solvent relaxation NMR," *Magnetic Resonance in Chemistry*, vol. 56, no. 4, pp. 251–256, 2018, doi: 10.1002/mrc.4707.

[64] R. Brown and I. Fatt, "Measurements of Fractional Wettability of Oil Fields' Rocks by the Nuclear Magnetic Relaxation Method," 1956, doi: 10.2523/743-G.

[65] W. P. Halperin, J. Y. Jehng, and Y. Q. Song, "Application of spin-spin relaxation to measurement of surface area and pore size distributions in a hydrating cement paste," *Magn. Reson. Imaging*, vol. 12, no. 2, pp. 169–173, 1994, doi: 10.1016/0730-725X(94)91509-1.

[66] T. Cosgrove, K. S. Jack, N. Green, T. M. Obey, and M. Wood, "NMR Solvent Relaxation Studies on Concentrated Particulate Dispersions," *ACS Symposium Series*, p. 16, 2012.

[67] K. Saoud, R. Alsoubaihi, N. Bensalah, T. Bora, M. Bertino, and J. Dutta, "Synthesis of supported silver nano-spheres on zinc oxide nanorods for

visible light photocatalytic applications," *Mater. Res. Bull.*, vol. 63, pp. 134–140, 2015, doi: 10.1016/j.materresbull.2014.12.001.

[68] C.-Y. Su *et al.*, "Electrical and Spectroscopic Characterizations of Ultra-Large Reduced Graphene Oxide Monolayers," *Chem. Mater.*, vol. 21, no. 23, pp. 5674–5680, 2009, doi: 10.1021/cm902182y.

[69] U. Khan, A. O'Neill, H. Porwal, P. May, K. Nawaz, and J. N. Coleman, "Size selection of dispersed, exfoliated graphene flakes by controlled centrifugation," *Carbon*, vol. 50, no. 2, pp. 470–475, 2012, doi: 10.1016/j.carbon.2011.09.001.

[70] C. Backes *et al.*, "Production of Highly Monolayer Enriched Dispersions of Liquid-Exfoliated Nanosheets by Liquid Cascade Centrifugation," *ACS Nano*, vol. 10, no. 1, pp. 1589–1601, 2016, doi: 10.1021/acsnano.5b07228.

[71] S. Ye and J. Feng, "The effect of sonication treatment of graphene oxide on the mechanical properties of the assembled films," *RSC Adv.*, vol. 6, no. 46, pp. 39681–39687, 2016, doi: 10.1039/C6RA03996K.

[72] L. N. Elliott, R. A. Bourne, A. Hassanpour, J. L. Edwards, S. Sutcliffe, and T. N. Hunter, "Salt enhanced solvent relaxation and particle surface area determination via rapid spin-lattice NMR," *Powder Technol.*, vol. 333, pp. 458–467, Jun. 2018, doi: 10.1016/j.powtec.2018.04.050.

[73] W. H. Walton, "Feret's statistical diameter as a measure of particle size," *Nature*, no. 162, p. 329, 1948, doi: 10.1038/162329b0.

[74] B. M. Weon and J. H. Je, "Capillary force repels coffee-ring effect," *Phys. Rev. E*, vol. 82, no. 1, p. 015305, 2010, doi: 10.1103/PhysRevE.82.015305.

[75] M. Lotya, A. Rakovich, J. F. Donegan, and J. N. Coleman, "Measuring the lateral size of liquid-exfoliated nanosheets with dynamic light scattering," *Nanotechnology*, vol. 24, no. 26, p. 265703, Jul. 2013, doi: 10.1088/0957-4484/24/26/265703.

[76] J. Stetefeld, S. A. McKenna, and T. R. Patel, "Dynamic light scattering: a practical guide and applications in biomedical sciences," *Biophys. Rev.*, vol. 8, no. 4, pp. 409–427, 2016, doi: 10.1007/s12551-016-0218-6.

[77] S. Bel Haaj, A. Magnin, C. Pétrier, and S. Boufi, "Starch nanoparticles formation via high power ultrasonication," *Carbohydr. Polym*, vol. 92, no. 2, pp. 1625–1632, 2013, doi: 10.1016/j.carbpol.2012.11.022.

[78] S. Stankovich, R. D. Piner, S. T. Nguyen, and R. S. Ruoff, "Synthesis and exfoliation of isocyanate-treated graphene oxide nanoplatelets," *Carbon*, vol. 44, no. 15, pp. 3342–3347, 2006, doi: 10.1016/j.carbon.2006.06.004.

[79] A. Liscio *et al.*, "Evolution of the size and shape of 2D nanosheets during ultrasonic fragmentation," *2D Mater.*, vol. 4, no. 2, p. 025017, 2017, doi: 10.1088/2053-1583/aa57ff.

[80] D. C. Marcano *et al.*, "Improved Synthesis of Graphene Oxide," *ACS Nano*, vol. 4, no. 8, pp. 4806–4814, 2010, doi: 10.1021/nn1006368.

[81] J. C. Lascovich, R. Giorgi, and S. Scaglione, "Evaluation of the sp2/sp3 ratio in amorphous carbon structure by XPS and XAES," *Appl. Surf. Sci.*, vol. 47, no. 1, pp. 17–21, 1991, doi: 10.1016/0169-4332(91)90098-5.

[82] S. Turgeon and R. W. Paynter, "On the determination of carbon sp2rsp3 ratios in polystyrene.polyethylene copolymers by photoelectron spectroscopy," *Thin Solid Films*, vol. 394, pp. 44–48, 2001, doi: https://doi.org/10.1016/S0040-6090(01)01134-8.

[83] A. Mezzi and S. Kaciulis, "Surface investigation of carbon films: from diamond to graphite," *Surf. Interface Anal.*, vol. 42, no. 6–7, pp. 1082–1084, 2010, doi: 10.1002/sia.3348.

[84] W. Regan *et al.*, "A direct transfer of layer-area graphene," *Appl. Phys. Lett.*, vol. 96, no. 11, p. 113102, 2010, doi: 10.1063/1.3337091.

[85] J. Li, F. Ye, S. Vaziri, M. Muhammed, M. C. Lemme, and M. Östling, "Efficient Inkjet Printing of Graphene," *Adv. Mater.*, vol. 25, no. 29, pp. 3985–3992, 2013, doi: 10.1002/adma.201300361.

[86] J. Kang, D. Shin, S. Bae, and B. H. Hong, "Graphene transfer: key for applications," *Nanoscale*, vol. 4, no. 18, p. 5527, 2012, doi: 10.1039/c2nr31317k.

[87] M. Krueger *et al.*, "Drop-Casted Self-Assembling Graphene Oxide Membranes for Scanning Electron Microscopy on Wet and Dense Gaseous Samples," *ACS Nano*, vol. 5, no. 12, pp. 10047–10054, 2011, doi: 10.1021/nn204287g.

[88] J. T. Robinson, F. K. Perkins, E. S. Snow, Z. Wei, and P. E. Sheehan, "Reduced Graphene Oxide Molecular Sensors," *Nano Lett.*, vol. 8, no. 10, pp. 3137–3140, 2008, doi: 10.1021/nl8013007.

[89] V. Dua *et al.*, "All-Organic Vapor Sensor Using Inkjet-Printed Reduced Graphene Oxide," *Angew. Chem. Int. Ed.*, vol. 49, no. 12, pp. 2154–2157, 2010, doi: 10.1002/anie.200905089.

[90] B. Derby, "Inkjet printing ceramics: From drops to solid," *J. Eur. Ceram.*, vol. 31, no. 14, pp. 2543–2550, 2011, doi: 10.1016/j.jeurceramsoc.2011.01.016.

[91] J. Li, M. C. Lemme, and M. Östling, "Inkjet Printing of 2D Layered Materials," *ChemPhysChem*, vol. 15, no. 16, pp. 3427–3434, 2014, doi: 10.1002/cphc.201402103.

[92] Y. Gao, W. Shi, W. Wang, Y. Leng, and Y. Zhao, "Inkjet Printing Patterns of Highly Conductive Pristine Graphene on Flexible Substrates," *Ind. Eng. Chem. Res.*, vol. 53, no. 43, pp. 16777–16784, 2014, doi: 10.1021/ie502675z.

[93] S. Di Risio and N. Yan, "Piezoelectric Ink-Jet Printing of Horseradish Peroxidase: Effect of Ink Viscosity Modifiers on Activity," *Macromol. Rapid Commun.*, vol. 28, no. 18–19, pp. 1934–1940, 2007, doi: 10.1002/marc.200700226.

[94] L. Fu *et al.*, "Defects regulating of graphene ink for electrochemical determination of ascorbic acid, dopamine and uric acid," *Talanta*, vol. 180, pp. 248–253, 2018, doi: 10.1016/j.talanta.2017.12.058.

[95] A. Capasso, A. E. Del Rio Castillo, H. Sun, A. Ansaldo, V. Pellegrini, and F. Bonaccorso, "Ink-jet printing of graphene for flexible electronics: An environmentally-friendly approach," *Solid State Commun.*, vol. 224, pp. 53–63, 2015, doi: 10.1016/j.ssc.2015.08.011.

[96] X. Gao, J. Jang, and S. Nagase, "Hydrazine and Thermal Reduction of Graphene Oxide: Reaction Mechanisms, Product Structures, and Reaction Design," *J. Phys. Chem. C*, vol. 114, no. 2, pp. 832–842, 2010, doi: 10.1021/jp909284g.

[97] H.-M. Ju, S. H. Huh, S.-H. Choi, and H.-L. Lee, "Structures of thermally and chemically reduced graphene," *Mater. Lett*, vol. 64, no. 3, pp. 357–360, 2010, doi: 10.1016/j.matlet.2009.11.016.

[98] S. Pei and H.-M. Cheng, "The reduction of graphene oxide," *Carbon*, vol. 50, no. 9, pp. 3210–3228, 2012, doi: 10.1016/j.carbon.2011.11.010.

[99] D. Mampallil and H. B. Eral, "A review on suppression and utilization of the coffee-ring effect," *Advances in Colloid and Interface Science*, vol. 252, pp. 38–54, 2018, doi: 10.1016/j.cis.2017.12.008.

[100] Y. Li, Q. Yang, M. Li, and Y. Song, "Rate-dependent interface capture beyond the coffee-ring effect," *Sci Rep*, vol. 6, no. 1, p. 24628, 2016, doi: 10.1038/srep24628.

[101] L. Cui *et al.*, "Suppression of the Coffee Ring Effect by Hydrosoluble Polymer Additives," *ACS Appl. Mater. Interfaces*, vol. 4, no. 5, pp. 2775–2780, 2012, doi: 10.1021/am300423p.

[102] G. D. Learn, E. J. Lai, and H. A. von Recum, "Using nonthermal plasma treatment to improve quality and durability of hydrophilic coatings on

hydrophobic polymer surfaces," Bioengineering, preprint, 2019. doi: 10.1101/868885.

[103]S. N. Alam, N. Sharma, and L. Kumar, "Synthesis of Graphene Oxide (GO) by Modified Hummers Method and Its Thermal Reduction to Obtain Reduced Graphene Oxide (rGO)*," *Graphene*, vol. 06, no. 01, pp. 1–18, 2017, doi: 10.4236/graphene.2017.61001.

[104]C. Fu, G. Zhao, H. Zhang, and S. Li, "Evaluation and Characterization of Reduced Graphene Oxide Nanosheets as Anode Materials for Lithium-Ion Batteries," *Int. J. Electrochem. Sci.*, vol. 8, pp. 6269–6280, 2013.

[105]E. B. Secor, P. L. Prabhumirashi, K. Puntambekar, M. L. Geier, and M. C. Hersam, "Inkjet Printing of High Conductivity, Flexible Graphene Patterns," *J. Phys. Chem. Lett.*, vol. 4, no. 8, pp. 1347–1351, 2013, doi: 10.1021/jz400644c.

[106]K.-Y. Shin, J.-Y. Hong, and J. Jang, "Flexible and transparent graphene films as acoustic actuator electrodes using inkjet printing," *Chem. Commun.*, vol. 47, no. 30, p. 8527, 2011, doi: 10.1039/c1cc12913a.

[107]C. Wang *et al.*, "A Reduced GO-Graphene Hybrid Gas Sensor for Ultra-Low Concentration Ammonia Detection," *Sensors*, vol. 18, no. 9, p. 3147, 2018, doi: 10.3390/s18093147.

[108]L. Dong, J. Yang, M. Chhowalla, and K. P. Loh, "Synthesis and reduction of large sized graphene oxide sheets," *Chem. Soc. Rev.*, vol. 46, no. 23, pp. 7306–7316, 2017, doi: 10.1039/C7CS00485K.

[109]H. Kim *et al.*, "Sheet Size-Induced Evaporation Behaviors of Inkjet-Printed Graphene Oxide for Printed Electronics," *ACS Appl. Mater. Interfaces*, vol. 8, no. 5, pp. 3193–3199, 2016, doi: 10.1021/acsami.5b10704.

[110]N. Joshi, T. Hayasaka, Y. Liu, H. Liu, O. N. Oliveira, and L. Lin, "A review on chemiresistive room temperature gas sensors based on metal oxide nanostructures, graphene and 2D transition metal dichalcogenides," *Microchim Acta*, vol. 185, no. 4, p. 213, Apr. 2018, doi: 10.1007/s00604-018-2750-5.

[111]M. Donarelli and L. Ottaviano, "2D Materials for Gas Sensing Applications: A Review on Graphene Oxide, MoS2, WS2 and Phosphorene," *Sensors*, vol. 18, no. 11, p. 3638, 2018, doi: 10.3390/s18113638.

[112]S. Virji, J. Huang, R. B. Kaner, and B. H. Weiller, "Polyaniline Nanofiber Gas Sensors: Examination of Response Mechanisms," *Nano Lett.*, vol. 4, no. 3, pp. 491–496, 2004, doi: 10.1021/nl035122e.

[113]S. Phanichphant, "Semiconductor Metal Oxides as Hydrogen Gas Sensors," *Procedia Engineering*, vol. 87, pp. 795–802, 2014, doi: 10.1016/j.proeng.2014.11.677.

[114] E. Llobet, "Gas sensors using carbon nanomaterials: A review," *Sensors and Actuators B: Chemical*, vol. 179, pp. 32–45, 2013, doi: 10.1016/j.snb.2012.11.014.

[115] H. Steinebach, S. Kannan, L. Rieth, and F. Solzbacher, "H2 gas sensor performance of NiO at high temperatures in gas mixtures," *Sens. Actuator B Chem.*, vol. 151, no. 1, pp. 162–168, 2010, doi: 10.1016/j.snb.2010.09.027.

[116] A. Ponzoni *et al.*, "Metal Oxide Gas Sensors, a Survey of Selectivity Issues Addressed at the SENSOR Lab, Brescia (Italy)," *Sensors*, vol. 17, no. 4, p. 714, 2017, doi: 10.3390/s17040714.

[117] S. L. Patil, M. A. Chougule, S. Sen, and V. B. Patil, "Measurements on room temperature gas sensing properties of CSA doped polyaniline–ZnO nanocomposites," *Measurement*, vol. 45, no. 3, pp. 243–249, 2012, doi: 10.1016/j.measurement.2011.12.012.

[118] S. S. Varghese, S. Lonkar, K. K. Singh, S. Swaminathan, and A. Abdala, "Recent advances in graphene based gas sensors," *Sensors and Actuators B: Chemical*, vol. 218, pp. 160–183, Oct. 2015, doi: 10.1016/j.snb.2015.04.062.

[119] W. Yuan and G. Shi, "Graphene-based gas sensors," *J. Mater. Chem. A*, vol. 1, no. 35, p. 10078, 2013, doi: 10.1039/c3ta11774j.

[120] H. Choi *et al.*, "Flexible and Transparent Gas Molecule Sensor Integrated with Sensing and Heating Graphene Layers," *Small*, vol. 10, no. 18, pp. 3685–3691, 2014, doi: 10.1002/smll.201400434.

[121] W. Chen, L. Yan, and P. R. Bangal, "Preparation of graphene by the rapid and mild thermal reduction of graphene oxide induced by microwaves," *Carbon*, vol. 48, no. 4, pp. 1146–1152, 2010, doi: 10.1016/j.carbon.2009.11.037.

[122] M. J. Allen, V. C. Tung, and R. B. Kaner, "Honeycomb Carbon: A Review of Graphene," *Chem. Rev.*, vol. 110, no. 1, pp. 132–145, 2010, doi: 10.1021/cr900070d.

[123] X. Li *et al.*, "Transfer of Large-Area Graphene Films for High-Performance Transparent Conductive Electrodes," *Nano Lett.*, vol. 9, no. 12, pp. 4359–4363, 2009, doi: 10.1021/nl902623y.

[124] Y. Zhu *et al.*, "Graphene and Graphene Oxide: Synthesis, Properties, and Applications," *Adv. Mater.*, vol. 22, no. 35, pp. 3906–3924, 2010, doi: 10.1002/adma.201001068.

[125] D. Chen, H. Feng, and J. Li, "Graphene Oxide: Preparation, Functionalization, and Electrochemical Applications," *Chem. Rev.*, vol. 112, no. 11, p. 6027−6053, 2012, doi: 10.1021/cr300115g.

[126] M. F. El-Kady and R. B. Kaner, "Scalable fabrication of high-power graphene micro-supercapacitors for flexible and on-chip energy storage," *Nat Commun*, vol. 4, no. 1, p. 1475, 2013, doi: 10.1038/ncomms2446.

[127] C. Zhang, N. Mahmood, H. Yin, F. Liu, and Y. Hou, "Synthesis of Phosphorus-Doped Graphene and its Multifunctional Applications for Oxygen Reduction Reaction and Lithium Ion Batteries," *Adv. Mater.*, vol. 25, no. 35, pp. 4932–4937, 2013, doi: 10.1002/adma.201301870.

[128] J. Zhao, W. Ren, and H.-M. Cheng, "Graphene sponge for efficient and repeatable adsorption and desorption of water contaminations," *J. Mater. Chem.*, vol. 22, no. 38, p. 20197, 2012, doi: 10.1039/c2jm34128j.

[129] P. Wick *et al.*, "Classification Framework for Graphene-Based Materials," *Angew. Chem. Int. Ed.*, vol. 53, no. 30, pp. 7714–7718, 2014, doi: 10.1002/anie.201403335.

[130] C. Hu, L. Song, Z. Zhang, N. Chen, Z. Feng, and L. Qu, "Tailored graphene systems for unconventional applications in energy conversion and storage devices," *Energy Environ. Sci.*, vol. 8, no. 1, pp. 31–54, 2015, doi: 10.1039/C4EE02594F.

[131] A. Chwalibog *et al.*, "In vitro and in vivo effects of graphene oxide and reduced graphene oxide on glioblastoma," *Int J Nanomedicine*, no. 10, pp. 1585–1596, 2015, doi: 10.2147/IJN.S77591.

[132] R. G. Jones, "Dispersity in polymer science," *Polym. Int.*, vol. 59, no. 1, pp. 22–22, 2010, doi: 10.1002/pi.2749.

[133] Y. Peng, J. Ye, L. Zheng, and K. Zou, "The hydrogen sensing properties of Pt–Pd/reduced graphene oxide based sensor under different operating conditions," *RSC Adv.*, vol. 6, no. 30, pp. 24880–24888, 2016, doi: 10.1039/C5RA26618A.

[134] D. Sun, Y. Luo, M. Debliquy, and C. Zhang, "Graphene-enhanced metal oxide gas sensors at room temperature: a review," *Beilstein J. Nanotechnol.*, vol. 9, pp. 2832–2844, Nov. 2018, doi: 10.3762/bjnano.9.264.

[135] D. Zhang, J. Liu, P. Li, and B. Xia, "Sensor array based on metal oxide modified graphene for the detection of multi-component mixed gas," in *2016 IEEE 29th International Conference on Micro Electro Mechanical Systems (MEMS)*, Shanghai, China, 2016, pp. 920–923, doi: 10.1109/MEMSYS.2016.7421781.

9 Appendix

Uncertainty analysis of gravimetry based on the example of the GO batch A1. All other GO batches are analogous.

First, the weighing boats (three boats per batch) were weighted for three times before addition of GO. The determined the averages $\emptyset_{before}$ and the corresponding deviation σm^i_{before} are shown in Table A.

$$\sigma m^i_{before} = \frac{\left|m^i_1 - \emptyset m^i_{before}\right| + \left|m^i_2 - \emptyset m^i_{before}\right| + \left|m^i_3 - \emptyset m^i_{before}\right|}{3}$$

Table A. Determined weights before addition of GO suspension with corresponding average $\emptyset m_{before}$ and deviation σm_{before}.

Measurement	Boat 1 g	Boat 2 g	Boat 3 g
m^i_1	0.62697	0.69156	0.69143
m^i_2	0.62698	0.69158	0.69415
m^i_3	0.62696	0.69161	0.69416
$\emptyset m^i_{before}$	0.62697	0.69158	0.69415
σm^i_{before}	6.67×10^{-6}	1.78×10^{-5}	1.11×10^{-5}

The same was done after storing the GO suspension (3 mL) in a desiccator containing silica gel as drying agent and is shown in Table B.

Table B. Determined weights after addition of GO suspension (3 mL) with corresponding average Øm$_{after}$ and deviation **σ**m$_{after}$.

Measurement	Boat 1 g	Boat 2 g	Boat 3 g
m$^i_1$	0.63542	0.70042	0.70297
m$^i_2$	0.63540	0.70040	0.70296
m$^i_3$	0.63539	0.70039	0.70294
Øm$^i_{after}$	0.63540	0.70040	0.70295
σm$^i_{after}$	$1.11\ 10^{-5}$	$1.11\ 10^{-5}$	$1.11\ 10^{-5}$

The difference in mass Δm^i_{3mL} of all three boats and the corresponding deviation $\Delta \sigma m i 3mL$ have been calculated Table C.

$$\Delta m^i_{3mL} = \text{Ø}m^i_{after} - \text{Ø}m^i_{before}$$

$$\Delta \sigma m^i_{3mL} = \sqrt{(|\sigma m^i_{before})^2 + (|\sigma m^i_{after})^2}$$

Table C. Calculated mass differences **Δ**m$^i_{3mL}$ and their corresponding deviations **Δσ**m$^i_{3mL}$.

	Boat 1 g	Boat 2 g	Boat 3 g
Δm$^i_{3mL}$	0.00843	0.00882	0.00881
Δσm$^i_{3mL}$	$1.29\ 10^{-5}$	$2.10\ 10^{-5}$	$1.57\ 10^{-5}$

The total average **Ø**m$_{3mL}$, the corresponding deviation **σØm**$_{3mL}$ and the total deviation **σ**$_{total}$ were calculated and are shown in Table D.

$$\text{Øm}_{3mL} = \frac{\Delta m^1_{3mL} + \Delta m^2_{3mL} + \Delta m^3_{3mL}}{3}$$

$$\sigma\text{Øm}_{3mL} = \frac{\left|\Delta m^1_{3mL} - \text{Øm}_{3mL}\right| + \left|\Delta m^2_{3mL} - \text{Øm}_{3mL}\right| + \left|\Delta m^3_{3mL} - \text{Øm}_{3mL}\right|}{3}$$

$$\sigma_{total} = \sqrt{(\Delta\sigma m^1_{3mL})^2 + (\Delta\sigma m^2_{3mL})^2 + (\Delta\sigma m^3_{3mL})^2 + (\sigma\text{Øm}_{3mL})^2}$$

Table D. Average mass difference **Øm**$_{3mL}$ with its corresponding deviations **σØm**$_{3mL}$ and the total deviation **σ**$_{total}$.

	Mass g
Øm$_{3mL}$	0.00869
σØm$_{3mL}$	1.70×10^{-4}
σ$_{total}$	1.72×10^{-4}

Finally, the mass concentration (mg/mL) and its deviation was calculated. Therefore, **Øm**$_{3mL}$ and **σ**$_{total}$ were divided by the 0.003. The mass concentration of GO batch A1 was determined as 2.90 ± 0.057 mg/mL.

Publications/Presentations/Posters

Publications

Kröner A and Hirsch T (2020) Current Trends in the Optical Characterization of Two-Dimensional Carbon Nanomaterials. Front. Chem. 7:927. doi: 10.3389/fchem.2019.00927

Aumer F, Hecht F, Kröner A, Recum P, Hirsch T. Carbon Nanomaterials for Miniaturized Gas Sensors. InMikroSystemTechnik 2019; Congress 2019 Oct 28 (pp. 1-4). VDE

Oral Presentations

2018   10. Interdisziplinäres Doktorandenseminar, Berlin, Deutschland *„Process Control for Nanomaterials via NMR-Relaxation Time*"

2018   Pitch Innovation Week Infineon Technologies AG, Regensburg, Deutschland

Poster Presentations

2018   Sensing with Graphene and 2-dimensional Materials, Aachen, Deutschland *„Process Control for Nanomaterials via NMR-Relaxation"*

2018   Innovation Week Infineon Technologies AG, Regensburg, Deutschland *„Process Control for Nanomaterials via NMR-Relaxation"*

2017   Innovation Week Infineon Technologies AG, München, Deutschland *„Simple Quality Monitoring of Nanomaterial Inks with NMR"*

Curriculum Vitae

Persönliche Daten

Name: Anton Kröner

Anschrift   Roter - Brach - Weg 64, 93049 Regensburg

Geburtsdatum   09.09.1990

Geburtsort: Landshut

Staatsangehörigkeit   Deutsch

Ausbildung

02/2016 - 09/2020   **Promotionsstudium Chemie**

                           Kooperation zwischen der Universität Regensburg und Infineon Technologies AG Regensburg

                           Dissertation: "Synthesis and Characterization of Graphene Oxide for System Integration in Semiconductor Components"

                           Institut für Analytische Chemie, Chemo- und Biosensorik (Prof. Dr. Antje J. Baeumner)

10/2013 - 12/2015   **Masterstudium Chemie,** Universität Regensburg

                           Masterarbeit: "Electrospun conductive nanofibers and their characterization"

                           Institut für Analytische Chemie, Chemo- und Biosensorik (Prof. Dr. Antje J. Baeumner)

10/2010 - 09/2013   **Bachelorstudium Chemie,** Universität Regensburg

                           Bachelorarbeit: "Anwendung von Porphyrinderivaten in der Gassensorik"

                           Institut für Analytische Chemie, Chemo- und Biosensorik (Prof. Dr. Joachim Wegener)

09/2001 - 06/2010   **Allgemeine Hochschulreife,**
                           Albertus-Magnus-Gymnasium, Regensburg

Eidesstattliche Erklärung

Ich erkläre hiermit an Eides statt, dass ich die vorliegende Arbeit ohne unzulässige Hilfe Dritter und ohne Benutzung anderer als der angegebenen Hilfsmittel angefertigt habe; die aus anderen Quellen direkt oder indirekt übernommenen Daten und Konzepte sind unter Angabe des Literaturzitats gekennzeichnet.

Weitere Personen waren an der inhaltlich-materiellen Herstellung der vorliegenden Arbeit nicht beteiligt. Insbesondere habe ich hierfür nicht die entgeltliche Hilfe eines Promotionsberaters oder anderer Personen in Anspruch genommen. Niemand hat von mir weder unmittelbar noch mittelbar geldwerte Leistungen für Arbeiten erhalten, die im Zusammenhang mit dem Inhalt der vorgelegten Dissertation stehen.

Die Arbeit wurde bisher weder im In- noch im Ausland in gleicher oder ähnlicher Form einer anderen Prüfungsbehörde vorgelegt.

_____

Ort, Datum   Unterschrift